4

NLC Damping Rings

Contents

4.1 Introduction . . . 111
4.2 System Overview and Parameter Determination . . . 112
4.2.1 Overview . . . 112
4.2.2 Damping Ring Complex Layout . . . 115
4.2.3 Requirements . . . 115
4.2.4 Parameters: Damping Times and Equilibrium Emittances . . . 117
4.2.5 Scaling Relations . . . 119
4.2.6 Ring Energy . . . 121
4.2.7 Wigglers vs. Arcs . . . 122
4.2.8 Lattice Specification . . . 122
4.2.9 RF Parameters . . . 126
4.3 Lattice Design . . . 126
4.3.1 Main Damping Rings . . . 127
4.3.2 Pre-Damping Ring . . . 136
4.3.3 Injection Line . . . 141
4.3.4 Extraction Line . . . 145
4.3.5 PPDR-to-PDR Transfer Line . . . 146
4.3.6 Bypass Lines . . . 146
4.3.7 Trajectory Correction . . . 147
4.3.8 Emittance Control and Matching . . . 149
4.3.9 Dynamic Aperture . . . 153
4.3.10 Polarization . . . 158
4.4 Collective Limitations . . . 158
4.4.1 Main Damping Ring: Impedance Model . . . 159
4.4.2 Single-Bunch Potential Well Distortion and Longitudinal Microwave Instability . . . 167
4.4.3 Single-Bunch Transverse Mode Coupling . . . 172
4.4.4 Bunch-to-Bunch Synchronous Phase Variation . . . 173
4.4.5 Coupled Bunch Instabilities . . . 177
4.4.6 Ion Trapping . . . 180
4.4.7 Positron-Electron Instability . . . 182
4.4.8 Intrabeam Scattering . . . 184
4.4.9 Beam-Gas Scattering . . . 185
4.4.10 Lifetime Limitations . . . 186
4.4.11 PPDR Collective Limitations . . . 186
4.5 RF Systems . . . 186
4.5.1 Main Damping Rings RF Systems . . . 187

4.5.2 Pre-Damping Ring RF Systems . . . 192
4.5.3 Low-Level RF Systems . . . 194
4.5.4 Energy Compressors . . . 202
4.6 Vacuum Systems . . . 202
4.6.1 Main Damping Ring . . . 202
4.6.2 Pre-Damping Ring . . . 207
4.6.3 Transport Lines . . . 208
4.7 Feedback and Feedforward Systems . . . 208
4.7.1 Coupled Bunch Transverse Feedbacks . . . 208
4.7.2 Stored Orbit Feedbacks . . . 211
4.7.3 Injection Feedbacks . . . 213
4.7.4 Extraction Feedbacks . . . 213
4.8 Vibration and Stability . . . 213
4.8.1 Vibration . . . 213
4.8.2 Stability . . . 216
4.9 Alignment and Supports . . . 216
4.9.1 Girders and Supports . . . 217
4.9.2 Mechanical Alignment . . . 217
4.9.3 Beam-based Alignment . . . 217
4.10 Magnet Design and Power Supplies . . . 219
4.10.1 Main Damping Rings . . . 219
4.10.2 Pre-Damping Ring . . . 229
4.10.3 Injection and Extraction Kickers . . . 231
4.10.4 Transport Lines . . . 236
4.11 Instrumentation for the Main Damping Rings . . . 236
4.11.1 Beam Position Monitors . . . 236
4.11.2 Beam Size Monitors . . . 237
4.11.3 Bunch Length Measurement . . . 237
4.11.4 Polarization Measurement . . . 238
4.11.5 RF Diagnostics . . . 238
4.11.6 Ion Measurements . . . 238
4.11.7 Conventional Diagnostics . . . 238
4.12 Conclusions and Comments . . . 238

4.1 Introduction

The NLC damping rings are designed to damp the incoming electron and positron beams to the very small emittances needed for collisions. The rings have three purposes: (1) damp the incoming emittances in all three planes, (2) damp incoming transients and provide a stable platform for the downstream portion of the accelerator, and (3) delay the bunches so that feedforward systems can be used to compensate for charge fluctuations.

To meet these goals, we have designed three damping rings: two identical main damping rings, one for the electrons (EDR) and one for the positrons (PDR), and a pre-damping ring for the positrons (PPDR). The pre-damping ring is needed because the incoming positron emittance is much larger than that of the electron beam. Each damping ring will store multiple trains of bunches at once. At every machine cycle, a single fully damped bunch train is extracted from the ring while a new bunch train is injected. In this manner, each bunch train can be damped for many machine cycles.

The parameters of the two main damping rings (MDR) are similar to the present generation of synchrotron light sources and the B-factory colliders that are being constructed in that they must store high-current beams ($\sim$1 A) while attaining small normalized emittances. Table 4-1 compares the NLC ring parameters with those of the SLAC B-factory Low Energy Ring (PEP-II LER), the Advanced Light Source (ALS) at Lawrence Berkeley National Laboratory (LBNL), and the Accelerator Test Facility (ATF) damping ring being constructed at KEK in Japan to verify many of the damping ring design concepts. In particular, the stored beam currents are less than half of what the PEP-II LER has been designed to store while the emittance, energy, and size of the rings are similar to those of the ALS and the ATF.

Thus, these other rings will be able to test and verify many of the accelerator physics issues that will arise in the NLC damping rings. In particular, strong coupled-bunch instabilities will be studied in the high current B-factories while issues associated with the very small beam emittances, such as intra-beam scattering and ion trapping, will be studied in the ALS and the KEK ATF damping ring. In addition, the PEP-II LER and the Advanced Photon Source (APS) at Argonne National Laboratory will be able to study the photoelectron-positron instability that is thought to arise in positron storage rings.

These similarities with other rings have also simplified the design process and we have been able to and will continue to benefit from the experience of these other accelerators. For example, the damping ring rf system is based on those developed for the SLAC B-factory and the ATF damping ring, the multibunch feedback systems are based upon the feedback systems which were designed for the SLAC B-factory and successfully verified on the ALS, and the vacuum system is similar to that used by the ALS. Furthermore, the design uses "C" quadrupole and sextupole magnets similar to those designed at the ALS and the APS at Argonne, a high-field permanent magnet wiggler very similar to a design developed and installed at Stanford Synchrotron Radiation Laboratory (SSRL), and a double kicker system for extraction similar to one to be tested in the KEK ATF.

Because the damping rings must form a stable and reliable platform for the rest of the linear collider, we have designed the rings conservatively. Whenever possible we have used concepts and designs that have been experimentally verified or will be verified in the near future and have not adopted some of the more exotic, although attractive, concepts that have been suggested. The one possible exception from this rule is the use of the TME lattice for the main damping rings instead of a standard TBA or Chasman-Green lattice. We felt that the advantages of the TME lattice—simpler and fewer bending magnets—justify this choice.

The damping ring complex consists of the injector lines for the damping rings, the positron pre-damping ring, the two main damping rings, and the transfer line between the pre-damping ring and the main positron damping ring. Section 4.2 gives an overview of the damping ring complex and defines the system requirements. Next, the determination

	NLC MDR	PEP-II LER	LBNL ALS	KEK ATF
Energy (GeV)	2.0	3.1	1.5	1.5
Circ. (m)	220	2200	200	140
Current (A)	1.2	3	0.6	0.6
$\gamma\epsilon_x$ (10^{-6}m-rad)	3	400	10	4
$\gamma\epsilon_y$ (10^{-6}m-rad)	0.02	16	0.2	0.04

Table 4-1. *Comparison of NLC main damping rings with parameters of other rings.*

of the parameters, various scaling relations, and some of the design tradeoffs that were made are discussed. The goal of this sections is to document our parameter choices so others may then explore alternate methods of optimization.

Section 4.3 presents the parameters and the optical designs of the main damping rings, pre-damping ring, injection and extraction lines, and PPDR-to-PDR transfer line. It also contains a description of the trajectory correction, emittance control and matching requirements, dynamic apertures, and the transport of the polarization through the damping ring complex.

The collective limitations are discussed in Section 4.4 and then, the rf and vacuum systems are described in Sections 4.5 and 4.6. This is followed by specifications of the feedback systems, supports and alignment techniques, magnet design and instrumentation. Finally, we discuss the ground vibration effects and some stability issues.

4.2 System Overview and Parameter Determination

In this section, we will first provide a brief overview of the damping ring complex and then we will enter a more detailed discussion of the requirements and parameter determination.

4.2.1 Overview

The damping ring complex consists of one damping ring for the electrons and both a pre-damping ring and a main damping ring for the positrons; as will be discussed, two positron rings are needed because the incoming positron emittance is very large. It also includes the transport line between the positron pre-damping ring and the main damping ring as well as elements in the extraction lines that complete the extraction system for the main damping rings. Finally, the damping ring complex includes the injection matching sections upstream of the rings which provide matching for the transverse phase space as well as the energy compressors to match the longitudinal phase space and spin rotators to orient the particle spin in the vertical direction for injection into the damping ring complex.

At present, most of the studies have concentrated on the main damping rings. Although relatively little of the detailed engineering has been performed, we have a good outline of the design and the problems we may encounter. In particular, we have identified and described solutions for the most difficult issues: these are the dynamic aperture, the vertical emittance, the impedance and instabilities, and the stability and jitter in both longitudinal and transverse phase space. As stated, much of the design rests on work being performed for the B-factories presently being constructed and the KEK ATF damping ring.

One area which has not been studied sufficiently is the design of the bending magnets. Although we have confidence that the magnets could be constructed, they are high-field combined-function magnets that need additional research to

fully verify their feasibility. We feel that it is justified to push their design since, if a design can be found, they are static devices that will not cause further trouble. If, instead, a reasonable design cannot be found, it is straightforward to scale the energy of the ring complex and reduce the requirements, although one also loses some of the tuning range in the present design and likely increases the cost.

In most aspects, the pre-damping ring has relatively loose requirements. The emittance and damping time requirements are not severe. The required beam stability is not very significant. The two difficult items are attaining the dynamic aperture and the injection/extraction kicker systems. At this time, the design is still in a preliminary stage but we have addressed the two issues just mentioned.

Main-Damping Rings

The Electron and Positron Damping Rings (EDR and PDR) are designed to damp beams with an injected emittance of $\gamma\epsilon_{x,y} = 1 \times 10^{-4}$ m-rad to an emittance of $\gamma\epsilon_x = 3 \times 10^{-6}$ m-rad and $\gamma\epsilon_y = 3 \times 10^{-8}$ m-rad. The rings will operate at 180 Hz and must provide sufficient damping to decrease an injected emittance by over four orders of magnitude.

The lattice is based on detuned Theoretical Minimum Emittance (TME) cells which were chosen because of eased requirements on the combined-function bending magnets. The damping is performed using both high-field bending magnets and ten 2.5-m sections of damping wiggler.

The rings operate with four trains of 90 bunches. The bunch trains are injected onto and extracted from the closed orbit using pulsed kickers and DC septa. To avoid coupled-bunch instabilities the rf cavities are based on those of the PEP-II B-factory and a transverse bunch-by-bunch feedback system is used. The rings are designed to operate with maximum bunch charges of 1.57×10^{10} particles; this is roughly 20% more than the maximum needed at the IP. In addition, the electron source has been designed to provide additional charge to allow for at least 10% losses during injection into the electron damping ring. Similarly, the positron source has been designed to produce at least 20% additional charge to provide for losses during injection into the pre-damping ring.

Finally, because the rings must generate extremely small beam emittances, there are tight jitter and alignment tolerances. Extensive effort has been made to include cancelations and tuning procedures in the design that will ease the tolerances to reasonable levels. In particular, all of the quadrupoles and all of the sextupoles will have independent power supplies. This will facilitate beam-based alignment as well as matching of the lattice functions.

Pre-Damping Ring

The Positron Pre-Damping Ring (PPDR) is designed to damp the large emittance positron beam from the positron source to an emittance of roughly $\gamma\epsilon_{x,y} = 1 \times 10^{-4}$ m-rad. At this point, the positrons are injected into the positron main damping ring (PDR) where they are damped to the desired final emittances. The pre-damping ring allows us to decouple the large aperture requirements for the incoming positron beams from the final emittance requirements of the linear collider.

The pre-damping- ring does not need to produce flat beams. Thus, to maximize the damping of the transverse phase space, the ring has a damping partition number $J_x \approx 1.4$ and operates on the coupling difference resonance. This increases the damping in both the horizontal and vertical planes. Furthermore, like the main damping ring, the ring damps multiple trains of bunches at once, the number of which is determined by the ring circumference. The initial design was only 114 m in circumference and stored only two trains. The present design is roughly 50% larger and stores three bunch trains. Although this increase in circumference will certainly increase the cost of the ring, the previous design was very tightly packed making the component design and maintenance substantially more difficult; experience with the SLC damping rings strongly suggests that the increase in circumference is cost-effective.

The magnets and vacuum system are being designed to provide sufficient aperture to accept a 2-GeV beam with an edge emittance of $\gamma\epsilon_{x,y} = 0.09$ m-rad and $|\delta p/p| \leq 1.5\%$ plus 2-mm clearance for misalignments and mis-steering. Given the nominal injected edge emittance of $\gamma\epsilon_{x,y} = 0.06$ m-rad, this provides a substantial margin for injection and internal mismatches. In addition, the injectors specifications assume that roughly 20% of the delivered charge is lost at injection into the pre-damping rings while the pre-damping rings are designed to operate with a maximum bunch charge that is roughly 20% greater than the maximum required at the IP.

Like the main damping rings, all of the quadrupoles and all of the sextupoles will have independent power supplies. This will facilitate beam-based alignment as well as matching of the lattice functions which is especially important in the pre-damping ring because of the limited aperture.

Injection Lines

The injection lines to the damping rings from the booster linacs are relatively straightforward transport lines. They have five primary functions:

- Provide diagnostics to monitor the beam energy, energy spread, transverse positions, and emittances.
- Provide transverse betatron matching for injection into the rings.
- Compress the incoming energy spread to match the longitudinal phase space to the damping rings.
- Rotate the longitudinal polarization of the electron beam into the vertical plane for injection into the electron damping ring.
- Include a beam dump after the diagnostics but before injection into the rings.

The spin rotation requires at least a 20° arc to rotate the longitudinal spin into the horizontal plane. We have designed a 60° arc (270° spin rotation) which is more suitable for the energy compressors. Finally, although the positron beam is not polarized, we are designing the positron system so that it could be converted to operate with polarized electrons for future $\gamma - \gamma$ or $e^- - e^-$ collisions. Thus, the geometrical constraints imposed by the spin rotation are applied to both the electron and positron injection lines.

Extraction Lines

The extraction lines from the damping rings have two purposes: they match the beams into the beginning of the spin rotator/bunch compressor beam lines that are described in Chapter 5, and they contain final elements for the extraction systems.

Bypass and Transfer Lines

There are four additional bypass and transfer lines that allow each of the rings to be bypassed and transfer the beams from the positron pre-damping ring to the main damping ring. These contain emittance diagnostics and beam dumps to allow tuning of the injector systems without operating portions of the ring complex.

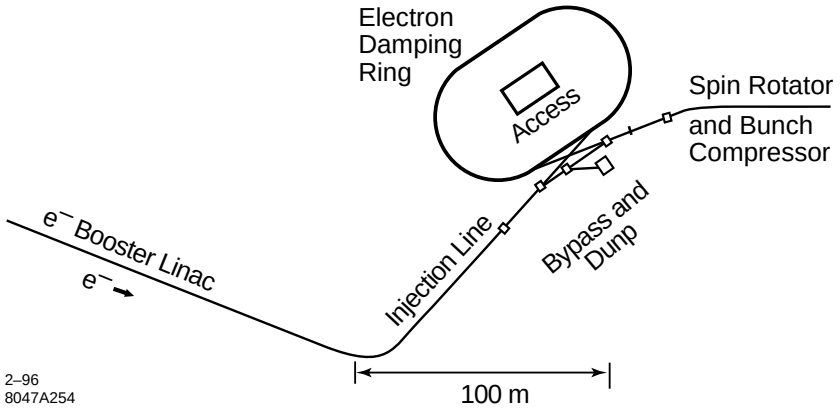

Figure 4-1. *Layout of electron damping ring system along with the two bunch compressors and the electron source.*

4.2.2 Damping Ring Complex Layout

The electron and positron damping ring systems are located at the low-energy ends of the respective linacs. The two systems are separated by roughly 20 km. On the extraction side, the systems are constrained by the prelinacs, the spin rotator in the low-energy bunch compressor which performs a 20° bend, and the bunch compressor turn-around (180° arc). At the injection end, the systems are constrained by the source linacs; the electron source is roughly 300 m in length while the positron source is in excess of 1 km.

The electron damping ring system includes an injection line with a 60° bend, and the ring injection and extraction sections which yield a net bending of roughly 20°. Figure 4-1 is a schematic of a possible layout.

The positron damping ring system also includes an injection line with a 60° bend, and the injection and extraction sections for both the pre-damping ring and the main damping rings. Figure 4-2 is a schematic of a possible layout which allows for the long positron source system.

4.2.3 Requirements

At this point, we will enter a more detail description of the damping ring requirements and the parameter determination. The primary requirements of the NLC damping rings are summarized in Table 4-2 where the limiting parameters are listed for each of the NLC energy upgrades. The rings must produce electron and positron beams with emittances of $\gamma\epsilon_x \leq 3 \times 10^{-6}$ m-rad and $\gamma\epsilon_y \leq 3 \times 10^{-8}$ m-rad at a repetition rate as high as 180 Hz. The beams in the damping rings consist of multiple trains of 90 bunches with a maximum single bunch charge of 1.31×10^{10} (this is 5% higher than the required charge at the IP to allow for beam loss due to collimation).

To satisfy these requirements, the damping ring complex is designed to operate with the parameters listed in Table 4-3 which exceed the requirements of all presently considered NLC upgrades. To provide operational flexibility, we are designing the rings to operate with a peak current roughly 20% higher than the nominal peak current. Many of the limiting requirements (damping times and bunch train lengths) are set by the NLC–Ic (500-GeV-c.m.) design and not the higher energy upgrades. The only parameter that increases in difficulty as the center-of-mass energy is upgraded is the beam charge. This is relevant for the design of the rf system and the vacuum chamber, and the study of collective effects (many of which depend upon the rf and chamber designs).

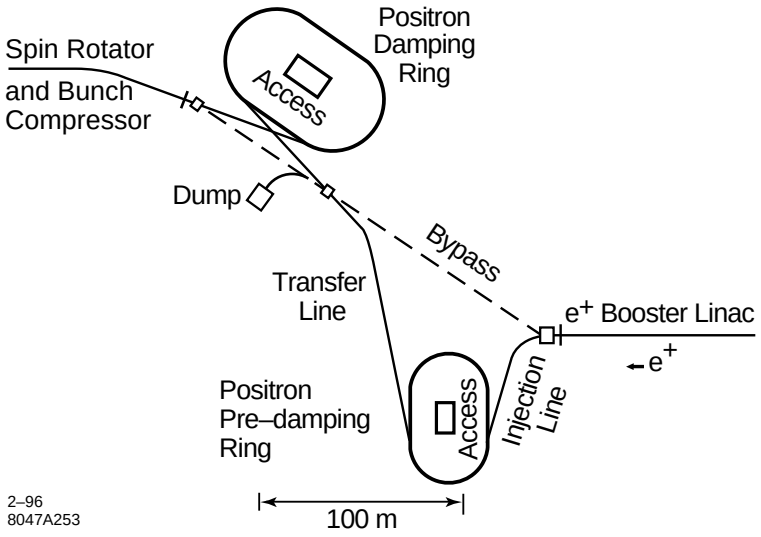

Figure 4-2. *Layout of positron damping ring complex along with the two bunch compressors and the positron source.*

	NLC–Ic (500 GeV)	NLC–IIc (1 TeV)	NLC–III (1.5 TeV)
$\gamma\epsilon_{x\,ext}$ $(10^{-6}$ m-rad$)$	3	3	3
$\gamma\epsilon_{y\,ext}$ $(10^{-8}$ m-rad$)$	3	3	3
Charge/Bunch (10^{10})	0.89	1.31	1.31
Bunches/Train	90	90	90
Bunch Spacing (ns)	1.4	1.4	1.4
Repetition Rate (Hz)	180	120	120

Table 4-2. *Damping ring beam requirements for NLC designs.*

$\gamma\epsilon_{x\,eq}$ / $\gamma\epsilon_{x\,ext}$ $(10^{-6}$ m-rad$)$	3.0 / 3.0
$\gamma\epsilon_{y\,eq}$ / $\gamma\epsilon_{y\,ext}$ $(10^{-8}$ m-rad$)$	2.0 / 3.0
Charge/Bunch	1.57×10^{10}
Bunches/Train	90 bunches/train
Bunch Spacing (ns)	1.4
Repetition Rate (Hz)	180

Table 4-3. *Requirements for NLC damping ring complex.*

	Injected Electrons	Injected Positrons
Charge/Bunch	1.9×10^{10}	2.5×10^{10}
$\gamma\epsilon_{x,y}$ (m-rad)	1×10^{-4} (rms)	0.06 (edge)
$\sigma_{\Delta E/E}$ (%)	1 (FWHM)	2 (FWHM)
$\Delta\gamma J$ (m-rad)	0.5×10^{-4} (rms)	0.03 (edge)
$\Delta E/E$ (%)	0.2 (rms)	0.2 (rms)

Table 4-4. *Electron and positron beams at entrance to damping rings.*

Table 4-4 lists the parameters of the beams assumed from the electron and positron injectors. The incoming electron emittance is specified as an rms value while the incoming positron emittance is specified as an edge emittance. The transverse injection errors are specified in units of the normalized actions and the permissible energy errors are given in %; the injection errors correspond to oscillation amplitudes that are equal to the rms and edge beam sizes for the electrons and positrons, respectively. Both of these values are set by the damping time requirements and not by the dynamic aperture or the multibunch sensitivity to transients both of which have looser tolerances.

4.2.4 Parameters: Damping Times and Equilibrium Emittances

At this point, we can discuss the parameters of the damping rings, in particular, the beam emittances and the required number of damping times. In a damping ring, the required number of damping times and the extracted emittances determine the primary parameters of the design. The emittances from the injectors are summarized in Table 4-4 for both the electrons and positrons and the requirements for the extracted beams are listed in Table 4-3. In examining these parameters, two points are immediately obvious.

First, the requirements for the positron and electron beams are extremely different. Because of the large incoming emittance, the injected positron beam needs substantially more damping and a much larger vacuum aperture. Therefore, we will use a pre-damping ring to damp the injected positron emittance to the level of the incoming electron beam. This allows us to partially separate the problems of large dynamic aperture, small equilibrium emittance, and fast damping. In addition, it allows us to design identical main damping rings for the electrons and positrons while the pre-damping ring is optimized for just the incoming positrons.

Second, the main damping rings must produce beams with a 100:1 emittance ratio, the vertical emittance being much smaller than the horizontal. Thus, the main rings will have to operate far from the coupling resonance. In a ring designed to produce flat beams, the vertical damping time is more critical than the horizontal and there is only one method of decreasing it: increased synchrotron radiation due to high-bending fields or damping wigglers. We will briefly discuss and discard other options subsequently.

In contrast, the pre-damping ring can operate on the difference coupling resonance since the extracted emittances of the pre-damping ring do not need to be asymmetric; the SLC damping rings operated in this mode until 1992 when it was decided to collide flat beams at the IP. Operating on the coupling resonance reduces the equilibrium emittance by a factor of two and it couples the horizontal damping partition into both planes, effectively increasing the vertical damping rate at the expense of the horizontal.

Now, we can specify the damping times and equilibrium emittances. Ideally, these determine the emittance of the extracted beam as expressed by:

$$\epsilon = \epsilon_i e^{-2N_\tau} + \epsilon_{eq}(1 - e^{-2N_\tau}) \quad , \tag{4.1}$$

	Main Damping Rings	Pre-damping Ring
Max. Injected $\gamma\epsilon_x$, $\gamma\epsilon_y$ (m-rad)	1.5×10^{-4}, 1.5×10^{-4}	0.09, 0.09 (edge)
Extracted $\gamma\epsilon_x$, $\gamma\epsilon_y$ (m-rad)	3×10^{-6}, 3×10^{-8}	1.5×10^{-4}, 1.5×10^{-4}
Equil. $\gamma\epsilon_{eq\,x}$, $\gamma\epsilon_{eq\,y}$ (m-rad)	3×10^{-6}, 2.0×10^{-8}	5×10^{-5}, 5×10^{-5}
$N_{\tau\,y}$	4.8	3.2
$\tau_{\rm eff}$ (ms)	1.16	1.74

Table 4-5. *Damping time requirements for NLC damping rings.*

where ϵ_i is the injected emittance, ϵ_{eq} is the equilibrium emittance, and N_τ is the number of damping times the beam has been stored. Because the damping needed in the vertical plane is greater than or equal to that in the horizontal while the damping rate in the vertical is less than or equal to that in the horizontal $(J_x \geq J_y)$, the number of damping times is determined from the vertical emittances. Table 4-5 lists the injected emittances from Table 4-4 assuming that the injection-offsets fully filament and add to the beam emittance. Then, we calculate the required number of vertical damping times for the pre- and main damping rings. We have assumed that the pre-damping ring is operating on the coupling resonance so that the extracted emittances are equal and we have assumed equilibrium vertical emittance of $\gamma\epsilon_{y\,eq} = 2.0 \times 10^{-8}$ m-rad for the main damping ring. Obviously, assuming a larger equilibrium vertical emittance in the main ring increases the required damping and therefore the difficulty of the design. Although requiring smaller a equilibrium emittances imposes stricter magnet and alignment tolerances, it is felt that the necessary alignment tolerances can be attained using beam-based alignment methods.

The NLC main damping rings will damp an injected beam vertical emittance of 1×10^{-4} to 7×10^{-9}. At the same time, we will design the rings to attain an equilibrium vertical emittance less than 2×10^{-8} m-rad; the tolerances are being specified to attain an expected vertical emittance of 1.5×10^{-8} m-rad. Thus, we are providing more damping that necessary. We believe that it is worthwhile investing in the additional damping capability since it provides stability against fluctuations in the incoming beam. Specifically, it allows for injection mismatches or other effects [1] that can increase the effective injected emittance by 50%. This additional damping will be reflected in the injection tolerance of $\gamma J_y \leq 0.5 \times 10^{-4}$. Finally, if necessary, the damping rates can be increased by operating the rings at a higher energy; the rings are being designed to operate at an energy between 1.8 GeV and 2.2 GeV with the nominal energy being 1.98 GeV.

Similar arguments apply to the pre-damping ring. Again, we want to keep the equilibrium emittance small to reduce the damping requirements. Because the pre-damping ring is coupled, the horizontal and vertical emittances and the horizontal and vertical damping rates are equal. In this case, we have chosen to design to coupled emittances of

$$\gamma\epsilon_{x,y\,\rm eq} \leq 5 \times 10^{-5}\ \text{m-rad} \qquad \text{(pre-DR)} \quad . \tag{4.2}$$

Although we have not included any margin in the damping time, we should note that in calculating the required number of damping times for the positron beam, we have used an effective rms injected emittance equal to 70% of the edge emittance.[2] At the time of this writing, we did not have details of the incoming positron beam distribution but

[1] In the SLC electron damping ring, the injected beam does not appear to damp at the expected damping rate during the first millisecond. The cause of this problem is unknown.

[2] When a beam is damped in a ring, the injected distribution is not modified until the emittance is damped close to the equilibrium emittance of the ring. Since an aperture limited beam, such as the incoming positrons, will not have a gaussian distribution, it is not reasonable to parameterize the emittance with the rms value. Instead, because we are interested in the core density of the beam, we will define the effective emittance using the FWHM: $\sigma_{\rm eff} = 0.4$ FWHM. Using this parameterization and assuming that the initial distribution is uniform, $\epsilon_{\rm eff} \approx 0.7\epsilon_{\rm edge}$. This is the value assumed for the pre-damping ring design.

this is undoubtedly an over-estimate of the effective rms emittance and therefore provides a margin on the damping requirements.

Finally, we can specify the required equilibrium horizontal emittance in the main damping rings. Since the rings are uncoupled and $J_x \geq J_y$, the horizontal damping time is less than or equal to the vertical. Therefore, the residual injected horizontal emittance is negligible and the horizontal emittance of the extracted beam is very nearly equal to the horizontal emittance of the ring:

$$\gamma\epsilon_{x\,\mathrm{eq}} \leq 3 \times 10^{-6}\,\text{m-rad} \qquad \text{(MDR)} \quad . \tag{4.3}$$

Now we can calculate the required damping times of the rings. The damping times are determined from the desired repetition rate (f_{rep}), the required number of damping times per bunch train (N_τ), and the number of trains stored simultaneously in the rings (N_{train}):

$$\tau_{x,y} \leq \frac{1}{f_{\mathrm{rep}}}\frac{N_{\mathrm{train}}}{N_\tau} \quad . \tag{4.4}$$

The maximum number of trains stored in the rings depends upon the length of the bunch trains and the rise and fall times of the injection and extraction kickers. The kicker rise and fall times depend upon the required kicker amplitude and stability [Mattison 1995]. The SLC damping ring kickers have rise and fall times of 60 ns. Although the stability requirements are tighter in the NLC main damping rings than in the SLC rings, the amplitude and physical design constraints are looser. Thus, it is thought that 60 ns will be sufficient for the rise and fall time of the NLC main damping ring kickers. The situation is different in the pre-damping ring. Here the amplitude requirements are more severe than those in the SLC rings but the stability requirements are comparable and again the physical design constraints are looser. Thus, again we feel that 60 ns will be sufficient for the rise and fall time of the pre-damping ring kickers.

Note that when damping multiple trains of bunches at the same time, the damping time *per se* is not the relevant parameter. Instead, we are concerned with the damping time scaled by the number of bunches in the ring which is roughly proportional to the ring circumference; two rings, one with twice the damping time but storing twice as many trains, will have the same damping performance. Thus, we define an effective damping time:

$$\tau_{\mathrm{eff}} \equiv \frac{\tau}{N_{\mathrm{train}}} = \tau\frac{T_{\mathrm{train}}}{T_0} \quad , \tag{4.5}$$

where T_{train} is the length required per bunch train including the gap between the trains, and T_0 is the ring circumference. The effective damping time then depends upon the repetition rate and the number of damping times per bunch. In the NLC main damping rings, the effective damping time is:

$$\tau_{\mathrm{eff}} \leq \frac{1}{f_{\mathrm{rep}}N_\tau} = 1.16\,\text{ms} \qquad \text{(EDR, PDR)} \quad , \tag{4.6}$$

while in the pre-damping ring

$$\tau_{\mathrm{eff}} \leq 1.74\,\text{ms} \qquad \text{(PPDR)} \quad . \tag{4.7}$$

4.2.5 Scaling Relations

Equations 4.2, 4.3, 4.6, and 4.7 determine the basic parameters. Initially to study these parameters we ignored the option of damping wigglers, assuming an isomagnetic ring, and we neglect the effect of intrabeam scattering. In this case, we can write simple expressions for $\gamma\epsilon_{x\,eq}$ and $\tau_{y\,\mathrm{eff}}$, the two quantities we wish to calculate:

$$\tau_{y\,\mathrm{eff}} = 1.69 \times 10^{14}\frac{T_{\mathrm{train}}}{\gamma^3 G_B} = \frac{2.88 \times 10^{12} T_{\mathrm{train}}}{B_0[kG]\gamma^2} \tag{4.8}$$

$$\gamma\epsilon_{x\,eq} = 3.84\times10^{-13}\frac{\gamma^3}{J_x}\langle\mathcal{H}\rangle_B G_B = \frac{65T_{\rm train}}{\tau_{y\,\rm eff}}\frac{\langle\mathcal{H}\rangle_B}{J_x} \quad . \tag{4.9}$$

Here, G_B is the inverse bending radius of the bending magnets, $\langle\mathcal{H}\rangle_B$ is the average of $\mathcal{H}_x$ over the bending magnets, B_0 is the magnetic field in kGauss, and we have assumed that $J_y = 1$. Finally, $T_{\rm train}$ is the train length which is determined by the length of the bunch train and the injection and extraction kickers.

Equations 4.8 and 4.9 show that the emittance of a ring can be decreased by reducing the dispersion in the bending magnets, reducing the strength of the bends, or decreasing the energy of the ring. Unfortunately, the damping times are increased by reducing the bending magnet strength or decreasing the energy of the ring. This implies that the dispersion in the bends is the only free parameter. Unfortunately, it is also constrained.

In the NLC design, we would like to limit the ring energy to roughly 2 GeV; reasons for this choice are discussed in Section 4.2.6. If we then apply these formula to the main damping rings, we find that we need a 30-kGauss bending field to attain the desired damping. This is not reasonable and therefore we consider additional methods of increasing the damping.

The most obvious method of increasing the damping is to use damping wigglers. Another method of increasing the damping is to change the horizontal damping partition. Unfortunately, this has no effect on the vertical damping if the ring is not coupled. Regardless, changing the horizontal damping partition will decrease the equilibrium horizontal emittance which is another quantity we need to reduce. The damping partition can be changed with a defocusing gradient in the bending magnets—Robinson wigglers are not effective because of the high dispersion that is needed [Raubenheimer 1988]. Unfortunately, damping wigglers reduce the change of J_x. Thus, to change J_x significantly, one is forced to use very high gradients in the bending magnets which makes the option less desirable.

The scaling formulas Eqs. 4.8 and 4.9 can be modified to include the effects of damping wigglers:

$$\tau_{y\,\rm eff} = \frac{2.88\times10^{12}T_{\rm train}}{B_0(kG)\gamma^2(1+F_w)} \tag{4.10}$$

$$\gamma\epsilon_{x0} = \frac{65T_{\rm train}}{\tau_{y\,\rm eff}(J_{x\,0}+F_w)}\frac{\left(\langle\mathcal{H}\rangle_B + 6\overline{\beta_x}F_w\rho_0/5\pi k_w^2\rho_w^3\right)}{\left(1+F_w\right)} \tag{4.11}$$

where $J_{x\,0}$ is the damping partition without wigglers and the parameter F_w is a measure of the effectiveness of the wigglers,

$$F_w \equiv \frac{L_w}{\pi}\frac{B_w^2}{B_0}\frac{1}{B\rho} = \frac{L_w}{\pi}\frac{\rho_0}{\rho_w^2} \quad . \tag{4.12}$$

In addition, L_w and B_w are the length and peak field of the wiggler; $\overline{\beta_x}$ is the average beta function in the wiggler, and k_w is the wiggler wave number, $k_w = 2\pi/\lambda_w$ where λ_w is the wiggler period. Also, ρ_0 and ρ_w are the bending radii of the main bends and the wiggler. Both bending radii are proportional to the energy over the respective magnetic fields. We have assumed sinusoidal wigglers, and thus the average of $B_w^2(s)$ over the wiggler is equal to $\frac{1}{2}\hat{B}_w^2$. In addition, we assume that $\overline{\beta_x} \gg \lambda_w/2\pi$ so that the $\eta_x'^2\beta_x$ term dominates in the excitation term from the wiggler.

As described in Section 4.2.7, in the NLC main damping ring design we have decided to equalize the contributions from the wigglers and the arcs to the radiation damping. This specifies that the term F_w is equal to 1. At this point, we can discuss the Halbach scaling formula for hybrid wigglers [Halbach 1985]:

$$B_w \le 3.44\exp\left[-\frac{g}{\lambda_w}\left(5.08 - 1.54\frac{g}{\lambda_w}\right)\right] \quad , \tag{4.13}$$

which is roughly valid for $0.08 < g/\lambda_w < 0.7$. This suggests that one can achieve a peak field of $B_w = 22$ kGauss (close to the saturation point of Vanadium Permendur) in a wiggler with a gap of 2 cm and a period of 20 cm. In

practice, this scaling result is optimistic when close to saturation but it provides a starting point from which one can determine the wiggler parameters.

4.2.6 Ring Energy

There are a number of considerations when determining the ring energy. First, the desire to maintain high-spin polarization while damping the beams suggests that the nominal ring energy should be chosen so that the spin tune is a half integer. This limits the energy to

$$E = (n + 0.5)440\,\text{MeV} \;= 1.10, 1.54, 1.98, 2.42, \cdots \text{GeV} \quad . \tag{4.14}$$

Second, we would prefer to keep the ring energy low for two primary reasons: it keeps the ring cost lower and it keeps the normalized longitudinal emittance small, making the bunch compression easier. The NLC requires that the damping ring bunch be compressed longitudinally by roughly a factor of 40. We do not want an uncorrelated energy spread much greater than 1% in the linac and thus we need to perform at least a portion of the bunch compression at an energy five times that of the damping ring. Unfortunately, at higher energies it becomes more difficult to perform the compression without degrading the beam emittances.

The problem with a low-energy ring is that it is harder to attain the required damping using reasonable magnet designs. We can understand the choices using the scaling formula. First, using Eqs. 4.10 and 4.12 and assuming that the fraction of damping due to the wigglers F_w and the wiggler peak field B_w are fixed, we find that, to meet the damping time requirements, the main bending field and the required length of wiggler scale as

$$B_0 \sim \frac{1}{\gamma^2} \qquad \text{and} \qquad L_w \sim \frac{1}{\gamma} \quad . \tag{4.15}$$

Thus, as the ring energy is increased, the bending magnets and wigglers become easier to design and construct.

Next, using Eq. 4.11 and noting that the dispersion invariant scales as $\langle \mathcal{H} \rangle_B \sim \Theta^3 \rho_0 \sim \Theta^3 \gamma / B_0$, we find that, to maintain the equilibrium emittance,

$$N_{\text{cell}} \sim \gamma \quad \text{and} \quad L_{\text{bend}} \sim \gamma^2 \quad . \tag{4.16}$$

Finally, given these relations, the length of the ring, the momentum compaction, and the synchrotron radiation power must scale as

$$L_{\text{ring}} \sim \gamma^3 \quad \text{and} \quad \alpha_p \sim 1/\gamma^2 \quad \text{and} \quad P_{SR} \sim U_0 \sim \gamma \quad , \tag{4.17}$$

where we assumed that the cell length scales in the same manner as the length of the bends. The cost of the rings will tend to increase with the length, while the cost of the rf systems will increase with the power required; both of these costs will increase with higher energy. In addition, the momentum compaction decreases with the square of the ring energy while rough scaling for the longitudinal microwave threshold scales as $\gamma \alpha_p$. This suggests that longitudinal stability may be more difficult at higher energy.

Thus, the determination of the nominal ring energy becomes an optimization between the difficulty of the bending and wiggler magnets versus the decrease in momentum compaction, and the increase in size and cost of the ring. We should attempt a cost optimization, but for this iteration of the NLC damping ring design, we have picked an energy of 1.98 GeV and a spin tune of roughly 4.5. This is the lowest energy that appears to yield reasonable designs for the bending magnets and wigglers. Of course, during operation, we may want to vary the ring energy to optimize for a lower repetition rate or a larger injected emittance. For this reason, we are designing the rings to operate over the 1.8–2.2-GeV range; this range extends between the two nearby integer spin resonances.

Finally, it is worth noting that intrabeam scattering does not present justification for increasing the ring energy. *When the effective damping times are held constant*, the emittance growth due to intrabeam scattering does not decrease with the ring energy [Raubenheimer 1991]. Using very simple scaling formula, the emittance growth depends upon the intrabeam scattering growth rate compared to the synchrotron radiation damping. The intrabeam scattering growth rate scales roughly as

$$\tau_{x\,\mathrm{IBS}}^{-1} \sim \frac{N\langle\mathcal{H}\rangle}{\gamma\epsilon_x\gamma\epsilon_y\gamma\epsilon_z} \tag{4.18}$$

which, for given normalized emittances, is independent of energy, while the damping rates scale inversely with the ring length which increases as γ^3. Thus, emittance growth due to intrabeam scattering actually becomes worse as the design energy is increased.

4.2.7 Wigglers vs. Arcs

At this point, we can discuss the difference between designing a wiggler with arcs or a ring with wigglers. In the former, the radiation damping in the wiggler dominates the radiation damping in the arcs, *i.e.*, the parameter F_w is much greater than 1. In this case, the contribution of the quantum excitation in the arcs is suppressed by roughly a factor of $(1 + F_w)^2$. This allows one to design the arcs with a much larger dispersion which leads to a larger contribution to the momentum compaction and makes the chromatic correction easier. Unfortunately, the gains in the momentum compaction and chromatic correction are partially offset by the additional length of wiggler that is required.

The Japan Linear Collider (JLC) damping rings [JLC] are an example of this design style. There, roughly 80% of the damping is performed in the wigglers and the requirements on the arcs are substantially reduced. But, the JLC design requires 140 m of high-field wiggler and the momentum compaction and dynamic aperture, if larger at all, do not appear to be significantly larger.

For the NLC main damping ring design, we have decided to pursue another approach: we want to divide the radiation damping equally between the arcs and the damping wiggler. We feel that this is a more efficient use of magnets and space. It exchanges some of the difficulties of dealing with a very long wiggler system with the arcs. Preliminary comparisons between the JLC and NLC rings show that they both have similar performance expectations.

4.2.8 Lattice Specification

At this point, we can apply the scaling formula to estimate the parameters for the NLC damping rings. First, we can estimate the bending field required in the pre-damping ring to meet the damping time requirements. The pre-damping ring needs to attain an effective damping time of $\tau_{y\,\mathrm{eff}} = 1.74\,\mathrm{ms}$ (Eq. 4.7). Assuming that damping wigglers are not used, limiting the change to the horizontal damping partition to $J_x = 1.3$, and allowing 60 ns for the rise and fall times of the injection and extraction kickers, Eq. 4.10 shows that the bending field must be $B_0 = 17.5\,\mathrm{kGauss}$; this is comfortably below the saturation point of standard magnet iron. Two points to note: first, the required field is independent of the number of trains stored in the ring at once, and second, without changing J_x, the required field would be 20 kGauss which is quite high.

A similar procedure can be used to estimate the bending fields and wigglers fields required in the main damping rings. Assuming that wigglers are used to perform half the required damping and that the bunch trains are separated by 60 ns, Eq. 4.10 shows that the bending field must be $B_0 = 15.1\,\mathrm{kGauss}$. If we limit the peak wiggler field to 22 kGauss, Eq. 4.12 shows that we need 26 m of wiggler.

Now, we have to specify a lattice that will meet the emittance requirements. For the main damping ring, we have considered four different lattice cell structures: a FOBO cell, which is a FODO cell where the defocusing quadrupole is replaced by a bending magnet with a defocusing gradient, a Chasman-Green lattice, a Triple Bend Achromat (TBA) lattice, and a Theoretical Minimum Emittance (TME) lattice. The advantages and disadvantages of each are summarized below:

- FOBO
  - \+ Simple FODO-like structure with well-constrained beta-functions
  - – Uses three quadrupoles per bending magnet (assuming symmetric form)
  - – Less efficient at generating emittance
  - – Difficult combined function bending magnet
- Chasman-Green
  - \+ Fairly efficient at generating emittance
  - \+ Two quadrupoles per bending magnet
  - \+ Excellent dynamic aperture behavior in R. Brinkmann's comparison [Brinkmann 1990].
  - \+ Presently used at ESRF and ELETTRA
- TBA
  - \+ Fairly efficient at generating emittance
  - \+ Two quadrupoles per bending magnet
  - \+ Presently utilized at ALS and PLS
- TME
  - \+ Very efficient at generating emittance (fewer bends)
  - \+ Easy to optimize ratio of α_p and $\mathcal{H}$
  - \+ Excellent dynamic aperture in studies
  - – Three quadrupoles per bending magnet

To study the different structures, we made preliminary designs for the NLC main damping rings using each of these four lattices [Moshammer 1993]; the rings were designed in a race-track form with two arcs, including dispersion suppressors, and roughly 10 m of straight section which could be expanded into injection and extraction and wiggler sections. Parameters and tracking results for the four designs are listed in Table 4-6 and the cell lattice functions are plotted in Figures 4-3, 4-4, 4-5, and 4-6. Notice that the dispersion is not matched to zero at the ends of the Chasman-Green and TBA cells; zero dispersion is not necessary after most cells in the ring and one can obtain smaller emittances by matching to nonzero values. The only advantage these preliminary results indicated was that for equal ring energy, the TME design used fewer and longer bending magnets with lower field gradients. This was thought to be sufficiently important that it outweighed the advantage of using a more standard lattice such as the Chasman-Green or TBA. Thus, we decided to complete a design based upon the TME structure and study the other lattices further in the future.

The optimization is different in the positron pre-damping ring. Here, the equilibrium emittance is easily attained and the primary issues become attaining the desired dynamic aperture and constraining the beta-functions to keep the

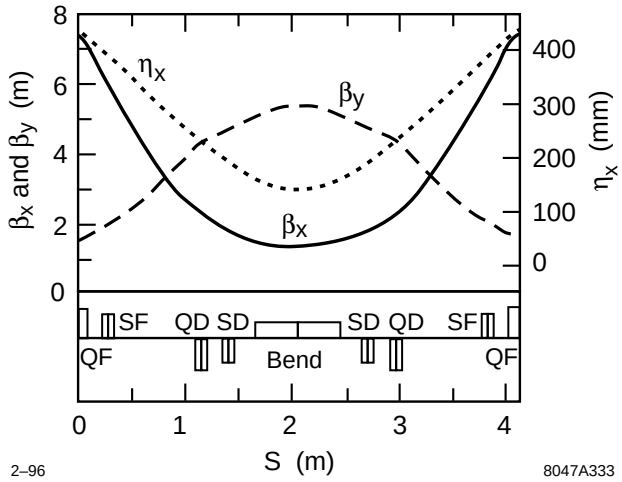

Figure 4-3. *Lattice functions in a FOBO cell.*

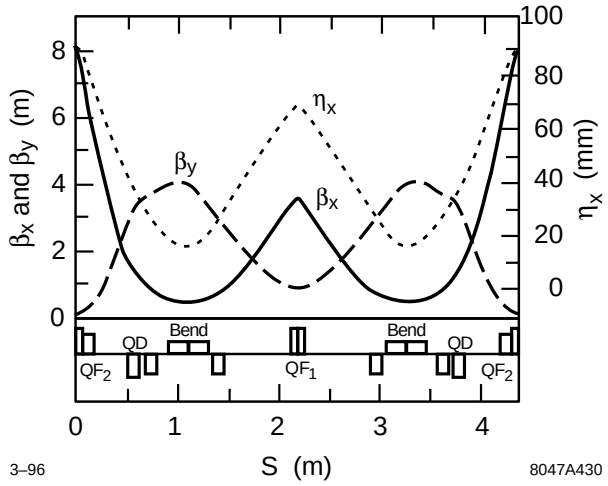

Figure 4-4. *Lattice functions in a Chasman-Green cell.*

Lattice (GeV)	Energy $(10^{-6}$ m-rad)	$\gamma\epsilon_{x\,\mathrm{eq}}$ (10^{-3})	α_p (m)	Circ.	N_{bends} $(10^{-3}$ m-rad)	Norm. Accept. X/Y
FOBO	2.2	4.4	1.4	133	80	36 / 17
Chasman-Green	2.0	3.0	0.6	154	72	4 / 14
TBA	2.0	3.4	0.7	177	72	14 / 10
TME	2.0	3.2	0.7	158	40	36 / 26

Table 4-6. *Parameters for different lattice structures [Moshammer, 1993].*

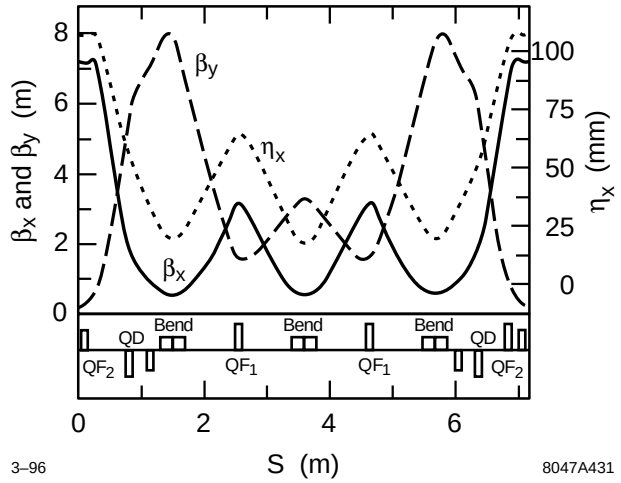

Figure 4-5. *Lattice functions in a TBA cell.*

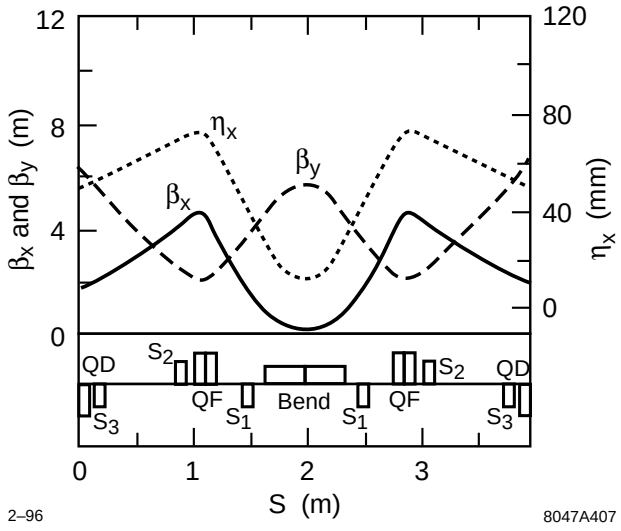

Figure 4-6. *Lattice functions in a TME cell.*

required vacuum aperture relatively small. The FOBO lattice which is basically a simple FODO structure seems to be the best choice in this case; typical lattice functions are plotted in Figure 4-3. The FOBO structure was felt to be superior to the more standard FODO structure because it allows one to increase the horizontal damping partition and thus increase the transverse damping rates when the ring operates on the betatron coupling resonance.

4.2.9 RF Parameters

In both the pre-damping ring and the main damping rings, the rf is chosen to be 714 MHz. This is as low as consistent with the bunch spacing of 1.4 ns. There are several advantages of the low-frequency choice. First, for a given rf voltage, the lower frequency has a higher stored energy in the cavities thereby reducing the beam loading and the bunch-to-bunch synchronous phase shift. Second, the coupled-bunch instability driven by the fundamental mode of the cavities has a smaller growth rate. Finally, two other advantages of the lower frequency is the increased bunch length in the main damping rings and the larger energy acceptance in the pre-damping ring.

The minimum rf voltage is determined by the synchrotron radiation, HOM losses, and the height of the energy bucket. In the pre-damping ring, we would need an rf voltage in excess of 3.5 MV to capture the full $\pm 2\%$ incoming energy spread. Instead, we use an energy compressor to reduce the injected energy spread at the expense of increasing the bunch length. We expect the compressor will be able to reduce the incoming energy spread by a factor of two. With the compressor, an rf voltage of 2.0 MV should be sufficient; this provides an energy bucket of $\pm 1.5\%$.

In the main damping rings, we are designing for an rf voltage of 1.0 MV. This is the lowest voltage that is consistent with the energy loss per turn of roughly 700 kV. The main rings have a very small momentum compaction and we want to keep the voltage low to keep the bunch length relatively long. Space is being left in the design to allow for future upgrades of the rf system to 1.5 or 2.0 MV.

Finally, the harmonic number of the rings is chosen to allow operation with fewer, but possibly longer, bunch trains at a reduced repetition rate. Since one would like to place the trains symmetrically in the ring, this requires that the harmonic number be a multiple of all the different numbers of trains being considered. Thus, while the PPDR has been designed to damp three trains of bunches at the same time, we have chosen an even harmonic number so that it could also operate with two evenly spaced bunch trains. Similarly, the EDR and PDR have been designed to operate with four trains of bunches at a 180-Hz repetition rate. To allow for operation with three bunch trains at 120 Hz, the harmonic number should be a multiple of 4 and 3. Unfortunately, the present design has a harmonic number of 532 which is not ideal. In the next design iteration, the rings will be modified to have an harmonic number of 540.

Finally, it should be noted that the harmonic numbers of the rings do not need to be related from timing considerations because only single bunch trains are injected on any machine cycle. In particular, the PPDR has a slightly larger gap between bunch trains allow more time for the injection and extraction kickers to rise and fall.

4.3 Lattice Design

In this section, we will describe the layouts and optics of the main damping rings, the pre-damping ring, the injection and extraction transport lines, and the PPDR to PDR transport line. After describing the optical designs, we will discuss the lattice related accelerator physics issues. This includes trajectory correction, emittance control and matching, dynamic and energy apertures, and polarization. These are all low-current effects. Collective effects are discussed in Section 4.4 and the rf and vacuum systems are described in Sections 4.5 and 4.6. In addition, the feedback systems

and support and alignment systems are described in Sections 4.7 and 4.9 and the magnet and diagnostics designs are describe in Sections 4.10 and 4.11.

At the time of this writing, the design of the main damping ring is fairly complete. We do not feel that there are any significant flaws in the design although a lot of detailed engineering is still required; this is particularly true of the rf cavities and the bending magnets. The only significant modification currently planned is increasing the ring circumference to increase the harmonic number from 532 to 540; this will facilitate operation with either 4 or 3 bunch trains. The circumference change will be made by increasing the length of the two straight sections by roughly 1.7 meters which will have the side benefit of making the vacuum chamber design simpler in the wiggler region.

The design of the pre-damping ring has not yet been investigated in the same depth as the main damping ring design. At this time, we have a design that appears to meet all of the requirements but many of the component designs have not yet been considered. As stated in the introduction, our belief is that the pre-damping ring is significantly more straightforward than the main damping rings except for two issues: the injection and extraction systems and the dynamic aperture. Both of these arise from the very large injected beam emittances and both of these are addressed in our design.

4.3.1 Main Damping Rings

As described, the Electron and Positron Damping Rings (EDR and PDR) are designed to damp beams with an injected emittance of $\gamma\epsilon_{x,y} = 1 \times 10^{-4}$ m-rad to an emittance of $\gamma\epsilon_x = 3 \times 10^{-6}$ m-rad and $\gamma\epsilon_y = 3 \times 10^{-8}$ m-rad. The damping and emittance requirements on the rings are described in Section 4.2.3. The determination of the design parameters is discussed in Sections 4.2.6–4.2.9; these parameters are summarized in Table 4-7.

The lattice is based on detuned Theoretical Minimum Emittance (TME) cells which were chosen because of eased requirements on the bending magnets. The chromaticity is corrected with three families of sextupoles and the dynamic aperture is more than sufficient. The damping is performed using both high-field bending magnets and a damping wiggler. The bunch trains are injected onto and extracted from the closed orbit using pulsed kickers and DC septa. Finally, all of the quadrupoles and all of the sextupoles will have independent power supplies. This facilitates beam-based alignment as well as matching of the lattice functions; both of these are important for attaining the desired vertical emittance.

In the next sections, we will describe the ring layout and then details of the ring lattice: the arcs and the dispersion suppressors, the wiggler and injection and extraction straight sections, and the placement of the rf cavities. In addition, the rf and vacuum systems are described in Sections 4.5 and 4.6 while the feedback systems and support and alignment systems are described in Sections 4.7 and 4.9. Finally, the magnet and diagnostics designs are describe in Sections 4.10 and 4.11.

Layout

The NLC main damping rings are roughly 223 m in circumference and measure 50 m by 80 m. They have a nominal energy of 1.98 GeV and required damping is achieved using both high field bending magnets and roughly 26 m of damping wiggler. The rings are designed in a race-track form with two arcs separated by straight sections; the layout is illustrated in Figure 4-7. Each arc consists of 19 TME cells plus dispersion matching sections. The straight sections are roughly 30 m in length. On one side of the ring, the straight section is devoted to the damping wigglers while the other straight section contains the injection and extraction components and the rf cavities. The arc cells, which are roughly 4 m in length, have one bending magnet, six sextupole magnets, three quadrupoles, and their own integral vacuum chamber. The wiggler straight section consists of 10 separate wiggler sections. The injection and extraction

Energy	$1.8 \sim 2.2$ GeV; 1.98 GeV nominal
Circ.	223 m
Max. Current	1.2 A
Max. N_{bunch}	1.57×10^{10}
Trains	4 trains of 90 bunches
Train Separation	60 ns
Bunch Separation	1.4 ns
Max. Rep. Rate	180 Hz
ν_x, ν_y, ν_s	23.81, 8.62, 0.004
$\gamma\epsilon_x$	2.56×10^{-6} m-rad
$\gamma\epsilon_x$, $\gamma\epsilon_y$ with IBS	3.1×10^{-6} m-rad, 1.5×10^{-8} m-rad
σ_ϵ	0.09%
σ_z	4.0 mm
$\xi_{x\ \mathrm{uncorr}}, \xi_{y\ \mathrm{uncorr}}$	-41.8, -22.4
τ_x, τ_y, τ_z	4.06 ms, 4.62 ms, 2.50 ms
U_{SR}	644 KV/turn
J_x	1.14
α_p	0.00047
V_{RF}	1.0 MV
f_{RF}	714 MHz
Lattice	40 TME Cells

Table 4-7. *Parameters for main damping ring (vers. 6.11)*

straight section contains: two kicker magnets and two septa for injection and extraction, two rf cavities, feedback striplines, and thirteen quadrupoles. Other components such as polarization monitors, optical monitors, and wire scanners will be added to this section.

At this time, we have not investigated the civil construction of the damping ring enclosures. Ideally, to minimize the disturbance to the ground, the ring enclosure will be constructed as a tunnel and not a vault. Although only schematically illustrated in Figure 4-7, the design goal will be to place all electronics, power supplies, kicker thyratrons, and rf klystrons in an accessible shielded region at the center of the ring. This will minimize cable and waveguide distances while allowing for maintenance and repair during operation.

Arcs

Each arc consists of 19 TME cells plus dispersion matching sections. Optimized TME cells are designed to attain the minimum emittance that is possible in a bending magnet. To do this, three quadrupoles are placed between the bending magnets and are used to minimize the average dispersion invariant $\mathcal{H}$ through the bending magnets. In general, this minimum is found when the dispersion and horizontal beta functions have minima at the center of the dipoles. Explicitly, the minimum emittance should be found when [Teng 1985]

$$\beta_{x\,0}^{TME} \approx \frac{L_B}{\sqrt{60}} \qquad \eta_{x\,0}^{TME} \approx \frac{L_B^2}{24\rho} \tag{4.19}$$

where β_0 and η_0 are the values at the center of the dipole and L_B is the length of the dipole.

Unfortunately, minimizing $\langle\mathcal{H}\rangle$ also implies a small value of the momentum compaction. We would like to keep the momentum compaction large since this eases the requirements on the longitudinal impedance due to the longitudinal

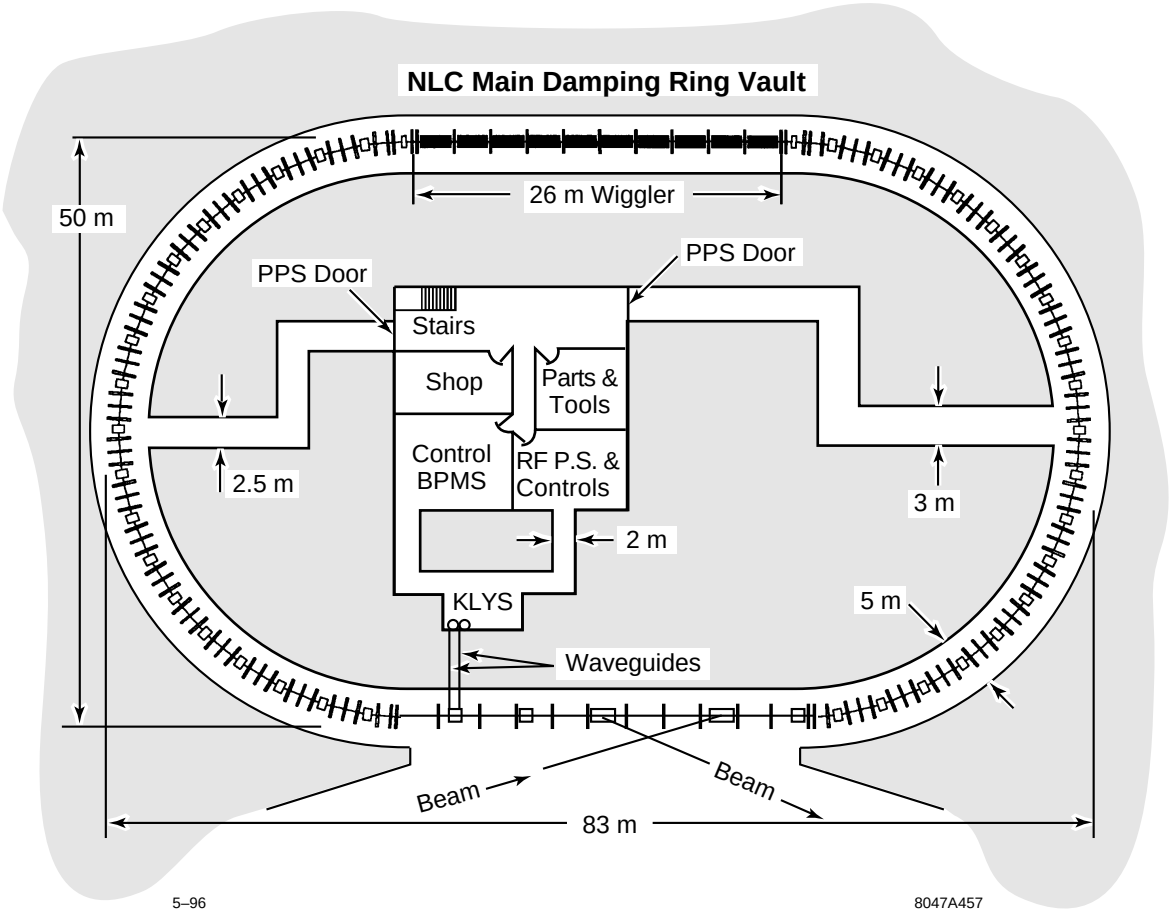

Figure 4-7. *Layout of main damping ring.*

microwave instability and it leads to a longer bunch length which is also desirable. Thus, we chose parameters in the cells to optimize the ratio of I_1/I_5 for a given bending angle rather than $\mathcal{H}$ (or I_5). In this case, the optimal values of the dispersion at the center of the bending magnet is equal to

$$\eta_0^\star \approx -\frac{L_B^2}{24\rho} + \frac{L_B}{\sqrt{15}}\sqrt{2L_B^2 + 5\beta_0^2} \quad . \tag{4.20}$$

This value is actually close the the optimal TME value.

In Figure 4-8, we plot the variation of I_5 (solid), which is proportional to $\mathcal{H}$, and I_5/I_1 (dashes), which is proportional to the ratio of $\mathcal{H}$ to α_p, versus β_0 for the case when $\eta_0 = \eta_0^\star$. Notice that both curves have minima near the optimum beta function but do not increase very rapidly as β_0 is increased. In practice, we detune the cell so that $\beta_0 \approx 2\beta_0^{TME}$; this reduces the chromaticity. In Figure 4-9, we plot the variation of I_5 (solid) and I_5/I_1 (dashes) against η_0 for $\beta_0 = 2\beta_0^{TME}$. In this case, the optimum $\mathcal{H}$ occurs at roughly η_0^{TME} while the optimum $\mathcal{H}/\alpha_p$ occurs around $\eta_0 \approx 2\eta_0^{TME}$. We have chosen to optimize the cells to this latter value.

Each TME cell consists of two QF quadrupoles, a single QD quadrupole, and a single bending magnet with a defocusing gradient. The defocusing gradient in the bending magnets increases both the quantum excitation and J_x. In a ring without damping wigglers, the increase in J_x is larger than the increase in the excitation and the equilibrium

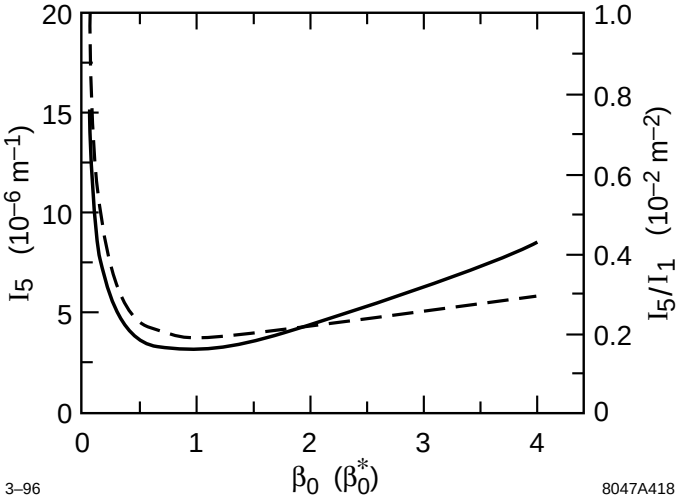

Figure 4-8. *I_5 (solid) and I_5/I_1 (dashes) versus β_0 for TME cells.*

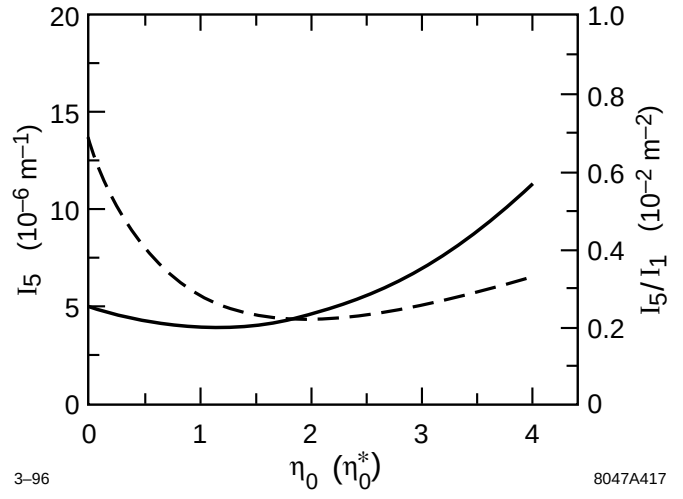

Figure 4-9. *I_5 (solid) and I_5/I_1 (dashes) versus η_0 for TME cells.*

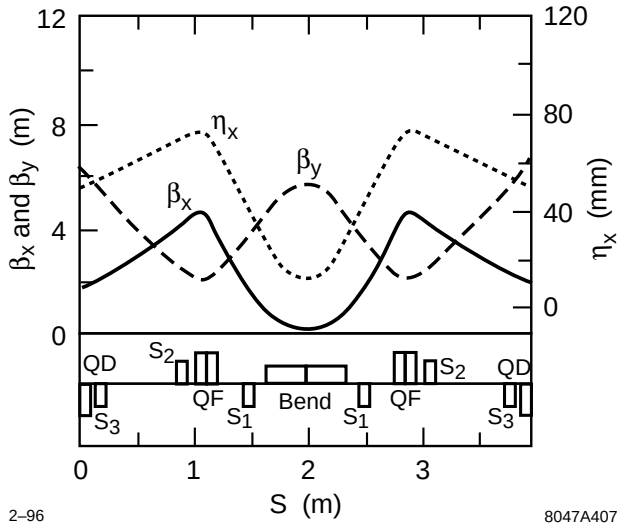

Figure 4-10. *β_x (solid), β_y (dashes), and η_x (dots) in main damping ring cell.*

emittance can be decreased by as much as a factor of two. But, the emittance and damping time reduction is less when damping wigglers are included since they reduce the change to J_x for a given gradient. Because the main damping rings do not need the additional horizontal damping and because it takes large gradients to achieve a significant reduction in the emittance, we have chosen a gradient that optimizes the matching through the cells while producing $J_x = 1.14$.

The length of each cell is roughly 3.9 m. The vacuum chamber is circular with a 1.25-cm inner radius and an antechamber is needed to handle the intense synchrotron radiation. The lattice functions for a cell are plotted in Figure 4-10 and the component layout is illustrated in Figure 4-11. The magnets and vacuum system are described in Sections 4.10 and 4.6.1, respectively.

The dipole steering correction is performed using trim windings on the sextupoles. There are two horizontal correctors and one vertical corrector in each cell. In addition, there are three button BPMs per cell. These are located at the sextupole magnets on either side of the bending magnet and one of the sextupoles adjacent to the defocusing quadrupole.

The chromatic correction is performed using three sextupole families in the arcs as illustrated in Figure 4-10. There is one defocusing family placed on either side of the bending magnets and a focusing and defocusing sextupole placed adjacent to the focusing and defocusing quadrupoles. Thus, there are six sextupoles per cell. At this time, it is not believed that additional sextupoles located in nondispersive regions or additional families of sextupoles are needed. The three sextupole families allow us to correct the chromaticities while also minimizing the tune shift with amplitude terms. This yields a dynamic aperture that is more than sufficient (Section 4.3.9).

Finally, the dispersion is matched to zero at the end of the arcs for the two straight sections. The matching is performed using the three upstream quadrupoles and a bending magnet with an integrated strength that is half of the arc bending magnets. We have assumed that the magnetic field of the matching bends is decreased to reduce excessive fringing fields. The gradient is scaled at the same time so that the matching bends can be constructed using the same pole shape as the main ring bends.

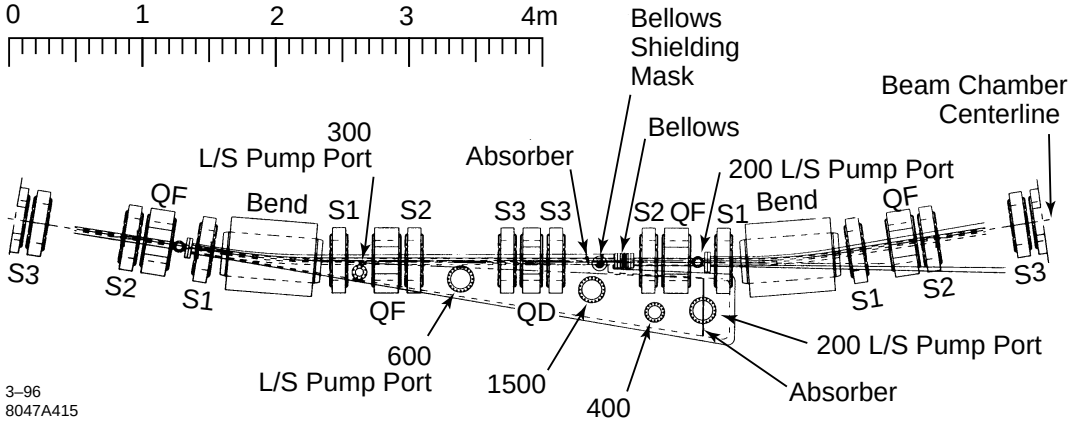

Figure 4-11. *Cell layout in a main damping ring cell showing magnet and vacuum chamber components; note the bending magnets are drawn as "H" magnets although the present design utilizes "C" bending magnets.*

The horizontal and vertical dispersion matching will be tuned using the matching quadrupoles, which have individual power supplies, and trim windings on the adjacent sextupoles that will be wired as skew quadrupoles. Four additional skew quadrupole windings are located in each arc for local correction of the vertical dispersion which is the most important contribution to the vertical emittance; this is discussed further in Section 4.3.8.

Wiggler Region

The wiggler region consists of five FODO cells with 3.0-m drifts between the quadrupoles. There are ten 2.6-m wiggler sections to be placed within the region with roughly 21 cm of space between the wiggler ends and the quadrupoles. The wigglers have a 2-cm full gap. To handle the intense synchrotron radiation, the vacuum chamber will have integrated pumping in ante-chambers on both sides of beam chamber. The adjacent quadrupoles have a 3-cm pole-tip radius so that they fit around the chamber. The wiggler magnet sections are described in Section 4.10.1: "Wiggler Magnets".

To minimize the emittance growth in the wigglers, we need to minimize the average horizontal beta function through the region. The average beta function is minimized at a phase advance of roughly 101.5° per cell, but this is a flat minimum and the chromaticity per cell increases rapidly as the phase advance increases. Thus, we have chosen horizontal and vertical phase advances of roughly 90° and 60° per cell.

The lattice functions are matched from the dispersion suppressors with two quadrupoles immediately following the suppressor and the first two quadrupoles at either end of the wiggler region. This allows the region to remain matched if the wiggler strength is varied. The lattice functions from the last TME cell through the wiggler region are plotted in Figure 4-12.

The dipole steering correction will be performed using trim windings on the quadrupoles wired as dipoles and button BPMs located next to the quadrupoles. The BPMs will be shielded to protect them from the large angle (low energy) synchrotron radiation.

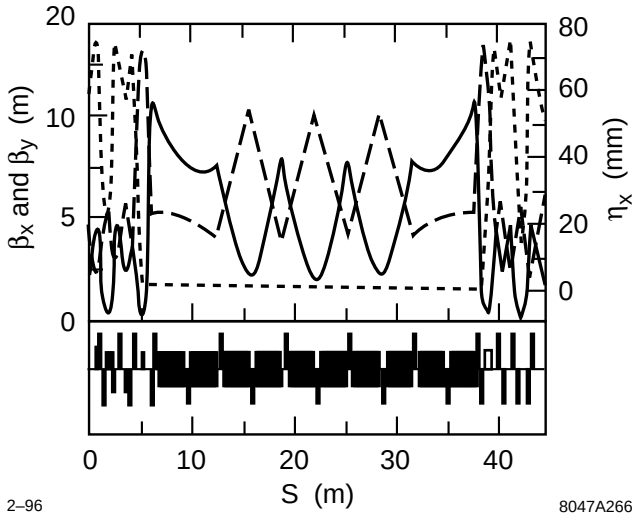

Figure 4-12. *β_x (solid), β_y (dashes), and η_x (dots) in main damping ring wiggler region.*

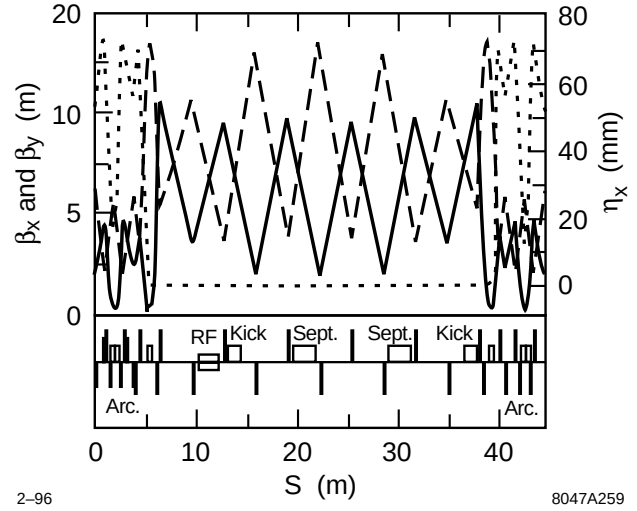

Figure 4-13. *β_x (solid), β_y (dashes), and η_x (dots) in main damping ring injection and extraction region.*

Injection-Extraction Region

The beams are injected and extracted in the injection-extraction straight section. To reduce the rf transients, beams are injected and extracted simultaneously. In this way, the beam current through the rf cavities is not interrupted.

The injection-extraction region is simply a mirror image of the wiggler region. It consists of five FODO cells with 3.0-m drifts between quadrupoles. The matching of the lattice functions is performed with four matching quadrupoles at either end of the region. The placement of the kickers and septa is illustrated in Figures 4-13 and 4-14 and the extracted beam trajectory, along with the position of the septum blade, is illustrated in Figure 4-15.

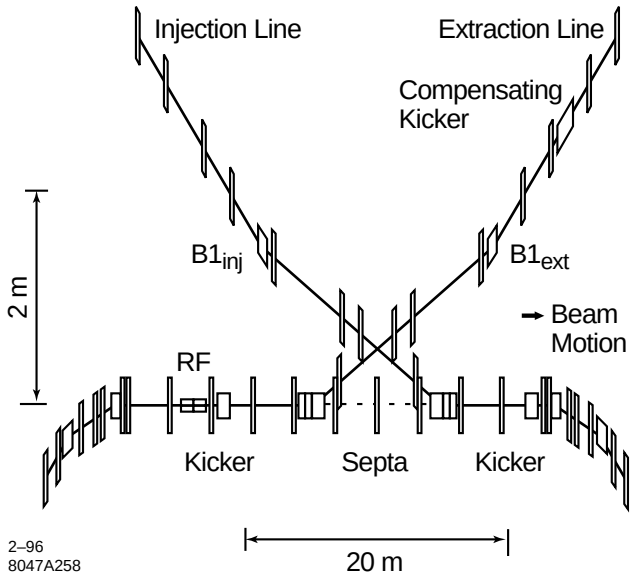

Figure 4-14. *Component layout in the main damping ring injection and extraction region.*

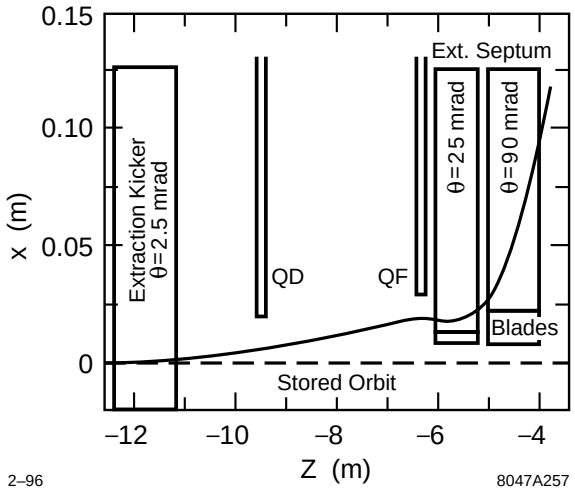

Figure 4-15. *Extracted beam trajectory from kicker through septum.*

The steering correction in this region will be performed using air-core dipole magnets. Experience with the SLC damping rings has illustrated the need for orthogonal horizontal and vertical angle and position closed orbit bumps through each of the septa as well as control of the injected and extracted beam trajectories.

The kickers are 1.2 m in length and provide a 2.5-mr horizontal deflection; these are described further in Section 4.10.3.

The septa are DC current sheet septa constructed in two pieces. The first septum is 83-cm long and provides a 25-mr deflection. The blade has a thickness of 5 mm and lies 9 mm from the stored beam where the residual field is negligible. The injected and extracted beam trajectories have 4.5-mm clearance from the blade; assuming an emittance of 10^{-4} m-rad, the 3-sigma horizontal beam size is 1.5 mm. The second septum is 1-m long and it provides a 90-mr deflection. The blade has a thickness of 15 mm and lies 9 mm from the stored beam where again the residual field is negligible. Both sections of the septum magnet are described further in Section 4.10.1.

The adjacent focusing quadrupoles need to have a 3-cm pole-tip radius to provide room for the injected or extracted beams, while the adjacent defocusing quadrupoles may need to include an entrance or exit beam line; at the adjacent defocusing quadrupoles, the injection and extraction trajectories are roughly 25 cm from the stored beam trajectory.

The injection and extraction lines cross about 60 cm from the stored beam trajectory. Initial calculations of the effect of the crossing suggest that the effect of the beams passing through each other is not insignificant. Thus, a vertical chicane will probably be used to deflect the incoming beam trajectory away from the extracted beam. The closest magnets are 1.2-m away from the crossing and thus there is plenty of longitudinal space for the chicane but attention will need to be given to the effect of the fringing fields on the extracted beam.

To reduce the tolerances on the septum field stability, a compensating bend B_1, which is powered in series with the septum, is located after the beam crossing on both the injection and extraction lines. Four quadrupoles are used to match the R_{22} transport element so that field fluctuations will cancel. This will ease the septum field tolerances by roughly an order of magnitude to $\Delta I/I \sim 5 \times 10^{-5}$.

In the same manner, the effects of kicker jitter on the extracted beam will be reduced using an achromatic (double) kicker scheme. Here, a compensation kicker is located in the extraction line after the septum compensation bend. Two additional quadrupoles are used to match the compensation kicker so that it is separated from the extraction kicker by a $+I$ transform in the horizontal plane. The compensation kicker is powered from the same thyratrons as the extraction kicker and is expected to reduce the sensitivity to kicker jitter by at least a factor of four. This will ease the tolerance $\Delta\theta/\theta$ on the extraction kicker from 0.0005 to 0.002. A similar achromatic kicker system will be tested at the ATF damping ring at KEK.

In addition, the sensitivity of the stored beam to the trailing edge of the kicker pulses is reduced by separating the injection and extraction kickers by $+I$ and adjusting the falling edge of the injection kicker to compensate for that of the extraction kicker; this can be done using a separate pulser as discussed in Section 4.10.3. Furthermore, the bunch trains will be ordered in the ring so that the trailing edge of the kicker pulse only effects the most recently injected bunch train allowing any residual deflection to be damped.

Finally, we should note that this injection and extraction region requires fairly difficult septa and kicker magnets. Although the magnets are thought to be possible, we also considered an alternate design that would require weaker kicker magnets. The alternate design consisted of two FODO cells with 5-m drift sections between quadrupoles. In this case, there is only one septum, a septum quadrupole, which both the injected and extracted beams use. Two of the disadvantages of this design were that the two beams must pass through each other and the resulting deflects of the extracted bunches can be as large as $0.2\sigma_y$ and the field tolerances in the septum quadrupole were very tight. For these reasons, we are not considering this design further.

RF Cavities

The rf cavities are located in a 3-m drift section before the extraction kicker; the cavity placement is illustrated schematically in Figures 4-13. The present rf design specifies two rf cavities, but the rf cavities and associated tapers are roughly 50 cm in length and thus additional cavities could be installed if necessary. In these sections, the dispersion is zero and the horizontal and vertical beta functions are roughly 6 m. It is expected that the cavity aperture will be roughly twice the nominal vacuum chamber radius and thus special masks will not be needed to protect the cavities from beam loss during injection or synchrotron radiation.

Detuned Lattice

We have studied a detuned version of the lattice for the main damping rings. The optics has an equilibrium emittance and a momentum compaction that are both roughly twice as large as the nominal lattice. In addition, the quadrupole and sextupole strengths are reduced by 30% while the dynamic aperture is increased by roughly 50% and the ring tunes are changed to $\nu_x = 20.185$ and $\nu_y = 6.385$. Such a lattice may prove useful during the initial commissioning stages.

4.3.2 Pre-Damping Ring

As described, the Positron Pre-Damping Ring (PPDR) is designed to damp the large emittance positron beam from the positron source to an emittance of roughly $\gamma\epsilon_{x,y} = 1 \times 10^{-4}$ m-rad. At this point, the positrons are injected into the positron main damping ring (PDR), described in Section 4.3.1 where they are damped to the desired final emittances. The pre-damping ring allows us to decouple the large aperture requirements for the incoming positron beams from the final emittance requirements of the linear collider.

The damping and emittance requirements on the PPDR are described in Section 4.2.3. The determination of the design parameters is discussed in Sections 4.2.6–4.2.9; these parameters are summarized in Table 4-8.

The pre-damping ring does not need to produce flat beams. Thus, to maximize the damping of the transverse phase space, the ring has $J_x \approx 1.4$ and operates on the coupling difference resonance. This increases the damping in both the horizontal and vertical planes. Furthermore, like the main damping ring, the ring damps multiple trains of bunches at once, the number of which is determined by the ring circumference. The initial design was only 114 m in circumference and stored only two trains. The present design is roughly 50% larger and stores three bunch trains. Although this increase in circumference will certainly increase the cost of the ring, the previous design was very tightly packed making the component design and maintenance substantially more difficult; experience with the SLC damping rings strongly suggests that the increase in circumference is cost-effective.

The magnets and vacuum system are being designed to provide sufficient aperture to accept a 2-GeV beam with an edge emittance of $\gamma\epsilon_{x,y} = 0.09$ m-rad and $|\delta p/p| \leq 1.5\%$ plus 2-mm clearance for misalignments and mis-steering. Given the nominal injected edge emittance of $\gamma\epsilon_{x,y} = 0.06$ m-rad, this provides a substantial margin for injection and internal mismatches.

Like the main damping rings, all of the quadrupoles and all of the sextupoles will have independent power supplies. This will facilitate beam-based alignment as well as matching of the lattice functions which is especially important in the pre-damping ring because of the limited aperture.

In the next sections, we will describe the ring layout and then details of the ring lattice: the arcs and the dispersion suppressors, the wiggler and injection and extraction straight sections, and the placement of the rf cavities. Issues

Energy	$1.8 \sim 2.2$ GeV; 1.98 GeV nominal
Circ.	171 m
Max. Current	1.2 A
Max. N_{bunch}	1.57×10^{10}
Trains	3 trains of 90 bunches
Train Separation	64 ns
Bunch Separation	1.4 ns
Max. Rep. Rate	180 Hz
ν_x, ν_y, ν_s	10.18, 8.18, 0.018
$\gamma\epsilon_x$	7.7×10^{-5} m-rad
$\gamma\epsilon_{x,y}$ (coupled)	4.5×10^{-5} m-rad
σ_ϵ	0.1%
σ_z	7.5 mm
$\xi_{x\,\mathrm{uncorr}}$, $\xi_{y\,\mathrm{uncorr}}$	-13.9, -10.0
τ_x, τ_y, τ_z	4.44 ms, 6.15 ms, 2.73 ms
U_{SR}	371 KV/turn
J_x	1.39
α_p	0.0051
V_{RF}	2.0 MV
f_{RF}	714 MHz
Lattice	30 FOBO Cells

Table 4-8. *Parameters for pre-damping ring (vers. 3.4)*

such as trajectory correction, dynamic aperture, and matching are described later in this section (Section 4.3), while collective effects are discussed in Section 4.4. In addition, the rf and vacuum systems are described in Sections 4.5 and 4.6 while the feedback systems and support and alignment systems are described in Sections 4.7 and 4.9. Finally, the magnet and diagnostics designs are describe in Sections 4.10 and 4.11.

Layout

The design of the pre-damping ring looks very similar to the SLC damping rings, except the lengths are scaled by a factor of five. The ring has a race-track form with dispersion-free straight sections for injection and extraction. The ring is roughly 60 meters by 40 meters and is illustrated schematically in Figure 4-16.

In the design, the injection and extraction regions are in the straight sections on opposite sides of the ring. To reduce the requirements on these components, the systems are designed to occupy most of these regions. To minimize rf transients during injection and extraction, a new bunch train will be injected one half turn after a train is extracted. Furthermore, the rf cavities are placed downstream of the injection kicker and upstream of the extraction kicker so that the injection/extraction process will not interrupt the beam current seen be the rf cavities.

Arcs

Each arc is constructed from 14 FOBO cells plus dispersion suppressors. The FOBO cells are similar to FODO cells except a bend with a defocusing gradient is used instead of the defocusing quadrupole. This lattice structure was chosen because it keeps the lattice functions well constrained and it is simple. It has significantly better emittance

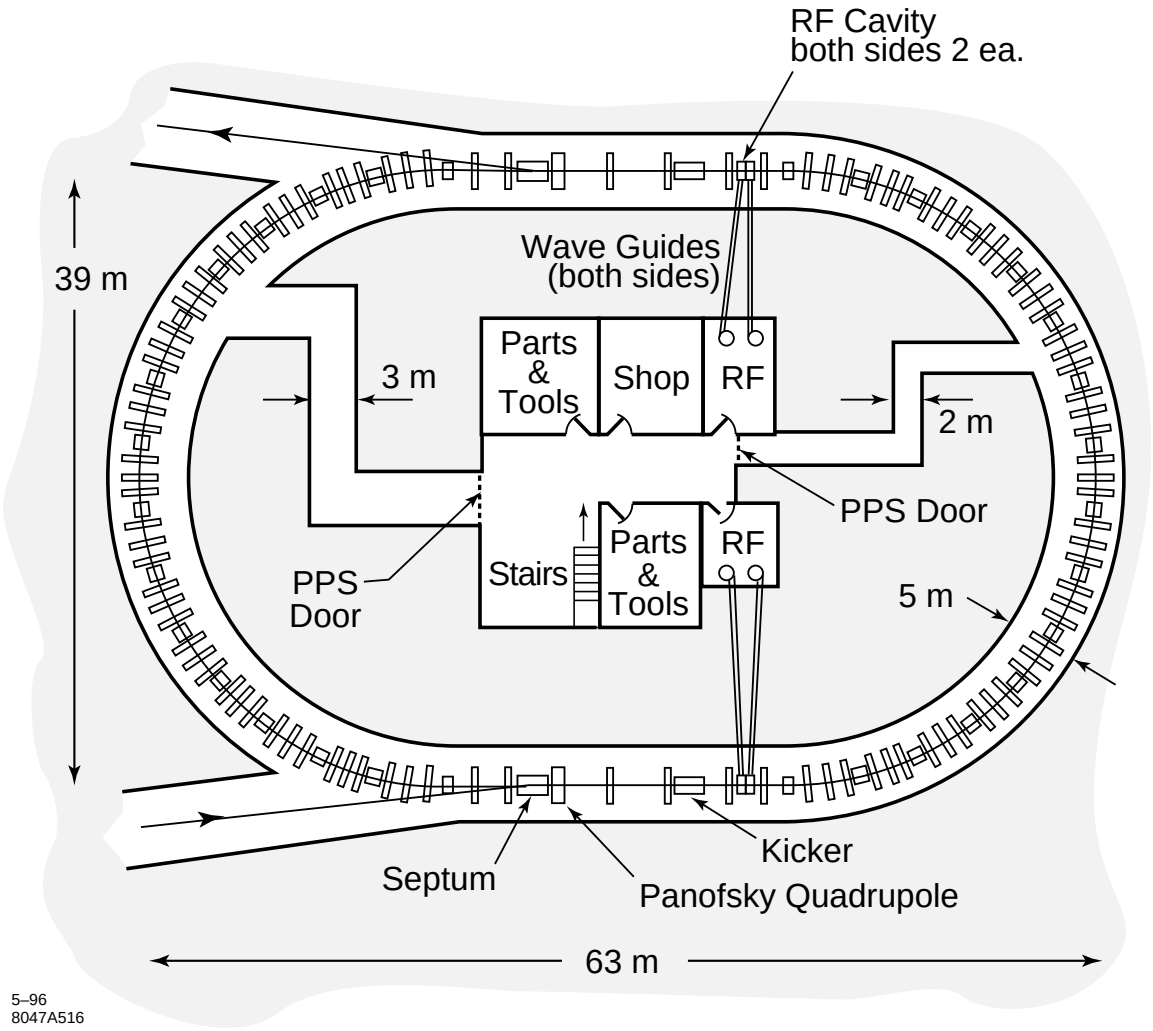

Figure 4-16. *Layout of pre-damping ring.*

performance than the normal FODO lattice and the single central bending magnet has smaller fringing field losses than if it were split as in a normal FODO cell.

Although the bending magnet has a defocusing gradient and could, in theory, completely replace the defocusing quadrupole, small defocusing quadrupoles are included at either end of the bending magnet. These provide additional vertical focusing to reduce the aperture and gradient requirements in the bend and they provide additional tuning control to optimize the lattice. Thus, each cell contains a single bending magnet, a single QF magnet, and two QD magnets. These magnets are described in Section 4.10. The cells are 4.1-m in length and the horizontal and vertical phase advances per cell are roughly 0.29 and 0.20. These tunes were chosen to balance the emittance contribution against the chromaticity generated by the cells while constraining the vertical beta function in the bending magnet. Finally, the lattice functions and magnet locations are plotted in Figure 4-17.

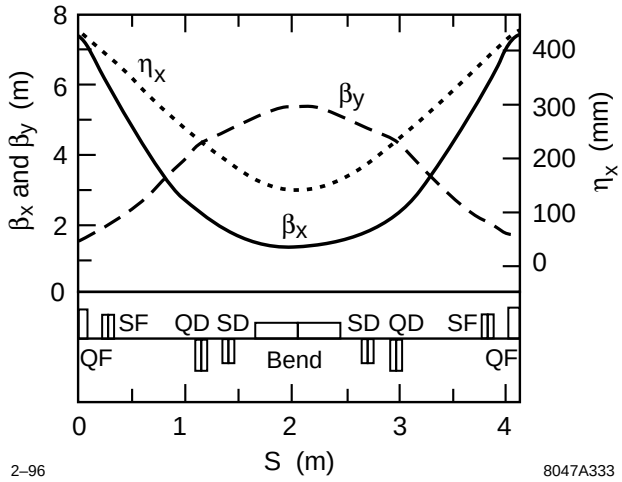

Figure 4-17. *β_x (solid), β_y (dashes), and η_x (dots) in the pre-damping ring FOBO cell.*

The dipole steering correction is performed using trim windings on the sextupoles. There is one horizontal corrector and one vertical dipole corrector in each cell. In addition, there are two BPMs per cell: one located adjacent to the bending magnet and one located next to the focusing quadrupole.

The chromatic correction is performed using two families of sextupoles: a set of defocusing sextupoles located between the bending magnet and the defocusing quadrupoles and a set of focusing sextupoles located between the defocusing and focusing quadrupoles. The symmetric placement of the sextupoles optimizes the dynamic aperture although it doubles the required number of sextupole magnets; this should be further investigated in the future.

The required vacuum aperture is determined from $X, Y = \sqrt{2\beta\epsilon_{x,y}} + \eta_{x,y}\delta p/p$. To provide sufficient aperture for an edge emittance of $\gamma\epsilon_{x,y} = 0.09$ m-rad and $|\delta p/p| = \pm 1.5\%$ plus 2-mm clearance around the beam for misalignments and mis-steering, the inner chamber size must be 5.8 by 1.8 cm at the focusing quadrupoles and 2.0 by 3.6 cm at the bending magnet. To minimize the impedance of the chamber, we will use a uniform elliptical cross section of an inner aperture of 6 cm by 3.6 cm; this will be discussed further in Section 4.6.2.

Finally, the dispersion is matched to zero at the end of the arcs for the two straight sections. The matching is performed using the two upstream quadrupoles and a bending magnet with an integrated dipole strength that is half that of the arc bending magnets. These matching bends have the same magnetic field as the main arc bends and half the effective length, but they have no field gradient to ease the field requirements and the fringing fields. As in the main damping ring, the horizontal and vertical dispersion matches will be tuned using the dispersion matching quadrupoles and trim windings on the sextupoles wired as skew quadrupoles.

Injection/Extraction

The injection and extraction regions are constructed from FODO cells in the dispersion-free straight sections. The two regions are located on opposite sides of the ring and utilize most of the respective straight sections to reduce the requirements on the kickers and the septa. Both systems are identical except for the number of kicker modules that are used; the extraction line needs fewer because of the smaller out-going beam. The lattice functions and component placement in the injection linac are illustrated in Figure 4-18.

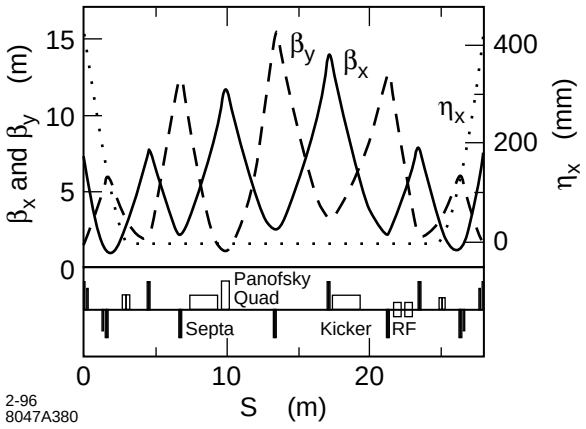

Figure 4-18. *β_x (solid), β_y (dashes), and η_x (dots) in the pre-damping ring injection region.*

The injection kickers are constructed in six segments with a total length of 2 m and provide an 8-mr horizontal deflection. The large deflection is needed because of the very large injected beam emittances. The extraction kicker is similar except it would be constructed from five of the kicker segments and would provide a 6.6-mr horizontal deflection. Both of these are described further in Section 4.10.3.

The septa are DC Lambertson septa that deflect the beam vertically. They are 2-m in length and have 5-kGauss fields providing a 150-mr deflection. The return blades are 2.3-cm thick and are located 3.3-cm from the stored and injected beam trajectories and 1.8-cm from the extracted beam trajectory; the extracted beams sizes are smaller and thus less space is required. In all cases, this leaves >1-cm clearance from the edge of the beam to the blade, assuming an injected edge emittance of 0.09 m-rad and an extracted beam emittance of 1×10^{-4} m-rad; the septa are described further in Section 4.10.2.

The focusing quadrupoles, adjacent to the septa, are constructed as dual Panofsky quadrupoles. This is necessary to make optimal use of the kickers. Both halves of the dual quad have the same strength and the same polarity. They are 50-cm in length and provide an integrated gradient of 28 kGauss. The horizontal aperture of each quadrupole is 6.2 cm. The center current sheet is 2-cm thick and, assuming an injected edge emittance of $\gamma\epsilon_{x,y} = 0.09$ m-rad, the blades are 8 mm from the stored and injected beams; these quadrupoles are described further in Section 4.10.2.

Finally, the adjacent defocusing quadrupoles may need to include an entrance or exit beam line; at the adjacent defocusing quadrupoles, the injection and extraction trajectories are roughly 30 cm from the stored beam trajectory.

After the beam has cleared the ring, it is deflected horizontally and then vertically to return to the plane of the damping ring. The optics of this section has not yet been developed but no significant problems are expected. Beyond this point the injection and extraction lines will be similar to those of the main damping rings.

Using the same technique as in the main damping rings, the effects of kicker jitter on the extracted beam will be reduced using an achromatic (double) kicker scheme. Here, a compensation kicker is located in the extraction line after the septum compensation bend. Six quadrupoles are used to match the compensation kicker so that it is separated from the extraction kicker by a $+I$ transform in the horizontal plane. The compensation kicker is powered from the same thyratrons as the extraction kicker and is expected to reduce the sensitivity to kicker jitter by at least a factor of four. This will ease the tolerance $\Delta\theta/\theta$ on the extraction kicker from 0.0016 to 0.0064. A similar achromatic kicker system will be tested at the ATF damping ring at KEK.

RF Cavities

The PPDR uses four 714-MHz rf cavities to provide the 2-MV rf field; the rf system is described in Section 4.5. To eliminate the transient beam loading when bunch trains are injected and extracted, one pair of rf cavities is placed in a 2-m drift section after the injection kicker and the other pair is located in a similar drift before the extraction kicker; these are illustrated in Figure 4-18. Although the cavity aperture is large compared to the vacuum chamber radius, additional masking will probably be needed to protect the cavities from beam loss at injection.

4.3.3 Injection Line

The injection lines transport the beams from the source linacs to the damping rings. The damping ring injection components from the septum compensation bend through the injection kicker, are considered part of the damping rings and are described in Sections 4.3.1 and 4.3.2. The injection lines have five primary functions:

- Provide diagnostics to monitor incoming the beam energy, energy spread, transverse position, and emittance.
- Provide transverse betatron matching for injection into the rings.
- Compress the incoming energy spread and match the longitudinal phase space to the damping rings.
- Rotate the longitudinal polarization of the electron beam into the vertical plane for injection into the electron damping ring.
- Include a beam dump just before injection into the rings.

Although the positron beam is not presently polarized, we are designing the positron injection line so that it could be easily upgraded to operate with polarized beams, *i.e.,* either polarized positrons or polarized electrons which would be needed for γ-γ or e^--e^- collisions. Thus, the geometrical constraints imposed by the spin rotation are applied to both the electron and positron injection lines and the two lines are very similar.

Layout

The layout of the electron injection line is plotted in Figure 4-19; the positron line is similar, although there is a longer rf section after the arc instead of the solenoid. Both injection lines are roughly 70 m in length. They include an arc of 60° which:

- Generates the R_{56} for the energy compressor.
- Provides for the energy diagnostics.
- Rotates the polarization vector by 270° in the x–z plane so that it is oriented in the x direction.

Following the arc, a 2.5-m S-band (2.856 GHz) rf (electrons) or 4-m L-band (1.428 GHz) rf (positrons) accelerator section is used to perform the energy compression. The L-band rf is needed in the positron line because the incoming positron beam emittance is very large and the aperture of the S-band structure is not sufficient; unfortunately, one needs twice the energy gain from the L-band structure as would be needed from an S-band structure.

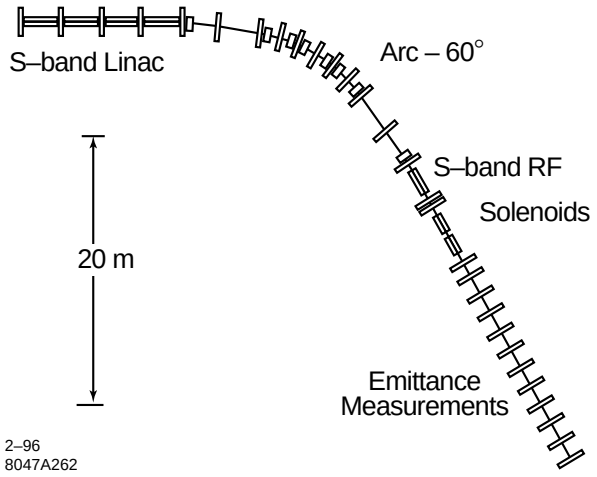

Figure 4-19. *Component layout of the electron injection line.*

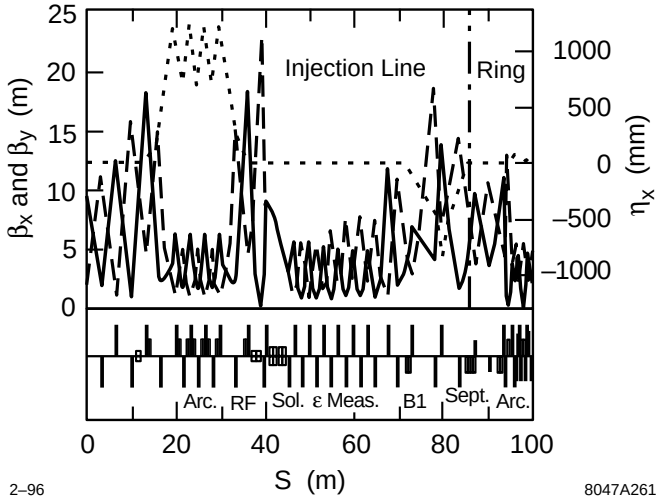

Figure 4-20. *β_x (solid), β_y (dashes), and η_x (dots) in the electron injection line with the solenoid on; the damping ring boundary is denoted by the vertical dashed line.*

Next, the electron side includes a solenoid to rotate the polarization from the horizontal plane to the vertical. This is followed by a series of FODO cells with five conventional wire scanners for emittance measurement; these wire scanners would be similar to those used throughout the SLC.

Finally, the beam is matched from the injection line into the ring. This section includes the septum compensation bend which generates a high dispersion that is ideal for a final energy and energy spread measurement. This portion of the line is described in Sections 4.3.1 and 4.3.2 and the component placement is illustrated in Figures 4-14 and 4-18. The bypass line, which includes a pulsed beam dump, intersects the injection line just before the septum compensation bend. A bending magnet is used to direct the beam to either the bypass line and beam dump or to the damping ring.

Optical Design

The electron injection line optical functions with the solenoids on are plotted in Figure 4-20; the positron line is similar. The lines are matched from the electron or positron source linacs into an arc that rotates the longitudinal spin polarization into the horizontal direction and acts as an energy diagnostic. The arc consists of three cells with a horizontal phase advance of 60° and a peak dispersion of 1.2 m.

This arc provides an $R_{56} = 0.8$ m for the energy compression and allows for a very accurate measurement of the beam energy by separating two BPMs by 180° and summing the horizontal measurements; the sum of the two measurements is independent of incoming betatron oscillations. The high dispersion also allows for accurate measurements of the electron and positron beam energy spread using wire scanners. For the electron beam, the dispersive beam size is roughly 1 cm while the betatron beam size is roughly 0.4 mm while in the positron system the expected energy spread extends between $\pm 2\%$ with a corresponding beam size of 2.4 cm at the high-dispersion points in the arc while the beam edge emittance of $\gamma\epsilon = 0.06$ m-rad corresponds to a size of 1 cm at the same location. Although this resolution is thought to be sufficient, if it is not, the dispersion can be increased in the design by increasing the length of the arc cells; this will be evaluated in the future.

In the electron line, the arc is followed by a 2.5-m S-band rf section which completes the energy compression and then two 1.5-m solenoids to complete the spin rotation. To prevent emittance dilution due to betatron coupling, the beta and alpha functions are set to be equal through the solenoid. The matching quadrupoles before and after the solenoid allow the betatron match to be maintained as the solenoid excitation is varied. The positron line differs in that it uses a 4-m L-band acceleration section and the solenoid is not needed.

Following the solenoids there is an emittance measurement section which consists of four FODO cells with five wire scanners interspersed. These wires will be used to measure the beam emittance, the betatron match, and the coupling mismatch from the solenoid; the matching quadrupoles can then be used to adjust the matching which when properly set will minimize the coupling mismatch as well as the betatron mismatch.

Finally, the beam line is matched past the septum compensation bend and into the ring; details of this are described in Sections 4.3.1 and 4.3.2. There is a dispersion maximum of 80 cm roughly halfway between the septum and the compensating bend where the final energy and energy spread will be measured just before injection into the rings.

Energy Compressors

The energy compressors reduce the incoming energy spread and the incoming energy jitter while increasing the bunch length. The compressor is required for the positron system because the pre-damping ring rf bucket height is only $\pm 1.5\%$ while the incoming beam has an energy deviation extending between $\pm 2\%$. The compressor also matches the beam to the rf bucket in the ring, reducing the amplitude of the longitudinal quadrupole oscillation at injection.

In the case of the electron beam, the compressor is not completely necessary since the rf bucket height is sufficient to accept the incoming beam. Regardless, the compressor will reduce the sensitivity to energy jitter and improve the longitudinal match at injection. In both cases, the compressors are designed to compress the energy spread and increase the bunch length by a factor of two. Parameters of the two compressors are given in Table 4-9 and the incoming and outgoing longitudinal phase spaces for the electrons and positrons are plotted in Figures 4-21 and 4-22, respectively.

Details of the energy compressor rf design can be found in Chapter 6. In both the S-band (electron) and L-band (positron) compressors, the structures will be Damped-Detuned Structures similar to those developed for the X-band main linacs. The L-band rf power will be provided by two 35-MW klystrons and a SLED rf pulse compressor. In the S-band case, the rf will be provided by a single 56-MW klystron which is similar to the SLAC 5045 klystrons. In both cases, the multibunch loading will be compensated using the ΔT (early injection) method. The positron compressor

	Electron	Positron
$(\Delta E/E)_{inj}$ (95%) (%)	±0.6	±1.8
$\sigma_{z\,inj}$ (mm)	1.5	3.7
R_{56} (m)	0.8	0.8
T_{566} (m)	2.0	2.0
f_{RF} (MHz)	2856	1428
V_{RF} (MV)	42	80
L_{RF} (m)	2.5	4
$(\Delta E/E)_{ext}(95\%)$ (%)	±0.4%	±1.0%
$\sigma_{z\,ext}$ (mm)	3.33	6.97

Table 4-9. *Parameters of electron and positron energy compressors.*

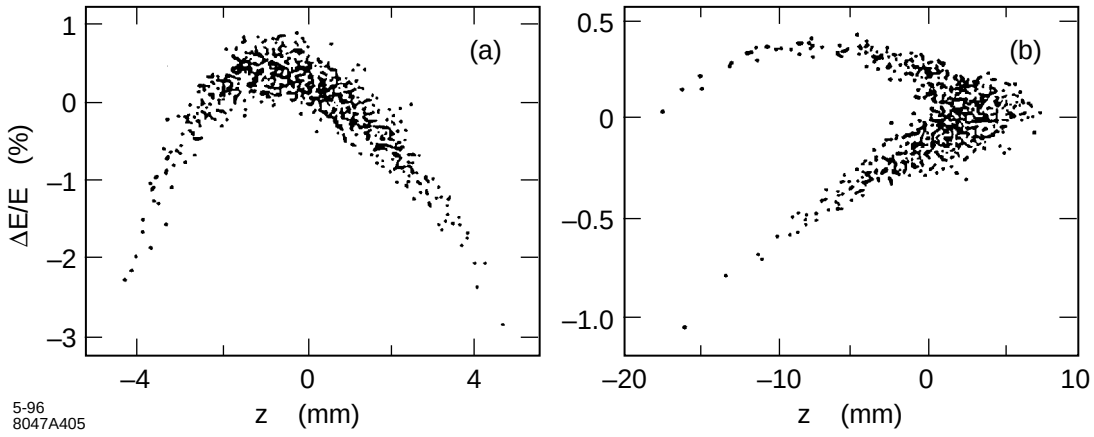

Figure 4-21. *Longitudinal phase space of electrons before (a) and after (b) energy compressor.*

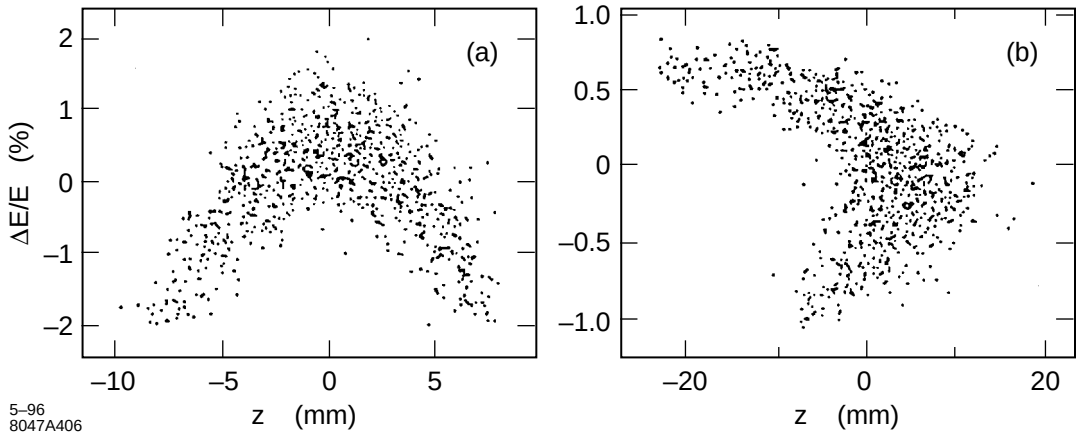

Figure 4-22. *Longitudinal phase space of positrons before (a) and after (b) energy compressor.*

has been specified to compensate for a maximum beam current of 2.75 A (2.4×10^{10} per bunch) which is roughly 85% greater than the charge needed at the IP to provide for beam loss through the injector system. The electron compressor has been designed to compensate for maximum beam current of 2.2 A (1.9×10^{10} per bunch) which is roughly 50% greater than the charge needed at the IP. In both cases, the beam loading should be compensated to an error less than a few 10^{-4} relative energy deviation; the tuning of the beam loading compensation will be done using either the energy spectrometer in the beam dumps or the dispersion in the arcs of the rings.

Polarization

The longitudinal polarization of the electron beam must be rotated into the vertical plane before injection into the main damping ring. This is performed using the 60° arc which rotates the polarization vector through 270° in the x–z plane at the nominal beam energy of 1.98 GeV. A solenoid is then used to rotate the polarization into a vertical orientation. The rotation in the solenoidal field is given by

$$\theta_s = \left[1 - \frac{g-2}{2}\right] \frac{B_z L_{sol}}{B\rho} \quad . \tag{4.21}$$

To perform the 90° rotation at 1.98 GeV requires an integrated field of 103.9 kGauss-m. We assumed two superconducting solenoids with lengths of 1.5 m and fields of 34.62 kGauss; these are similar to the superconducting solenoids used in the SLC damping ring injection and extraction lines.

4.3.4 Extraction Line

The main damping ring extraction lines only extend through the end of the achromatic kicker systems; the achromatic kicker system is discussed in Section 4.3.1. The extraction line optics is shown in Figure 4-23 and the component layout is illustrated in Figure 4-14 which is in Section 4.3.1.

The beam line downstream of the extraction line is part of the spin rotator and bunch compressor section and is described in Chapter 5. Regardless, it is worthwhile noting the requirements from the damping ring viewpoint.

- Energy and energy spread measurement: This will be done using the dispersion in the 20° arc which is part of the spin rotator system and is described in Chapter 5. In the same manner as in the injection line arc, BPMs located 180° apart in horizontal phase advance can provide a very accurate measure the the beam energy deviations.
- Bunch length measurement: It will be desirable to have a continuous parasitic measurement of the bunch length from the damping rings. This will be done by measuring the beam size in the bends of the bunch compressor. The calibration depends upon the compressor rf voltage and the dispersion in the bending magnet; this is discussed in Chapter 5.
- Transverse phase space measurement: The present design has a laser wire scanner located after the beta-matching quadrupoles at the end of the extraction line. This will provide a continuous parasitic diagnostic of the damping ring performance and can be used for quad-scan emittance measurements when necessary. In addition, there are four laser wire scanners in the prelinac at the end of the first bunch compressor. The emittance from the damping rings can be measured by turning off the bunch compressor spin rotation solenoids and the bunch compressor rf. This will be the main diagnostic for most tuning operations.
- Matching: The beta-matching will be performed using six quadrupoles at the end of the extraction line and the beginning of the bunch compressor system which is described in Chapter 5. The dispersion-matching will

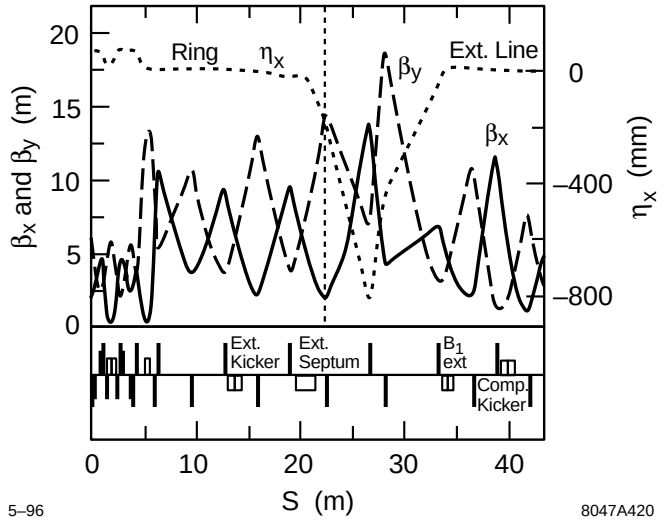

Figure 4-23. *β_x (solid), β_y (dashes), and η_x (dots) in the main damping ring extraction line; the damping ring boundary is denoted by the vertical dashed line.*

be performed using both trim quadrupoles and trim skew quadrupoles located in the extraction line and trim quadrupoles located in the 20° arc of the spin rotator system. Finally, the residual betatron coupling will be corrected with a skew correction system located between the spin rotators and the first bunch compressor; this is also described in Chapter 5.

- Pulsed dump line: A pulsed dump line will be located in the prelinac following the emittance diagnostics at the end of the first bunch compressor. This will allow full operation of the damping ring complex for commissioning and tuning.

4.3.5 PPDR-to-PDR Transfer Line

The design of the PPDR-to-PDR transfer line has not been completed yet. In concept it will combine the pre-damping ring extraction line, described in Section 4.3.2, with the main damping ring injection line, described in Section 4.3.1. In addition, the line should include a single wire scanner with a variable quadrupole to perform a quad-scan emittance measurement and a beam dump before the main damping ring. If the beams are polarized, the spin polarization will already be oriented vertically and no further manipulation is necessary.

4.3.6 Bypass Lines

The design of the damping ring bypass lines has not been completed yet. As illustrated in Figures 4-1 and 4-2, the primary component of the bypass lines will be the beam dumps. Since the bypass lines will branch off after the emittance diagnostics, these will allow tuning of the electron and positron sources while the damping rings are being maintained. These beam dumps will need to absorb the full beam power of roughly 130 kW.

Sextupoles ($X/Y/\Theta$) (μm/ μr)	100 / 50 / 1000
Quad. QFH ($X/Y/\Theta$) (μm/ μr)	100 / 100 / 600
Quad. QM2 ($X/Y/\Theta$) (μm/ μr)	100 / 100 / 600
Other Quad. ($X/Y/\Theta$) (μm/ μr)	100 / 100 / 1000
Bends ($X/Y/\Theta$) (μm/ μr)	200 / 200 / 1000
BPMs ($X/Y/\Theta$) (μm/ μr)	100 / 100 / 1000
All magnets have 0.1% rms strength errors.	

Table 4-10. *Rms errors for EDR and PDR orbit and emittance simulations.*

	Rms Θ_X (μrad)	Max Θ_X (μrad]	Rms Θ_Y (μrad)	Max Θ_Y (μrad)
Arcs	155	433	132	468
Straights	60	201	54	223

Table 4-11. *Corrector strengths from 100 simulations in the EDR and PDR with errors from Table 4-10.*

4.3.7 Trajectory Correction

The main damping rings and downstream systems all have very tight alignment and field tolerances to prevent dilution of the transverse emittances. In all cases, these tolerances will be attained using beam-based alignment techniques where the alignment accuracy depends on beam measurements and not mechanical systems; the techniques to be used in the damping rings are described in Section 4.9.

In the downstream systems, the alignment will be implemented using remote magnet movers. The tolerances are sufficiently loose in the damping rings that there is some question as to whether magnet movers are required; once the alignment is known, one could mechanically perform the differential moves to attain the desired alignment. This question will be determined in the future, for this design, we have assumed magnet movers.

In this section, we will describe the placements and required strengths of the trajectory correctors. These correctors must be able to provide sufficient steering to store beams before the beam-based alignment procedures are started. In addition, they must correct for residual alignment errors after beam-based alignment. In most cases, the corrector strengths required to simply store the beams are very weak compared to those required to steer the trajectory and minimize the BPM readings.

Main Damping Rings

In the main damping rings, each arc cell (Figure 4-10) contains two horizontal dipole correctors, a single vertical dipole corrector, and three BPMs. The horizontal correctors will be located at the S1 sextupole magnets (the sextupoles adjacent to the bending magnet). The vertical corrector will be located at either one of the S3 sextupoles (the sextupoles adjacent to the QD magnet). Both horizontal and vertical dipole correctors will consist of trim windings on the sextupole magnets and are discussed in Section 4.10.1.

Like the horizontal correctors, two BPMs will be located between the S1 sextupole magnets (the sextupoles adjacent to the bending magnet) and the QF quadrupole magnets. At this time, we have not determined how the BPMs are

mounted but, ideally, they would be constrained transversely at either the sextupole or the quadrupole magnet. The sextupoles are the preferred choice because they are separated by roughly 108° in horizontal phase advance while the QF magnets are separated by 144° and the orbit relative to the magnetic center of the sextupoles is more important than that of the quadrupoles. The third BPM would be located at the QD magnet; it is not strictly necessary for the trajectory correction or emittance control, but it provides redundancy if one of the other BPMs in the cell fails.

In both straight sections, BPMs will be located at every quadrupole, while horizontal dipole correctors will be located at the focusing quadrupoles and vertical dipole correctors will be located at the defocusing quadrupoles. Here, the dipole correctors will consist of trim windings on the quadrupoles.

Finally, additional horizontal and vertical dipole correction elements will be needed in the injection/extraction region to allow optimal control of the trajectory through this region. Small air core dipoles will be used for this function.

The orbit correction has been simulated using a standard set of errors listed in Table 4-10. All errors have Gaussian distributions truncated at ± 2.5 sigma. For the simulations, the arc BPMs and horizontal correctors were placed at the non-optimal QF magnets. After correction, the residual trajectory at the monitors was roughly 100-μm rms. The rms and maximum corrector strengths found from 100 simulations are listed in Table 4-11. The correctors are subdivided into arc correctors and straight section correctors. It is suggested to design the arc correctors for a maximum deflection of 0.50 mr (33 G-m field) and the straight section correctors for a maximum deflection of 0.25 mr (16 G-m field). These strengths will be more than sufficient to store beams after the preliminary conventional alignment where the expected errors are roughly four times those in Table 4-10. In addition, if during normal operation, the errors are significantly larger and many of the correctors are at maximum strength, the rings must be realigned.

Pre-Damping Ring

In the pre-damping ring, each arc cell (Figure 4-17) contains one horizontal dipole corrector, a single vertical dipole corrector, and two BPMs. The horizontal corrector will be located at one of the SF sextupole magnets (the sextupoles adjacent to the focusing quadrupole). The vertical corrector will be located at either one of the SD sextupoles (the sextupoles adjacent to the bending magnet). Both horizontal and vertical dipole correctors will consist of trim windings on the sextupole magnets and are discussed in Section 4.10.2.

Like the correctors, one BPM will be located between the SF sextupole magnets and the adjacent QF quadrupole magnets. The other BPM would be located between the bending magnet and one of the SD magnets. At this time, we have not determined how the BPMs are mounted but, ideally, they would be constrained transversely at either the sextupole or the quadrupole magnet.

In both straight sections, BPMs will be located at every quadrupole while horizontal dipole correctors will be located at the focusing quadrupoles and vertical dipole correctors will be located at the defocusing quadrupoles. Here, the dipole correctors will consist of trim windings on the quadrupoles.

The orbit correction has been simulated using a standard set of errors listed in Table 4-12. All errors have Gaussian distributions truncated at ± 2.5 sigma. For the simulations, the arc BPMs and horizontal correctors were placed at the non-optimal QF magnets while the defocusing correctors were placed at one of the QD magnets. After correction, the residual trajectory at the monitors was roughly 110-μm rms while the actual trajectory had an rms and maximum values of roughly 130 μm and 269 μm in the horizontal plane and 390 μm and 1014 μm in the vertical plane. These trajectory offsets are consistent with the 2-mm steering allowance provided in the aperture calculations.

The rms and maximum corrector strengths found from 100 simulations are listed in Table 4-13. It is planned to design the correctors for a maximum deflection of 1.0 mr (67 G-m field). These strengths will be more than sufficient to store beams after the preliminary conventional alignment where the expected errors are comparable to those in Table 4-12.

Sextupoles ($X/Y/\Theta$) (μm/ μr)	200 / 200 / 2000
Quadrupoles ($X/Y/\Theta$) (μm/ μr)	200 / 200 / 2000
Bends ($X/Y/\Theta$) (μm/ μr)	200 / 200 / 1200
BPMs ($X/Y/\Theta$) (μm/ μr)	200 / 200 / 2000
All magnets have 0.1% rms strength errors.	

Table 4-12. *Rms errors for PPDR orbit and matching simulations.*

Rms Θ_X (μrad)	Max Θ_X (μrad)	Rms Θ_Y (μrad)	Max Θ_Y (μrad)
166	532	347	1104

Table 4-13. *Corrector strengths from 100 simulations in the PPDR with errors from Table 4-12.*

Transfer Lines

No simulations have been performed at this time. The primary issues will be the aperture issues in the positron injection line, injection onto the closed orbit in both rings, trajectory control through the extraction septa. The aperture issues in the positron injection line will be resolved by including a $\pm$5-mm clearance for steering and including numerous BPMs and dipole correctors. The injection and extraction trajectories will be adjusted with additional steering correctors in the injection/extraction regions. The apertures of the septa have been chosen so that there should be plenty of room to optimize the trajectories.

4.3.8 Emittance Control and Matching

In addition to causing orbit deviations, alignment and field errors generate dispersion and betatron mismatches. In all of the damping rings, these increase the horizontal and vertical emittances but are only significant in the main damping rings where the equilibrium emittances are very small. In fact, in the main damping rings, the vertical emittance requirement determines alignment tolerances; other effects such as steering and dynamic aperture have looser tolerances.

In the pre-damping ring, which operates on the betatron coupling difference resonance, the tolerances for emittance control are relatively loose; other effects such as physical and dynamic aperture limitations are more important. Thus, the matching into- and in the pre-damping ring needs to be controlled. In addition, the pre-damping ring has a problem which is opposite that in the main damping rings, namely, the width of the coupling resonance is extremely small and, for stable operation, this will probably need to be increased with skew quadrupoles or vertical orbit bumps through the sextupoles.

In the transport lines, similar effects will increase the effective emittances injected into the rings, thereby increasing the time needed to damp to the desired emittances, and possibly leading to particle loss if the mismatched beam exceeds the aperture. We will first describe the issues for the main damping rings where the very small vertical equilibrium emittance determines the alignment tolerances; the tolerances needed to attain the vertical emittance are more severe than those due to the dynamic aperture limitations. Next, we will discuss the pre-damping ring and finally we will discuss the injection and extraction matching requirements.

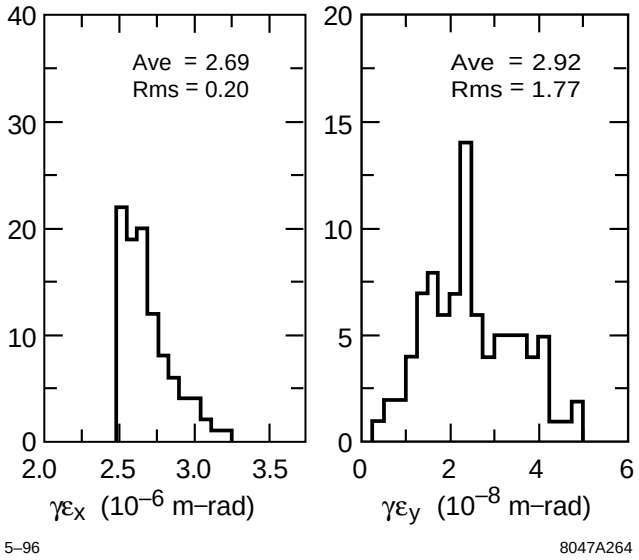

Figure 4-24. *Horizontal and vertical emittances from 100 simulations of errors and only using orbit correction; the average horizontal emittance is $\gamma\epsilon_x = 2.69 \times 10^{-6}$ m-rad and the average vertical emittance is $\gamma\epsilon_y = 2.92 \times 10^{-8}$.*

Although these effects will set tolerances, this section does not discuss how these tolerances will be attained and maintained stably. This will be discussed in Sections 4.9 and 4.8.

Main Damping Rings

In the NLC main damping rings, the primary sensitivity of the equilibrium emittances arises from dispersion mismatches; this is true in both the horizontal and vertical planes. Other effects such as betatron mismatches and betatron coupling are less important. In particular, the expected vertical emittance dilution from vertical dispersion due to random errors is roughly five times greater than the dilution due to coupling from the same errors.

The three elements that have the greatest contribution to the emittances are the horizontal and vertical misalignments of the arc sextupoles, rotational misalignments of the arc focusing quadrupoles, and rotational misalignments of the bending magnets. To reduce the emittance dilutions, it is most efficient to set lower tolerances on these sources and have more relaxed tolerances on the other elements.

We have performed 100 simulations using the errors listed in Table 4-10. As before, all errors have Gaussian distributions truncated at ± 2.5 sigma. Orbit correction was performed as discussed in the previous section. Without any other correction of the lattice, we found an average horizontal emittance of $\gamma\epsilon_x = 2.69 \times 10^{-6}$ m-rad and an average vertical emittance of $\gamma\epsilon_y = 2.92 \times 10^{-8}$ m-rad; for comparison, the design values for horizontal and vertical emittance are $\gamma\epsilon_x = 2.6 \times 10^{-6}$ m-rad and $\gamma\epsilon_y = 1.5 \times 10^{-8}$ m-rad. Histograms of the resulting emittance values are plotted in Figure 4-24.

In general, the dispersion generated by the alignment errors is easily corrected. The mismatch will oscillate much like an uncorrected close orbit and a few dispersion correctors can reduce the rms value significantly. The horizontal dispersion can be corrected using weak quadrupoles in regions of large horizontal dispersion and the vertical dispersion can be corrected using weak skew quadrupoles in regions of large horizontal dispersion.

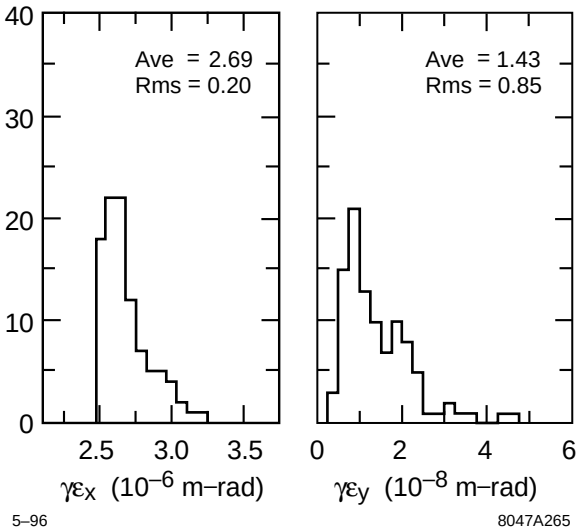

Figure 4-25. *Horizontal and vertical emittances from 100 simulations of errors where two weak skew quadrupoles were used to reduce the vertical dispersion; the average vertical emittance is* $\gamma\epsilon_y = 1.43 \times 10^{-8}$.

In Figure 4-25, we plot the residual emittance after using just two skew quadrupoles, located in the dispersion suppressor cells, to minimize the rms vertical dispersion. Notice that both the average of the vertical emittance and the width of the distribution are decreased. In this case, the average vertical emittance is $\gamma\epsilon_y = 1.43\times10^{-8}$ m-rad and 95% of the simulations have emittances below $\gamma\epsilon_y = 3 \times 10^{-8}$ m-rad; further correction would be possible with additional elements. This minimization can be performed either by directly measuring the dispersion or by optimizing the emittance of the extracted beam; in the simulation, we optimized the extracted beam emittance. Finally, as mentioned, a similar procedure can be used to correct the horizontal dispersion. We have not yet implemented such a solution but it will be straight-forward.

The current design for the main damping rings specifies individual power supplies for all the quadrupoles and sextupoles. Thus, there are numerous quadrupoles that can be used to correct betatron mismatches and horizontal dispersion mismatches. In addition, we are considering using magnet movers on most of the quadrupoles and sextupoles. If remote magnet movers are adopted then skew correctors to correct the vertical dispersion will exist all around the ring, *i.e.,* vertical motion of the sextupoles. If we do not choose to use the remote magnet movers, then eight sextupoles in each arc will have trim windings wired as skew quadrupoles.

As discussed previously, the alignment tolerances will be attained using beam-based alignment practices which are discussed in Section 4.9 while the tolerances required to maintain the required stability are discussed in Section 4.8.

Pre-Damping Ring

As stated, the issues are completely different in the pre-damping ring. Here, because the aperture is tight, the primary problem becomes maintaining the matched beta and dispersion functions. With the individual quadrupole power supplies it is straight-forward to both measure and correct any betatron mismatches that may exist. Similar arguments apply to correcting dispersion mismatches which are easily measured by storing the beam and varying the rf frequency.

Finally, because of the accurate alignment that is required to attain the desired dynamic aperture, the width of the betatron resonance is relatively small. This will make reliable operation on the coupling resonance difficult and so

skew quadrupoles will be used to increase the width of the resonance; this technique was also used on the SLC Positron Damping Ring.

Injection Line

The injection lines have relatively loose alignment and field tolerances. The primary issue is matching the beams to the damping rings. This is required to prevent emittance growth due to filamentation and possible beam loss if the mismatched beam exceeds the damping ring aperture.

Both injection lines have emittance diagnostics just upstream of the rings so that incoming mismatches can be corrected. The fine tuning of the beam match will be performed using gated synchrotron light cameras, located in the rings, to measure the beam size on different turns after injection. This technique has been used to successfully match the incoming phase space to the SLC damping rings [Minty 1995] and we expect to be able to match the incoming beam sizes to better than 10%.

Extraction Line

In the extraction lines from the main damping rings, the beam emittances are asymmetric and very small. Thus, betatron coupling and dispersive errors can lead to significant emittance growth. The betatron coupling will set tolerances on the allowable magnet roll and skew fields. This is particularly true for the extraction septa which tend to have nonlinear fields close to the septa blades. Similarly, the dispersive errors will set tolerances on the allowable orbit deviations, magnet alignment, and matching of the dispersion.

In the NLC damping rings, we are including multiple steering correctors to optimize in the injection and extraction trajectory through the septa. In addition, we are designing the septa with substantial clearance between the beam trajectory and the septa blades to minimize the nonlinearity seen by the beams.

The extraction lines will include six matching quadrupoles to match the beta functions into the spin rotators beam lines which follow; these are described in Chapter 5. In addition, residual betatron coupling from the damping rings or the extract lines will be corrected in the first bunch compressor skew correction section; this is also described in Chapter 5. In simulations, this correction section has had no difficulty removing large coupling from the extracted beams. We do not plan on installing any additional skew quadrupoles to control the betatron coupling in the extraction lines.

Trim quadrupole and skew quadrupoles will be located in the dispersive region of the extraction lines (Figure 4-23) to correct for residual dispersion leaking from the damping rings. In addition, correcting quadrupole elements will be placed in the 20° arc which is part of the spin rotator that follows the damping ring extraction lines.

Most tuning of the extracted beam will be performed using the emittance diagnostic station at the end of the first bunch compressor; this is described more fully in Chapter 5. To measure the extracted beams, the compressor rf and spin rotators will be turned off. In addition, a single laser wire will be located in the extraction line to monitor the ring performance. It will be possible to perform quad-scan emittance measurements on this wire for further tuning of the extracted beam.

Transfer Line

At this time, we have not yet designed the PPDR-PDR transfer line. It is expected that the beam line will be a combination of the injection and extraction lines just discussed and is not thought to present any significant problems.

Source	Error	Rms Magnitude
All Elements except Bends	$X,\ Y$ (μm)	100, 100
All Bends	$X,\ Y$ (μm)	200, 200
All Elements	Z [mm], Θ (mr)	1, 1
All Magnets	$\Delta B/B\ (10^{-3})$	1

Table 4-14. *Rms errors for main damping ring dynamic aperture simulations.*

The line will include a single conventional wire scanner to monitor the pre-damping ring performance. In addition, quad-scan emittance measurements could be made on this wire when desired.

4.3.9 Dynamic Aperture

The dynamic aperture is usually a limitation in low-emittance strong-focusing rings such as the NLC main damping rings. It is of particular concern in these cases, because the the rings must be designed to have minimal injected beam loss and the injected beam emittances are many orders of magnitude larger than the extracted emittances. The dynamic aperture is also a limitation for the pre-damping ring because of the very large injected beam emittances.

At this time, we have developed solutions for both the main damping rings and the pre-damping ring with very satisfactory performance. The tolerances in the main damping rings to attain a dynamic aperture that is in excess of $10\sigma_{x,y}$ of the injected beams are looser than the tolerances that are required to attain the desired extracted vertical emittance. We believe that these tolerances will be attained using beam-based alignment techniques and do not present a limitation.

In the pre-damping ring, the tolerances to attain a dynamic aperture in excess of the physical aperture are even looser. Here, the alignment tolerances could probably be attained using conventional alignment practices although the ability to use beam-based alignment will exist.

Finally, the multipole tolerances on the magnets in both rings are also straightforward. The tolerances on the main and pre-damping ring magnets are looser than the multipoles components that are being measured on the KEK ATF damping ring magnets and are comparable to those of the PEP-II LER ring magnets.

Main Damping Rings

The goals for the dynamic aperture are an aperture in excess of 10 sigma for an injected beam with the nominal injected emittance of 1×10^{-4} m-rad and a momentum aperture of $\pm 1\%$. This will allow the rings to operate during the commissioning phases where the injection beam properties will likely be poor and it will reduce the sensitivity to injection trajectory errors. Of course, this goal far exceeds the aperture requirements. The electron and positron injectors are being designed assuming a 10% loss of charge at injection into the main damping rings for which an aperture of 3 sigma of the injected beam size would more than suffice.

The dynamic aperture studies have been performed using MAD (Vers. 8.1) and TRACY; it should be noted that both of these codes use large ring approximations and the validity of this should be verified. The results, including energy errors of $|\delta p/p| \leq 1\%$, are illustrated in Figure 4-26. The outer curve shows the acceptance of the bare lattice while

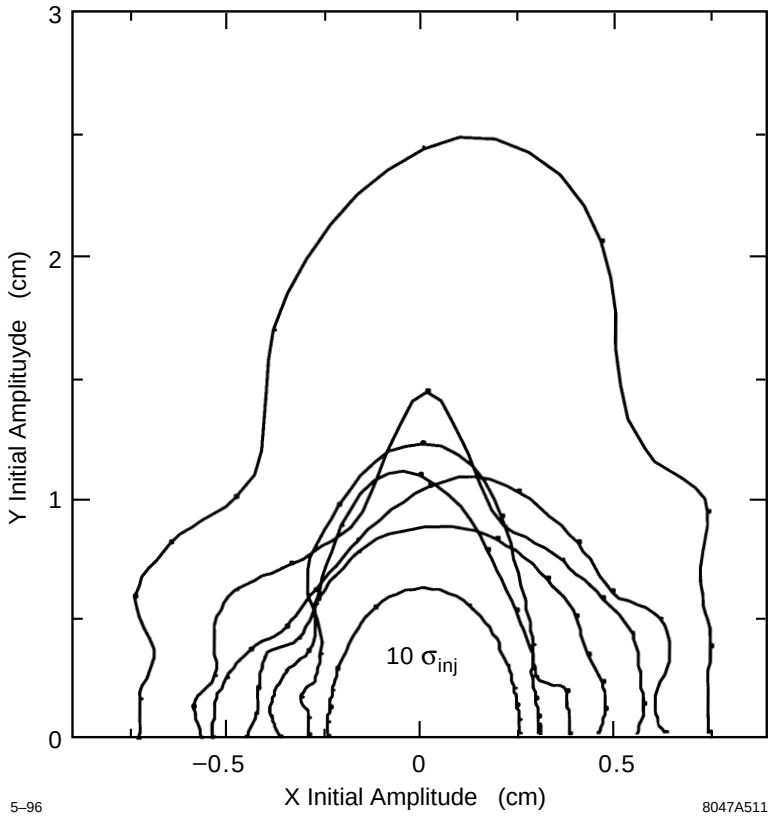

Figure 4-26. *Main damping ring dynamic aperture with multipole and alignment errors; the outer solid curve is the aperture of the bare lattice while the middle five curves are the aperture with different sets of errors and the inner solid curve is 10 sigma of the injected beam.*

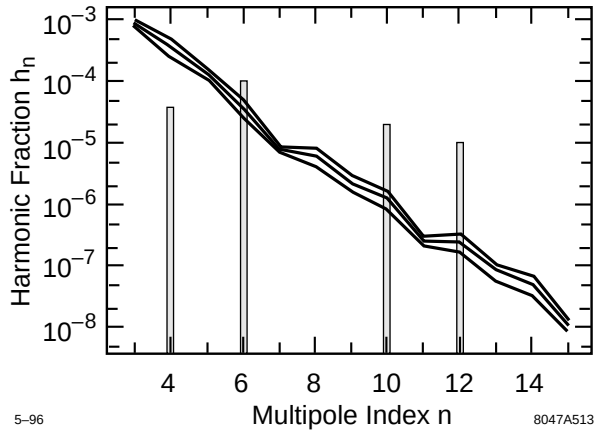

Figure 4-27. *Systematic (bars) and random (solid line) multipoles in the quadrupoles where the harmonic fraction is evaluated at 2/3 of the quadrupole bore.*

the inner curve is the goal of 10 times the injected beam size. One can see that the bare rings have an acceptance that is more than double the desired aperture.

The five middle curves in Figure 4-26 show the aperture when alignment and multipole errors are included, each curve corresponding to a different seed of random errors. In each case, the ring orbits were corrected with the dipole correctors and the tunes were corrected back to the nominal values using the arc quadrupoles.

The rms alignment errors that were used are listed in Table 4-14; these are looser than the tolerances required to attain the desired vertical emittance. In addition, all magnets were assumed to have strength errors of 10^{-3} and higher-order multipole errors.

The quadrupole magnet multipoles that were included are shown in Figure 4-27. Here, the bars represent the systematic multipoles while the solid line is the magnitude of the random multipoles. In both cases, the harmonic fraction shown is the multipole component relative to the quadrupole component at 2/3 of the the magnet bore; the bore varies from 15 mm to 30 mm for the different quadrupole families.

In order to evaluate the magnitude of the random multipoles in the quadrupole magnets, we assumed that the quadrupoles would be constructed in two pieces, as was done for both the ALS and the APS synchrotron light sources. The random contribution arising from fabrication errors then has two components: an uncorrelated pole-to-pole piece (significantly reduced relative to four-separate-pole construction), which we take to be 0.77 mils (20 μm) rms in the pole placement in the transverse plane; and the two-pole correlated contribution which can characterized in terms of a relative translation (in the transverse plane) and rotation of the two halves. The former we take to be 1.5 mils (40 μm) in each of the two dimensions, and the latter to be 1.1 mr, corresponding to a linear displacement of 8.9 mils (225 μm) at a 20 cm arm length.

These pole-to-pole errors contribute to all multipoles and yield a symmetric (but non-uniform) multipole orientation angle distribution, while half-magnet translation errors generate even index pole contributions (*i.e.*, 8, 12, ...), and rotation errors generate odd index poles (*i.e.*, 6, 10, ...). Neglecting fringe fields and assuming ideal pole shapes, the anomalous multipoles generated by the above pole misplacements are precisely determined (to first order) by two dimensional magnetostatics [Halbach 1969].

The estimated systematic components are based on preliminary designs and experience from similar magnet designs. The 8- and 24-pole contributions occur only in the magnets which must accommodate a wide vacuum ante-chamber and thus necessarily deviate from reflection symmetry around each pole. The detailed design alternatives that affect the systematic multipoles have been given minimal attention; thus these systematic multipoles should be viewed as representative rather than definitive.

Finally, similar random and systematic multipoles have been included in the combined function dipoles. The systematic multipoles tentatively adopted are slightly looser than those achieved in prototyping the KEK ATF combined function magnet. It will be possible to extend the analysis of random multipoles done above for quadrupoles once a sufficiently definite design of the combined function pole shape is achieved.

With the errors, the dynamic aperture still exceeds the goal aperture although it is significantly smaller than the bare aperture of the ring. Of course, the dynamic apertures are sensitive to the correction that has been performed. As a trivial example, we considered the seed that led to the worst aperture and corrected the tunes with the straight section quadrupoles rather than the arc quadrupoles. In this case, the aperture improves by roughly 60%; in other cases, correcting the tunes with the straight section quadrupoles rather than the arc quadrupoles has little effect. Finally, we have also studied the aperture for tune variations of 0.01 about the nominal tunes and saw no noticeable change.

Finally, we have not yet included the multipoles from the sextupole magnets or the effect of the nonlinearity due to the wigglers. Both of these are expected to have a small effect but still need to be added.

Source	Error	Rms Magnitude
All Elements	$X,\ Y$ (μm)	200, 200
All Elements	Z (mm), Θ (mr)	2, 2
All Magnets	$\Delta K/K\ (10^{-3})$	1

Table 4-15. *Rms errors for PPDR dynamic aperture simulations.*

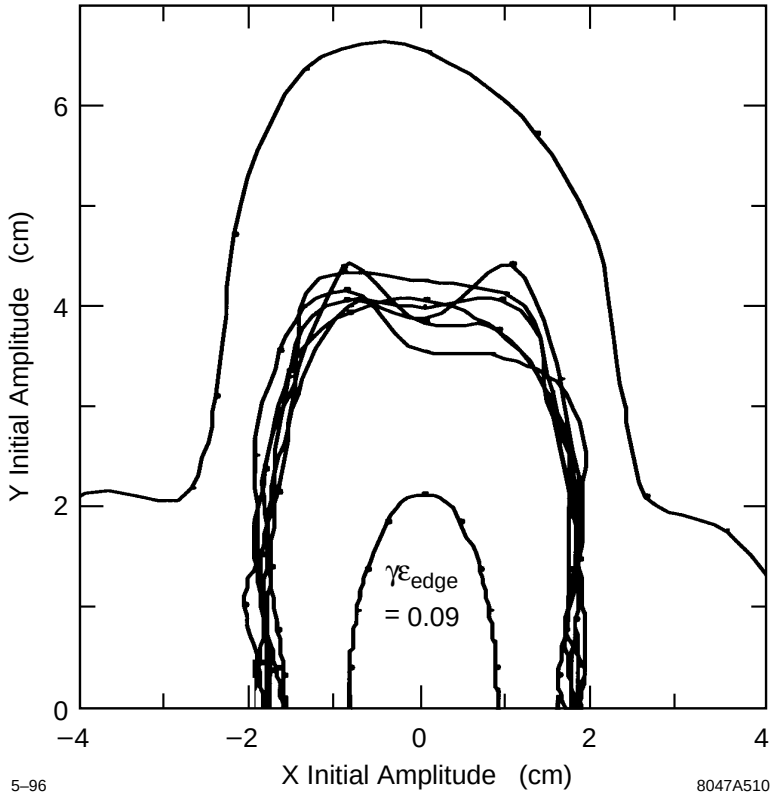

Figure 4-28. *Main damping ring dynamic aperture with multipole and alignment errors; the outer solid curve is the aperture of the bare lattice while the middle six curves are the aperture with different sets of errors and the inner solid curve is that required for an edge emittance of* $\gamma\epsilon_{x,y} = 0.09$ *m-rad.*

Pre-Damping Ring

In the pre-damping ring, the goal for the dynamic aperture is an acceptance in excess of the nominal injected edge emittance of 0.09 m-rad with a momentum aperture of $\pm 2\%$. This corresponds to a normalized acceptance of 0.09 m-rad where the acceptance is defined in terms of the particle action:

$$J_x = \frac{1}{2}\left(\gamma x^2 + 2\alpha x x' + \beta x'^2\right) \quad . \tag{4.22}$$

It should be noted that this is much larger than the aperture required. The positron source has been specified assuming 20% beam loss during injection into the pre-damping ring.

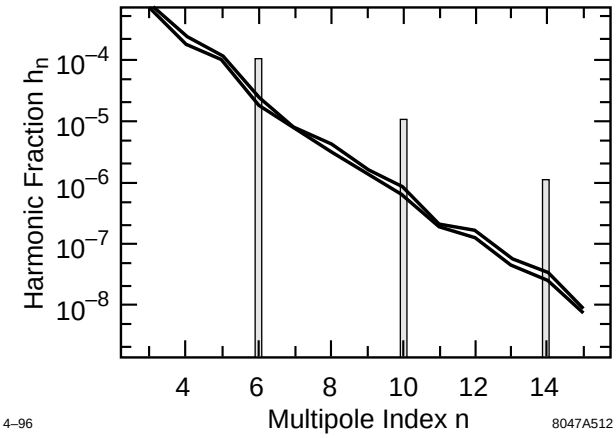

Figure 4-29. *Systematic (bars) and random (solid line) multipoles in the quadrupoles where the harmonic fraction is evaluated at 2/3 of the quadrupole bore.*

Again, the aperture studies have been performed using MAD (Vers. 8.1) and TRACY. We have studied the effect of alignment and magnet multipole errors. The results, including energy errors of $|\delta p/p| \leq 2\%$, are illustrated in Figure 4-28. The outer curve shows the acceptance of the bare lattice while the inner curve is the goal aperture of $\gamma J = 0.09$ m-rad. One can see that the bare rings have an acceptance that is more than three times the required aperture.

The six middle curves in Figure 4-28 show the aperture when alignment and multipole errors are included, each curve corresponding to a different seed of random errors. In each case, the ring orbits were corrected with the dipole correctors and the tunes were corrected back to the nominal values using the arc quadrupoles.

The rms alignment errors that were used are listed in Table 4-15; these are relatively loose tolerances and could be expected to be attained using conventional alignment practices. In addition, all magnets were assumed to have strength errors of 10^{-3} and higher-order multipole errors.

The quadrupole magnet multipoles that were included are shown in Figure 4-29. Again, the bars represent the systematic multipoles while the solid line is the magnitude of the random multipoles. In both cases, the harmonic fraction shown is the multipole component relative to the quadrupole component at 2/3 of the the magnet bore; the bore varies from 30 mm to 40 mm for the different quadrupole families.

As was done for the main rings, we assume that the quadrupoles would be constructed in two pieces with tolerances on 0.77 mils (20 μm) on the relative placement of the two poles on one piece and 1.5 mils (40 μm) on the placement of the two pieces. We also assumed random and systematic multipoles in the combined function dipoles that are based on those achieved in the prototype KEK ATF combined function magnet.

With these errors, we find that the aperture is almost double the required aperture. In the future, we will improve our estimates of the multipoles in the bending magnets and include multipoles in the sextupole magnets but we do not expect the aperture to change significantly.

4.3.10 Polarization

The polarization is assumed to be longitudinal at the exit of the electron source linac. It is rotated into the vertical plane in the injection line for injection into the electron main damping ring. The rotation is performed using the 60° arc followed by a solenoid. A similar arc is included in the positron injection line to allow the line to be easily upgraded for future polarized beams.

The polarization loss in the injection line due to the 1% energy spread in the beam is less than 1%. In contrast, if the injection line energy is changed, there will be large losses in polarization. This loss arises because the 60° arc no longer rotates the polarization by 270°. The fractional polarization loss is equal to:

$$\frac{\Delta P}{P} = (1 - \cos \Delta\Theta) \tag{4.23}$$

where $\Delta\Theta$ is the deviation from the 270° rotation: $\Delta\Theta = 270° \Delta E / 1.98\,\text{GeV}$. Thus, changing the ring energy by 100 MeV to 1.9 GeV or 2.1 GeV would result in a 2.7% loss in polarization through the injection line; the loss would increase to roughly 10% at 1.8 or 2.2 GeV.

At this time, we have not looked in detail at polarization issues in the damping rings. At the nominal operating energy of 1.98 GeV, the rings have a spin tune of 4.5; at this operating point, the depolarization is expected to be small. The operating energy range of roughly $\pm$ 220 MeV corresponds to shifts of ± 0.5 in spin tune. At these points, the spin tunes would be integral and we would expect full depolarization. Many other resonances exist that will limit the polarization within the ± 200-MeV operating range; these have not yet been studied although it would likely be possible to minimize their effect by modifying the ring tunes. We also have yet to study the effect of the beam emittance and the synchrotron radiation on the beam polarization. Both of these effects are expected to be negligible but have yet been considered.

Finally, after extraction from the damping rings, the polarization is rotated to the desired orientation in the bunch length compressors; these spin rotators are described in Chapter 5.

4.4 Collective Limitations

The NLC damping rings will operate with long trains of bunches at a high average beam current and thus coupled-bunch instabilities are an important limitation. In addition, to obtain the desired magnetic fields, the vacuum apertures are relatively small and the broad-band impedance sources can be large. Thus, both single and multibunch instabilities are potential limitations in the NLC damping rings.

Furthermore, because the performance requirements on the damping rings are tight, it is important to avoid instabilities of all sorts. This is also true of the so-called "benign" instabilities. For example, the "strong" longitudinal microwave instability, usually considered benign, sometimes exhibits a bursting mode that has been observed in a number of storage rings; such uncivilized behavior is not acceptable in a damping ring.

In this section, we review "collective" limitations for the main damping rings. We start by describing the impedance model for the ring. This is based upon MAFIA [Klatt 1986] calculations of the bellows, slots, masks, and BPMs, the resistive wall impedance, and the rf cavities; the rf cavities and the vacuum system are described in greater detail in Sections 4.5 and 4.6. Next, we discuss the single bunch instabilities, the synchronous phase variation along the bunch trains, and the coupled bunch instabilities. Finally, we address other effects including beam-gas scattering, intrabeam scattering, lifetime limitations, and ion trapping.

In addition to the usual series of instabilities, the damping rings may also be subject to some new effects that have been predicted theoretically but have not yet been seen experimentally. In particular, there are a photoelectron-positron instability, referred to as the "Ohmi effect," and a fast beam-ion instability that have been postulated. We address both of these issues although, at this time, the true implications are not clear.

In general, there are no known limitations in the main damping rings. The coupled-bunch instabilities require HOM damped rf cavities and a transverse coupled bunch feedback system but these technologies are being well developed for the new B-factories as well as for the KEK ATF damping ring. In addition, the broad-band impedance must be keep minimal to avoid the microwave instability but this should be possible with careful vacuum chamber design.

The two unknowns, the fast beam-ion instability and the electron-positron instability, will be verified in the near future. If they do present a limitation, there are a number of ways to ameliorate the effects; these are addressed in the respective sections.

Finally, this section deals primarily with the main damping ring. In most respects, the issues are less severe in the pre-damping ring since the bunch length is roughly twice as long, the vacuum aperture is much larger, and the beam emittances are much larger. The collective issues in the PPDR is are summarized in Section 4.4.11.

4.4.1 Main Damping Ring: Impedance Model

The ring impedance determines the beam stability and heating due to excitation of the higher-order modes (HOMs). The short damping ring bunches have a bunch spectrum that starts rolling off at 10 GHz, which is comparable to the 9-GHz cutoff frequency of the 1.25-cm-radius beam pipe. With such a broad bunch spectrum, even small irregularities of the beam pipe cross-section can give noticeable contribution to the beam impedance. Therefore, a careful design and analysis of the vacuum system and other impedance sources is required.

The total longitudinal impedance can be written as the sum of the narrow-band impedance (NB) and the broad-band impedance (BB):

$$Z_l^{tot} = Z_l^{NB} + Z_l^{BB} \quad . \tag{4.24}$$

The narrow-band impedance is primarily determined by the rf cavity HOMs and a few NB HOMs of the BPMs and bellows:

$$Z_l^{NB} = i\sum_m \frac{\omega_m}{2}\left(\frac{R}{Q}\right)_m \left[\frac{1}{\omega - \omega_m + i\omega_m/(2Q_m^L)} + \frac{1}{\omega + \omega_m + i\omega_m/(2Q_m^L)}\right] \quad . \tag{4.25}$$

The broad-band impedance is determined by the high frequency modes of the cavities and small discontinuities of the beam pipe such as the slot of the ante-chamber, bellows, BPMs, rf contacts, shallow tapers, etc. We can estimate the impedance by scaling from the inductance of the PEP-II. Scaling proportional to the machine circumference $2\pi R$ gives $L = 12$ nH. However, this scaling implies that the total number of inductive components in the ring scales as machine radius and that the inductive character of a component is not changed, *i.e.*, the dimensions of the elements scales in proportion to the rms beam size. A more accurate estimate can be obtained by modeling the vacuum components with the code MAFIA [Klatt 1986] as will be described below.

The broad-band impedance can be expressed:

$$Z_l^{BB} = -i\frac{Z_0}{(1 - i\omega a/c)^{3/2}}\frac{\omega L}{4\pi c} + (1-i)\,1.05\sqrt{\frac{\omega R}{c}} + (1+i)\frac{R_{cav}}{\sqrt{\omega}}\theta(\omega - \omega_c) \quad [\Omega] \quad . \tag{4.26}$$

The impedance of the inductive components also have a small resistive part in addition to the inductance. This is included in the first term in Eq. 4.26; the pure inductive impedance is modified to roll off at high frequencies as

Model	freq (MHz)	R_s [MΩ]	R/Q [Ω]	E_p (kV/m)	H_p (A/m)	k_l V/pC	$k_\perp$ V/pC/m
1	728.06	3.99	114.14	74.1	66.46	1.21	10.1
2	726.88	4.89	137.01	88.7	61.99	2.99	75.6
3	717.33	4.54	132.21	71.2	68.73	2.78	72.0

Table 4-16. *RF cavity models considered for MDR with $\sigma_z = 3.3$ mm.*

$1/\sqrt{\omega}$ which corresponds to the behavior of a cavity impedance at high frequencies. Such a model well describes the dependence of the loss factor on the bunch length. The parameter a defines the roll-off frequency and can be obtained from the loss factor of a bunch with the nominal rms length $\sigma_z = 4$ mm.

RF Cavities

The main contribution to the narrow-band impedance comes from the two rf cavities. As a first estimate, we modeled the cavities after the PEP-II rf cavity, scaled to the desired 714-MHz frequency. Since it is desirable to increase the beam pipe radius b at the cavity location to minimize the transverse kick factor, we considered three models with different beam pipe radii b and nose cone radii r:

1) b=3.1 cm, r=0.66 cm

2) b=1.4 cm, r=0.66 cm

3) b=1.4 cm, r=1.86 cm.

Table 4-16 gives frequency, shunt impedance R_s, R/Q, and the maximum E and H fields at the surface of the cavity, E_p and H_p, for the fundamental mode.

Cavity model 1, with 3.1-cm beam-pipe radius, has a total loss factor of $k_l = 1.21$ V/pC for an rms bunch length $\sigma_z = 3.3$ mm; this is shorter than the expected damping ring bunch length of $\sigma_z = 4.0$ mm. The maximum longitudinal impedance is $\Re Z_l = 0.21$ kΩ at 1 GHz while the maximum transverse impedance is $\Re Z_\perp = 170$ kΩ$/m^2$ at 2 GHz. The total loss factor of cavity model 2, with the 1.4-cm beam pipe, is $k_l = 3.0$ V/pC for the same 3.3-mm bunch length. The transverse kick factor is increased from $k_\perp = 10.2$ V/pC/m for cavity model 1 to $k_\perp = 75.6$ V/pC/m for cavity model 2 without a substantial gain in the shunt impedance of the fundamental mode.

The larger radius $r_c = 3.1$ cm of the beam pipe at the cavity location reduces the impedances which is preferable. The two rf cavities could be mounted on the same large radius beam pipe, which may be tapered to the regular 1.25-cm beam pipe at both ends. Separation of the cavities and the distance from a cavity to the nearest taper has to be optimized to avoid reduction of the Q factor of the fundamental mode and cross-talk between the cavities. The longitudinal loss and transverse kick factors for a model with a shallow 15-cm-long taper on both sides gives $k_l = 1.725\, V/pC$ and $k_\perp = 39.43$ V/pC/m; these numbers may be reduced by using longer tapers.

Such a design, however, leaves a large number of HOMs with frequencies up to the 9-GHz cutoff frequency trapped between the tapers. They can be damped by using absorbers placed on the tapers, adding wave guide dampers loaded with ferrite, or by using wave guides with ridges matched to coaxial cables. Similar designs have been used at KEK B-factory and DAFNE Φ-factory. The first method may be difficult to use because the absorber efficiency deteriorates at high frequencies and because the absorbers themselves would be sources of the resistive-wall impedance, outgassing, and dust.

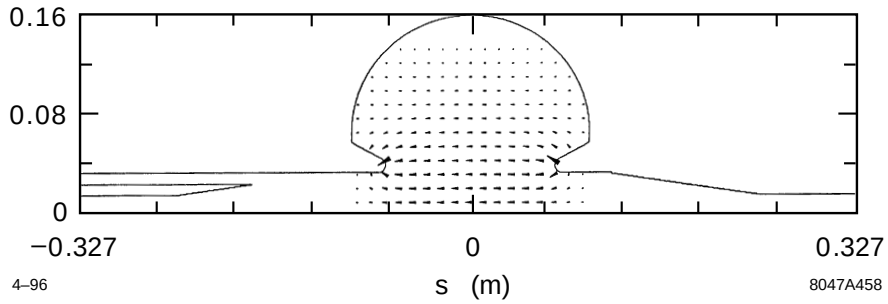

Figure 4-30. *Rf cavity model showing coax damping waveguide in the taper but not showing the damping waveguides on the cavity.*

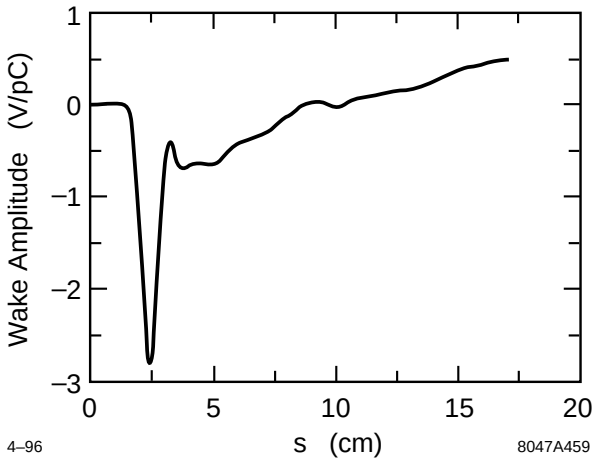

Figure 4-31. *Longitudinal wake for the rf cavity.*

A conceptual design using the wave-guide dampers is shown in Figure 4-30. A cylindrical coaxial wave guide, having a zero cutoff frequency, is connected to a taper. The outer radius of the wave guide is 3.1 cm and the inner radius of the wave guide was chosen to optimize the damping while minimizing the transverse kick to the beam. The wave guide is terminated with absorbers. The effect of the dampers on the Q-factor of the fundamental mode may be reduced by placing a choke on the wave guide.

Preliminary studies using MAFIA demonstrate that the fundamental mode is not affected by the wave guide damper as shown in Figure 4-30. The longitudinal wakeield for this design is shown in Figure 4-31; it is thought that the short-range wake can be further minimized with optimization of the parameters. At this time, we are performing 2- and 3-D MAFIA studies of the cavity to optimize the placement of the waveguide on the taper and those on the cavity body.

The high frequency contribution of the rf cavities to the broad-band impedance, Eq. 4.26, can be estimated comparing the loss factors of the modes with frequencies $\omega < \omega_c$ with the total loss factor of a cavity. The difference, Δk_l,

$$\Delta k_l = \frac{2R_{cav}}{Z_0}\sqrt{\frac{\omega_c}{c\sigma_z}}[\Gamma(1/4) - 4\sqrt{\frac{\omega_c\sigma_z}{c}}] \tag{4.27}$$

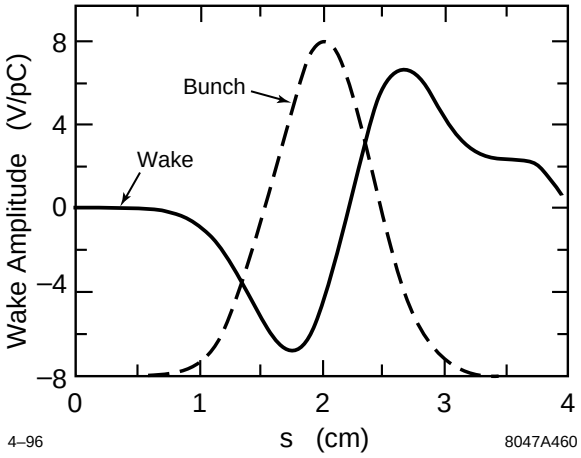

Figure 4-32. *Longitudinal wake of the slot termination.*

defines the coefficient which appears in Eq. 4.26

$$R_{cav} = \frac{Z_0 \Delta k_l}{2\Gamma(1/4)} \sqrt{c\sigma_z} \tag{4.28}$$

for $f_c = 5.34$ GHz. The sum of the NB contribution from the modes $f < f_c$ and the BB tail from $f > f_c$ has a weak dependence on the choice of f_c.

Resistive Wall

The resistive-wall impedance for a round 223-m Al beam pipe is

$$Z_l = (1-i)\, 1.05\sqrt{n}\,\Omega \tag{4.29}$$

$$Z_\perp = (1-i)\frac{0.48}{\sqrt{n}}\frac{M\Omega}{m} \tag{4.30}$$

where n is the harmonic number, $n_{max} = R/\sigma_z = 9000$ for $\sigma_z = 4.0$-mm bunch. The conductivity $\sigma_c = 3.8 \times 10^7$ $\Omega^{-1}m^{-1}$ and the beam pipe radius $b = 1.25$ cm were taken in this estimate. Note, that the skin depth is $\delta = 69.5/\sqrt{n}\,\mu$m.

The loss factor of the resistive wall is

$$k_l = \frac{\Re Z_l}{\sqrt{n}} \frac{2\Gamma(3/4)}{Z_0 \sigma_z} \sqrt{\frac{R}{\sigma_z}} \tag{4.31}$$

and, in this case, is equal to $k_l = 1.4$ V/pC. It should be noted that this estimate does not include the smaller vacuum aperture in the wiggler region where the full gap is only 16 mm. This is partially offset by the larger chamber in the injection/extraction region, and the average loss factor is not changed significantly.

Ante-Chamber Slots and Bellows

To provide adequate pumping with the minimum impedance and to reduce heating and adverse effects of the secondary photon and electron emission, the beam chamber is connected with the ante-chamber by a narrow slot 5-mm wide and

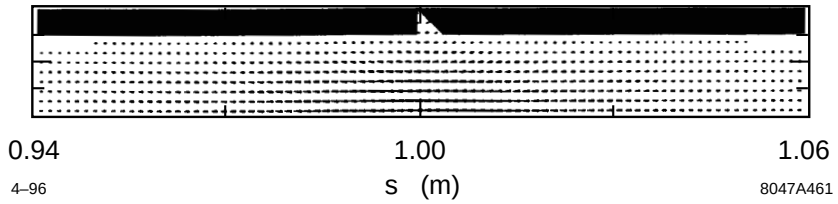

Figure 4-33. *MAFIA model of the bellows rf contact showing the trapped mode.*

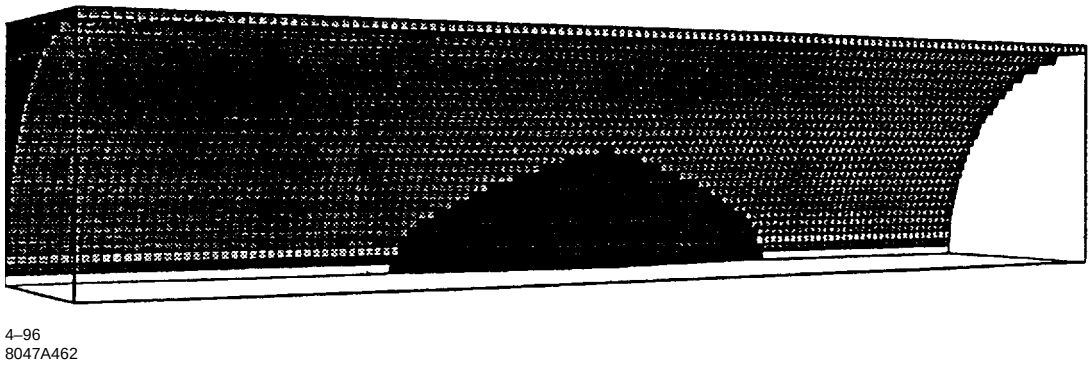

Figure 4-34. *MAFIA model for the bellows mask.*

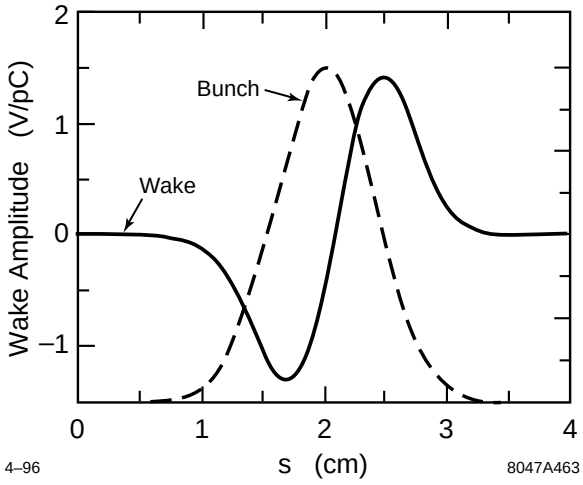

Figure 4-35. *Longitudinal wake for the bellows mask.*

20-mm deep. The slot is terminated with a 25° taper at the masks for the bellows. The impedance of the slot is inductive, see Figure 4-32. The inductance is 0.001 nH for the $\sigma_z = 4$-mm bunch length. The total inductance of 50 slots per ring is 0.05 nH, a very small contribution to the impedance budget.

The impedance of the shielded bellows is given by slots between shield fingers, and by a small cavity of 4-mm length near the ends of the fingers. The contribution of the slots can be estimated analytically and is negligibly small. The 2D MAFIA simulations of the small cavity showed that there is a trapped mode, see Figure 4-33, with frequency 9.099 GHz, which is below the beam pipe cutoff frequency of 9.186 GHz. The mode is localized in the region with length longer than length of the cavity. The trapped mode has a high $Q_0 = 15000$ and $R/Q = 0.23\,\Omega$. The power loss by 360 bunches with 1.5×10^{10} particles per bunch is 6.7 W but, only 25%, *i.e.*, 1.7 W, is deposited within the cavity region. This estimate is conservative because the beam pipe is interrupted by the chamber slot within the localization length of the trapped mode reducing the loaded Q factor of the mode.

Masks

A mask, that is 25-mm long and 2-mm thick, is located at the downstream end of the chamber slot to shield the bellows from the synchrotron radiation. The wakefield of the mask, modeled as shown in Figure 4-34, is depicted in Figure 4-35. The wakefield is mostly inductive but with a substantial resistive component of roughly 5×10^{-3} V/pC. The inductance of a mask is 0.0048 nH which agrees roughly with analytic estimates. The total inductance of the 50 masks and slots is 0.24 nH; the inductance will increase to 1.71 nH if the mask thickness is increased from 2 mm to 4 mm.

BPMs

The design of the BPMs in a high current ring is difficult because of the need to avoid trapped modes that can lead to excessive heating. The BPMs in the NLC damping ring consist of four buttons placed symmetrically around the beam pipe. In the initial design, the buttons have diameters of 8 mm and a ceramic ring of 2 mm thickness for vacuum seal is located at a distance of 9-mm away from the button. Calculations with 3D MAFIA were used to determine the impedance and signal sensitivity of the BPM. The MAFIA model of the BPM is outlined in Figure 4-36.

The total loss parameter of a four-button BPM is found to be $k_l = 2.03 \times 10^{-2}$ V/pC. The longitudinal wakefield of a BPM has a long tail of oscillations at large distances related to several trapped modes. The impedance spectrum is shown in Figure 4-37. Two prominent peaks in the relevant frequency range appear. The field pattern of the resonant mode of high Q at 9.1 GHz corresponds to a mode which is localized mostly in the beam pipe and extends to long distances around a BPM, (Figure 4-38(a)). For 150 BPMs, the total impedance of this mode is 2.1 kΩ, which is small compared with the stability limit of 6.5 kΩ which is calculated from Eq. 4.41 assuming that its frequency is resonant with the revolution frequency (f_b); this is the worst case. The actual frequency of the mode in units of the revolution frequency of 714 MHz, $f_r/f_b = 12.7$, is far from an integer value. Hence, the coupled-bunch effects of this mode will be small. Additionally, due to large spatial extent, the heating, produced by the mode at the BPM button, is small. Another resonance at 12.0 GHz is the TE_{11} is localized inside of a button, see Figure 4-38c. The total impedance for all the BPMs for this mode is 2.4 kΩ, which is small compared with the stability limit of 7.5 kΩ. The Q value of this resonance is about 50, and, hence, the heating effect arising from coupled bunches is negligible. Furthermore, there is a small peak at around 9.8 GHz between these two resonances. It is identified as the ceramic mode (Figure 4-38b). Since the ceramic is situated far away from the button, this mode is not strongly excited by the beam.

Thus, in the present design, there are a number of narrow-band impedances which appear to be below the coupled bunch stability limits. Detailed heating effects in the BPM need to be addressed further. Finally, the signal at the coax-

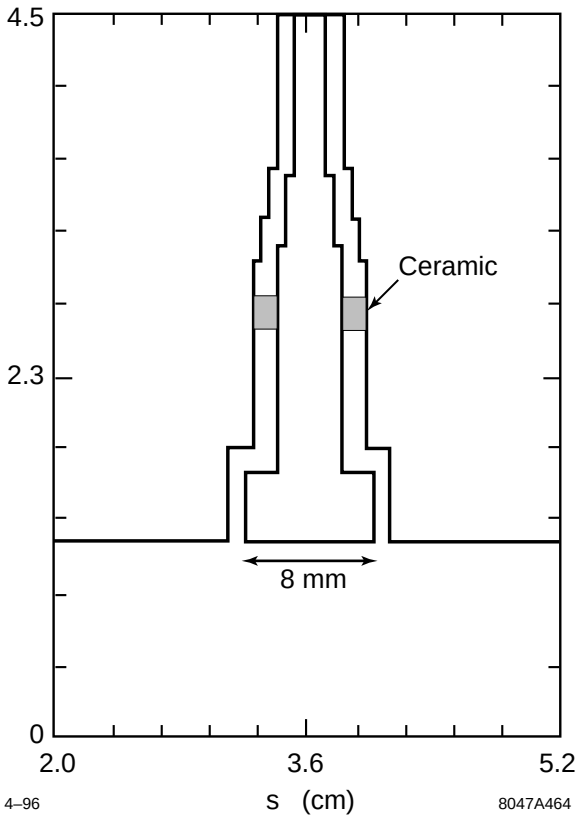

Figure 4-36. *2D projection of 3D MAFIA model for the BPMs.*

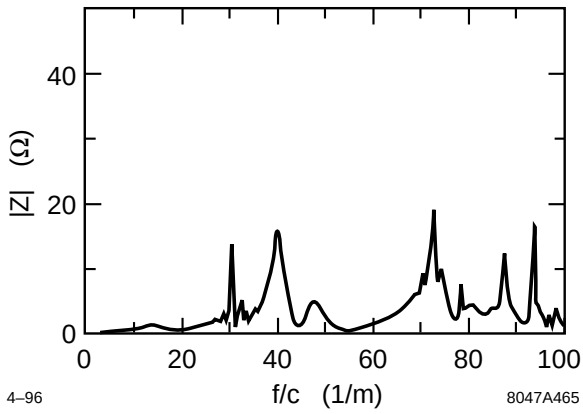

Figure 4-37. *Longitudinal impedance of a four button BPM.*

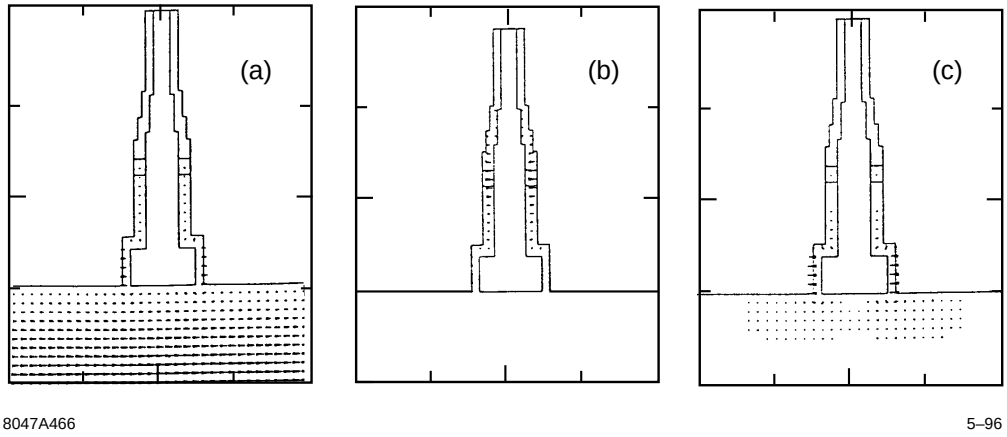

Figure 4-38. *Trapped modes in the BPMs.*

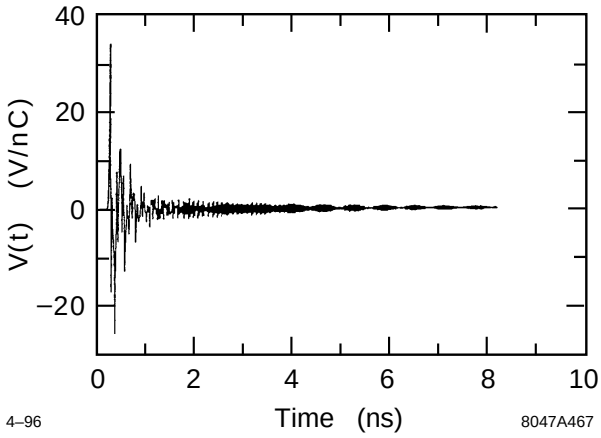

Figure 4-39. *BPM response to a passing bunch.*

ial cable as a function of time is shown in Figure 4-39 and the transfer impedance for the signal is shown in Figure 4-40. Further investigation is needed to determine whether the output signal satisfies the resolution requirements.

Summary

The contributions to longitudinal loss factor are listed in Table 4-17. The main contribution comes from two rf cavities, BPMs, and resistive walls. The other components of the ring are mostly inductive but, for short bunches, still have noticeable loss factors. The main source of the inductance is the synchrotron radiation masks, 50 of them give $L = 0.24$ nH. Some components, such as feedback, injection and extraction kickers, diagnostics, dampers, etc. are not yet included. We expect that they will not substantially change the total (high frequency) impedance.

The transverse impedance is dominated by the HOMs of the cavities and the resistive wall.

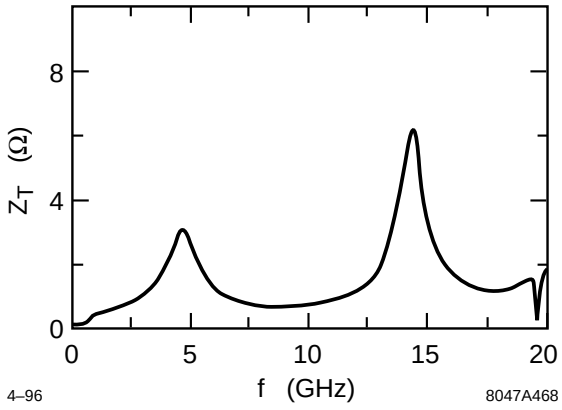

Figure 4-40. *Transfer impedance for the BPMs.*

	number	k_l V/pC
RF cavities	2	3.45
Res. Wall		1.44
Ante-chamber		0.0225
Bellows	50	0.365
4-button BPMs	150	3.04
Masks	50	0.25
Total:		8.5

Table 4-17. *Loss factor summary for the main damping rings.*

The total HOM power can be estimated from the total loss factor k_l as

$$P = I_{beam}^2 \frac{Z_0 k_l s_b}{4\pi} \tag{4.32}$$

which gives a rough estimate that does not take into account the real beam spectrum and an enhancement for the modes at frequencies equal to multiples of the bunch spacing frequency.

This yield $P = 15.4$ kW for $k_l = 8.5$ V/pC, maximum beam current $I_{beam} = 1.2$ A, and the $s_B/c = 1.4$-ns bunch spacing; the HOM power propagating in the beam pipe is smaller due to the narrow-band modes trapped in the rf cavities and BPMs. This is not expected to present a limitation but needs further investigation.

4.4.2 Single-Bunch Potential Well Distortion and Longitudinal Microwave Instability

The two important questions concerning the single bunch longitudinal phase space are (a) What is the average bunch shape and energy spread in the ring? and (b) What is the threshold current to the microwave instability? The answer to the first question is needed in order to know the longitudinal phase space properties of the bunch in subsequent parts of the collider. As for the second question, it is known that the microwave instability is accompanied by an increase in beam energy spread (which increases the longitudinal emittance) and, more importantly, that it can also be accompanied by unpredictable transient beam behavior (*e.g.*, the "saw-tooth" variation in bunch length that has been

observed in the SLC damping rings [Krejcik 1993]), a phenomenon that can greatly degrade the performance of the linear collider as a whole.

The microwave instability is also known to come in at least two forms: One, which we call the "strong" type of instability, has a high growth rate that depends only weakly on the synchrotron radiation damping rate, a threshold that can be roughly approximated by the Boussard criterion [Boussard 1975], and that can be thought of as generated by the coupling of two synchrotron modes with different azimuthal mode numbers. The other, a type that has only recently been identified [Oide 1994, Chao 1995, Bane 1995a], we call the "weak" type of instability; it has a growth rate that is sensitive to the radiation damping time, has a threshold that has no connection to the Boussard criterion, and can be described as the coupling of two modes with the same azimuthal but different radial mode numbers. The weak type of instability is found in storage rings with a predominantly resistive impedance.

In this section, we find that for the NLC damping rings at our highest design current ($N = 1.57 \times 10^{10}$) we may be running near the threshold of the weak instability but we are significantly below that of the strong instability. However, the weak instability is not a serious problem like the strong instability.

Consider, the SLC damping rings. In 1994 a completely redesigned vacuum chamber was installed. Before this time a strong type of instability was observed, with the current—due to the microwave instability—limited to the threshold value [Krejcik 1993]; since the upgrade only a weak type of instability has been seen, and the SLC runs routinely a factor of 3 above the threshold current [Bane 1995b]. We also believe the weak instability is less serious in that, unlike the strong instability, it is very sensitive to the tune spread within the bunch; by slightly increasing the tune spread (such as, for example, by adding a modestly powered, higher harmonic cavity to the ring [Chao 1995]), through Landau damping, the threshold to this kind of instability can be increased substantially.

In this section, we first obtain the wakefields of the main vacuum chamber objects, driven by a bunch that is significantly shorter than the nominal bunch length, using the computer program MAFIA [Klatt 1986]. These individual wake functions are then summed in the correct proportion to give a wakefield representing the entire ring. Finally, this wakefield is used as a Green function for calculating the effect of potential well distortion and for obtaining the threshold to the microwave instability. To obtain the bunch shape below threshold this wakefield is applied to the Ha¨ssinski formula [Ha¨ssinksi 1973]; for locating the threshold current it is applied to the Vlasov equation, which is solved in a perturbative manner using K. Oide's computer program [Oide 1990].

Calculations

One cannot predict the average bunch properties nor the threshold current of a ring without knowing the vacuum chamber geometry, from which they can calculate the wakefield or the impedance. As was the case for the SLC damping rings small changes in vacuum chamber cross-section—such as those connected to bellows, transitions, and masks—can dominate in their contribution to bunch lengthening and the microwave instability over larger objects such as the rf cavities [Bane 1988]. Therefore, it is important to know the details of the geometry of the vacuum chamber before beginning this work (as it is important to build the vacuum chamber to tight specifications during the construction phase). For the NLC damping rings, the main contributors to the longitudinal impedance have been designed: they are the 2 rf cavities, the 150 beam position monitors (BPMs), the longitudinal resistive-wall wakefield, the 50 synchrotron radiation masks, and the 50 tapers and pumping slots. It is assumed that the bellows that allow the ring to be assembled are shielded, leaving an impedance that is insignificant. Furthermore, it is assumed that the kicker chamber and septum region also do not contribute significantly to the impedance (Note that the important objects are all described in detail in Section 4.4.1).

The nominal rms bunch length in the NLC damping ring is 4 mm; for all our wakefield calculations we take a gaussian bunch with rms $\sigma_z = 1$ mm as the driving bunch and calculate the wakefield to 15 mm behind the bunch center (due to the large number of mesh points required for finding the wake of the rf cavities and the BPMs we could not easily

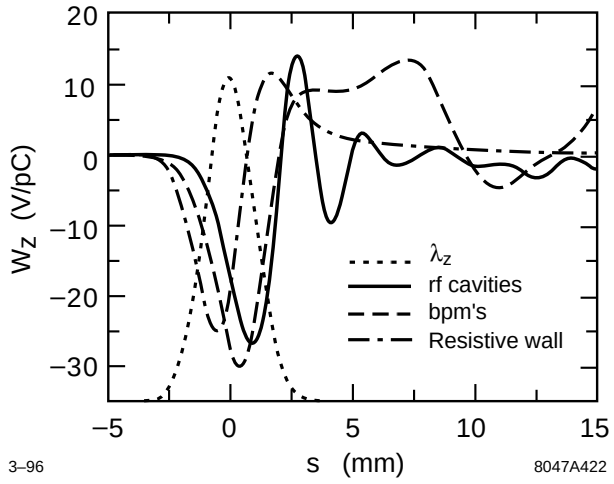

Figure 4-41. *The longitudinal wakefield left by a gaussian bunch, with $\sigma_z = 1$ mm, due to the rf cavities (the solid curve), the BPMs (the dashed curve), and the resistive-wall wakefield (the dot-dashes). The driving bunch shape is given by the dotted curve, with the head to the left.*

use a shorter driving bunch). We begin with the rf cavities. There are two single–cell cavities; each cavity is set back from the beam tube by a pair of gradual tapers. The total wakefield of the two rf cavities, as calculated by MAFIA, is shown in Figure 4-41 (the solid curve). We see contributions of both the setbacks and the cavity itself in the shape of the wake. The BPMs are of the button type; each BPM consists of four cylindrical, 8-mm-diameter electrodes that are set symmetrically (about the axis) into the beam tube wall; the impedance is due to the annular space that electrically isolates each button from the tube wall. The wakefield of the 150 BPMs is given by the dashed curve in Figure 4-41. We notice ringing at a frequency beyond 20 GHz.

The longitudinal resistive-wall wakefield can normally be ignored in impedance calculations of storage rings; for the NLC, however, its contribution is significant. For a gaussian bunch the resistive-wall wakefield is given by [Piwinski 1972]

$$W_z(s) = \frac{C}{4b\sigma_z^{3/2}}\sqrt{\frac{c}{2\pi\sigma}}f(s/\sigma_z) \quad , \tag{4.33}$$

with C the machine circumference, b the tube radius, σ_z the rms bunch length, σ the conductivity of the vacuum chamber walls; with

$$f(u) = |u|^{3/2}e^{-u^2/4}(I_{1/4} - I_{-3/4} \mp I_{-1/4} \pm I_{3/4})|_{u^2/4} \quad . \tag{4.34}$$

In Eq. 4.34 the upper signs apply for $u < 0$, the lower signs for $u > 0$; the modified Bessel functions I are evaluated at $u^2/4$. For the NLC damping ring we take $C = 223.5$ m, $b = 1.25$ cm, $\sigma_z = 1$ mm, and $\sigma = 3.2 \times 10^{17}$ s^{-1} (aluminum). The resulting resistive-wall wakefield is given by the dot-dashed curve in Figure 4-41. We note that, in amplitude, the cavities, the BPMs, and the resistive-wall contribute about equally to the total wakefield of a 1-mm bunch. As final ingredients we have also obtained the wakefields of the 50 synchrotron radiation masks and the 50 tapers and pumping slots; these contributions are small compared to the wakefields discussed above.

Summing all the contributions we obtain the wakefield that we will use as a Green function to represent the entire NLC damping ring (see Figure 4-42). One important subtlety is that, since it has a leading tail, our Green function is not causal. To obtain a causal Green function we will consider two ways of modifying the leading tail. The first method, which we call the capacitive approximation, is obtained by flipping the leading tail to the back, about $s = 0$, and adding it to the wake. The second method, which we call the resistive approximation, is obtained by replacing the leading tail by a delta function at the origin that has the same area as the leading tail. In the following we will

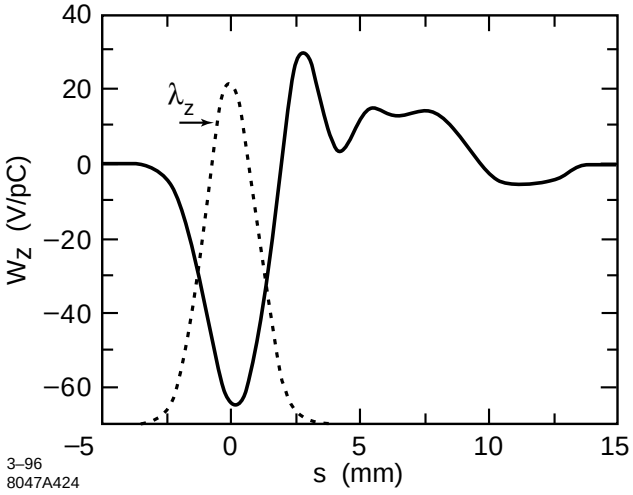

Figure 4-42. *The total longitudinal wakefield left by a gaussian bunch, with $\sigma_z = 1$ mm, on each turn in the NLC damping ring. The driving bunch shape is given by the dotted curve, with the head to the left.*

compare the results using these two versions of the Green function. If the bunch used to calculate the Green function is sufficiently short, then the results for the two cases should be nearly the same.

To obtain the longitudinal bunch distribution λ_z we apply the total wake function to the Ha¨ssinski equation [Ha¨ssinksi 1973]

$$\lambda_z(s) = K \exp\left(-\frac{s^2}{2\sigma_{z0}^2} + \frac{1}{V'_{rf}\sigma_{z0}^2}\int_0^s V_{ind}(s')\,ds'\right) \quad , \tag{4.35}$$

with K a constant that gives $\int_{-\infty}^{\infty}\lambda_z(s)\,ds = 1$, σ_{z0} the nominal (zero current) bunch length, V'_{rf} the slope of the rf voltage at the synchronous phase, and

$$V_{ind}(s) = eN\int_0^{\infty}\lambda_z(s-s')W_z(s')\,ds' \quad , \tag{4.36}$$

with eN the total bunch charge. For $N = 1.57\times10^{10}$, $\sigma_{z0} = 4$ mm, $V_{rf} = 1$ MV, rf frequency $f_{rf} = 714$ MHz, and synchronous phase (from the peak) $\phi = 50°$, we obtain the bunch shape and induced voltage shown in Figure 4-43 (the head of the bunch is to the left). [The result is essentially the same for both the capacitive and the resistive approximation to the Green function.] We note that the impedance is clearly resistive in character, *i.e.*, V_{ind} is roughly proportional to λ_z, and that the bunch shape is hardly perturbed from the nominal, gaussian one. The rms bunch length is increased by 6% to 4.23 mm and the centroid is shifted forward by 1.46 mm, to make up for the higher mode losses.

To estimate the threshold for the strong microwave instability we use the Boussard criterion [Boussard 1975]:

$$\frac{e\hat{I}|Z/n|}{2\pi\alpha_p E\sigma_\delta^2} \lesssim 1 \quad , \tag{4.37}$$

with $\hat{I}$ the peak current; $|Z/n| = |Z|\omega_0/\omega$ where Z is the impedance at frequency ω and ω_0 is the revolution frequency (for an inductive impedance $|Z/n|$ is a constant); α_p is the momentum compaction, E the beam energy and σ_δ the rms relative energy spread. The above criterion, if satisfied, indicates that the beam is stable. Note, however, that the Boussard criterion is only a very rough criterion, used to obtain an approximate idea of where the threshold to the strong instability might be. For the NLC, since the impedance is resistive it can be characterized by a resistance R, with

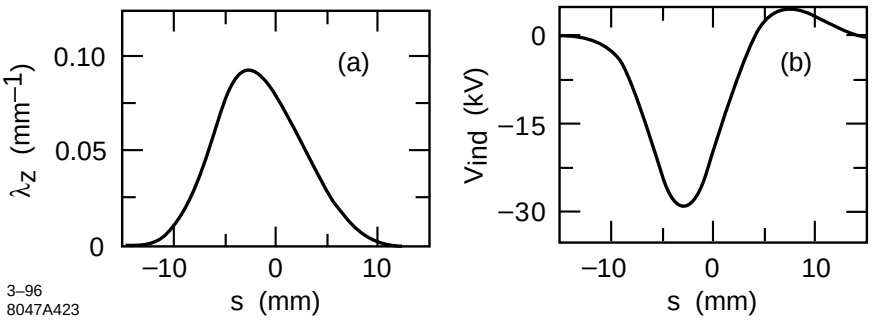

Figure 4-43. *The NLC damping ring bunch shape (a) and the induced voltage (b) when $N = 1.57 \times 10^{10}$, $V_{rf} = 1$ MV, $\phi = 50^{\circ}$. The head of the bunch is to the left.*

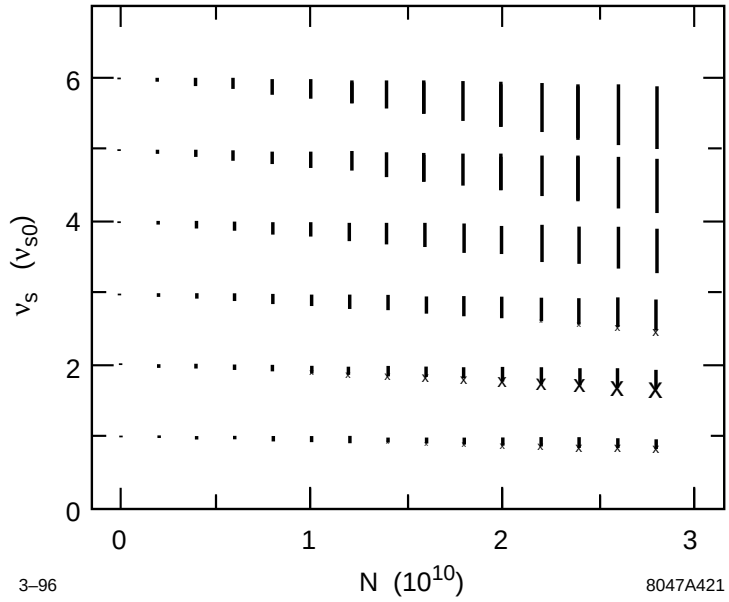

Figure 4-44. *The modes obtained by the Vlasov method when the capacitive model to Green function is used. Stable modes are represented by a dot, unstable modes by an `X', with the size proportional to the growth rate.*

the induced voltage given by $V_{ind} = -eNcR\lambda_z$. Fitting to this equation we find that the effective resistance of the damping ring $R \approx 250\,\Omega$. Let us take as typical bunch frequency $\omega \sim c/\sigma_z$, which gives $|Z/n| \approx R\sigma_z\omega_0/c = 0.03\,\Omega$. Then, using the same parameters as above, and taking $\alpha_p = 4.7 \times 10^{-4}$, $E = 2\,\text{GeV}$, and $\sigma_\delta = 9 \times 10^{-4}$, we find that the left hand side of Eq. 4.37 equals 0.5, suggesting that, at the highest envisioned current, we are still below the threshold for a strong instability.

To get a better estimate of the instability threshold, we have applied our wakefield to K. Oide's computer program that solves the linearized, time-independent Vlasov equation [Oide 1990]. This program uses a perturbation approach to find the threshold; it includes the potential well distortion as a zeroth order effect. This program solves for the modes of the system, and finds the mode that first becomes unstable. (For the SLC damping ring, the results of this program have been shown to agree very well with turn-by-turn tracking using a large number of macro-particles [Bane 1995a, Bane 1993]). For our simulation, we take as nominal synchrotron frequency $\nu_{s0} = 0.004$, and truncate the system matrix to six mode numbers in the azimuthal direction and 60 in the radial direction.

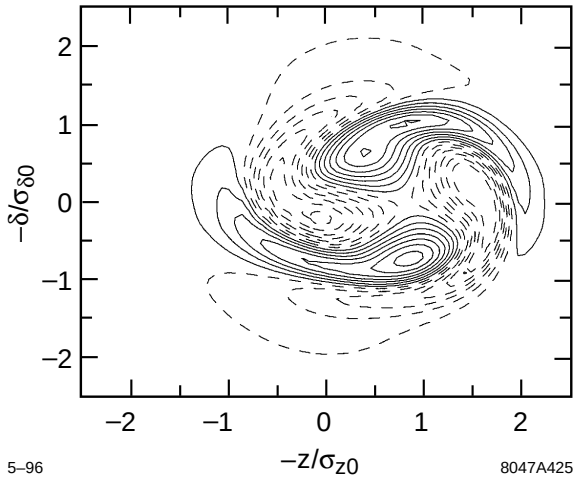

Figure 4-45. *The shape of the weak mode found at $N = 2 \times 10^{10}$ when the capacitive approximation to the Green function is used.*

The results are shown in Figure 4-44 where we plot the dependence of mode frequency on current for the capacitive approximation to the Green function. Stable modes are represented by a dot (note that at $N = 0$ for every azimuthal mode number there are 60 dots with the same frequency); unstable ones are indicated by an 'X', with the size of the symbol proportional to the growth rate (synchrotron radiation damping is not included in the calculation). We see that for each azimuthal mode number, at least up to the nominal maximum current ($N = 1.57 \times 10^{10}$), the frequencies are spread and depressed only slightly, which is typical behavior for a resistive impedance. The synchrotron radiation damping time of the NLC damping ring is $t_z = 2.5$ ms. The growth rate of an unstable mode first matches this value at $N = 1.65 \times 10^{10}$. The unstable mode is a quadrupole mode of the weak type, with frequency $1.8\nu_{s0}$ (its shape is plotted in Figure 4-45). In this example, the nearest strong instability is at $N = 7 \times 10^{10}$.

If, instead, we take the resistive approximation to the Green function we find that the growth rate of the weak instability is below the synchrotron radiation damping all the way up to the threshold of the strong instability, which, in this case, we find at $N = 8 \times 10^{10}$. The true result for our model damping ring is probably somewhere between the results given by the capacitive and the resistive model to the Green function, which suggests that at the highest design current no microwave instability will be encountered in the NLC damping rings. To obtain a more precise result of the location of the instability thresholds we need to get the wakefields for the NLC damping ring vacuum chamber due to a bunch with an rms that is significantly shorter than the current value of 1 mm.

4.4.3 Single-Bunch Transverse Mode Coupling

Transverse coupling will set a limit on the maximum single bunch beam current. In addition, the mode coupling threshold will be modified by the coupling between the bunches [Berg 1995]. In this section, we calculate the single bunch mode coupling threshold and then describe the modification of the results due to the bunch trains; the coupled-bunch instabilities are described in a later section.

In the NLC damping ring, the vertical plane results are universally worse than those for the horizontal plane, so only the vertical plane will be discussed here. The details of these calculations is given in Ref. [Berg 1995].

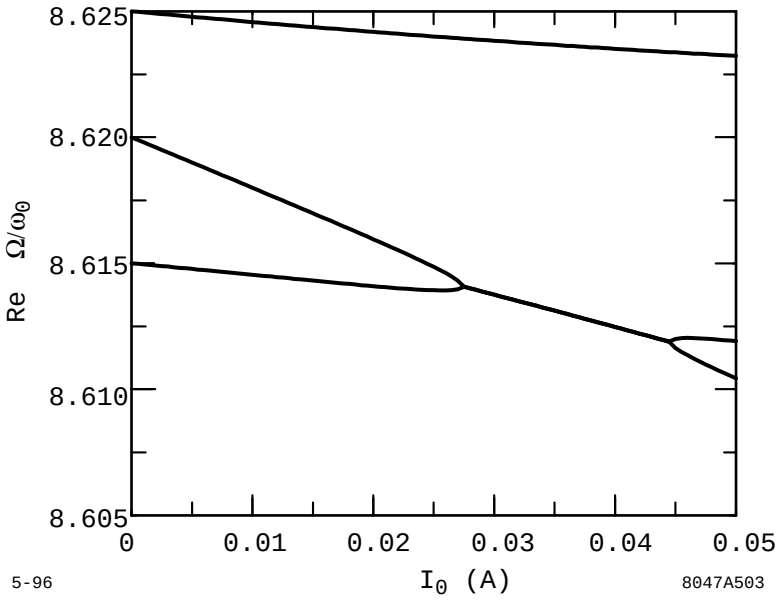

Figure 4-46. *Single-bunch vertical mode coupling.*

We use the broadband model of the transverse impedance and the transverse cavity higher-order modes given in Section 4.4.1. Note that the cavity higher-order modes as well as the part of the broadband impedance due to cavity tails must be enhanced by a factor of the β-function at the cavities (taken to be 6.5 m) over the average β-function (4-m vertical).

If only a single bunch is considered, transverse-mode coupling is seen at around 28 mA, as shown in Figure 4-46; the threshold is almost identical whether the rf cavities are de$Q$ed to 100 or 3000. For comparison, the damping ring single bunch current is much less, roughly 3.3 mA.

If we consider 532 symmetrically placed bunches, we find that the rigid ($m = 0$) coupled-bunch motion is only very slightly affected by mode coupling at the typical currents but the $m = 1$ coupled-bunch growth rates are strongly affected. If the rf cavities are de$Q$ed to around 100, the resulting growth rates are well below radiation damping at a beam current of 1.2 A. If the some cavity modes are left with Qs around 3000, the growth rates can become comparable to to the radiation damping rate. Additional details will be discussed in the section on transverse coupled-bunch instabilities.

4.4.4 Bunch-to-Bunch Synchronous Phase Variation

At any given time, there will be four trains of 90 bunches in the main damping rings. Within a train, the bunches populate adjacent buckets and between trains there is a gap that extends over 43 buckets. A consequence of an uneven filling scheme is that within each train the synchronous phase will vary from bunch to bunch. After extraction the beam enters the bunch compressors and then the X-band linac. The phase variation in the ring, if uncompensated, will lead to a phase variation in the X-band linac which, in turn, will result in an unacceptable spread in the final energy of the bunches in a train. The synchronous phase variation, however, can be compensated, either in the damping ring itself or in the bunch compressors that are described in Chapter 5. The present NLC design assumes that later method of

compensation and the bunch compressors have been designed to accommodate a ± 20 ps variation in the synchronous phase.

In this section, we first find the synchronous phase variation across the bunch trains of the NLC damping rings, and then we study a method of compensating this variation—one employing passive sub-harmonic cavities—in the damping ring itself. More details of this compensation technique can be found in Ref. [Bane 1995c].

The Variation in Synchronous Phase

Consider a damping ring filled with bunch trains, with N bunches per train, and let us suppose that we can ignore the effects of higher cavity modes. Let us further assume that the bunch gap is short, *i.e.*, $|\Delta\bar{\omega} T_g| \ll 1$, with T_g the gap time interval, and

$$\Delta\bar{\omega} = \Delta\omega + i\frac{\omega_{rf}}{2Q_L} \quad , \tag{4.38}$$

where $\Delta\omega$ is the frequency detuning, ω_{rf} the fundamental frequency, and Q_L the loaded Q of the cavity. Then the steady-state phase difference between the first and last (N^{th}) bunch in each train is given by [Lambertson 1995]

$$\Delta\phi_{1N} \approx -\frac{2kI_0T_g}{V_c \sin\phi} \quad , \tag{4.39}$$

with k the loss factor ($= \frac{1}{2}\omega_{rf} R/Q$), I_0 the average beam current, V_c the peak voltage, and ϕ the nominal synchronous phase ($\phi = \cos^{-1}[U_0/eV_c]$, where U_0 is the energy loss per turn). The average beam current I_0 is given by

$$I_0 = \frac{Nq}{NT_b + T_g} \quad , \tag{4.40}$$

with q the charge per bunch and T_b the bunch-to-bunch time interval within a train. The negative sign in Eq. 4.39 indicates that the synchronous phase of the last bunch is more forward (toward the crest) than the first bunch. Note also that in the NLC damping rings not only is the gap short but also the bunch train itself, *i.e.*, $|\Delta\bar{\omega} N T_b| \ll 2\pi$; it can easily be shown [Bane 1995c] that in such a case the synchronous phase varies linearly with bunch number within each bunch train.

For the NLC damping rings the rf frequency is 714 MHz and the R/Q for the two rf cavities combined is 240 Ω; therefore, $k = 0.54$ V/pC. We take $N = 90$, $q = 2.5$ nC, $T_b = 1.4$ ns, and $T_g = 60.2$ ns; therefore, $I_0 = 1.2$ A. Taking $V_c = 1$ MV and $\phi = 50°$ we obtain $\Delta\phi_{1N} = -5.8°$. We have also numerically simulated this problem using turn-by-turn tracking [Thompson 1991]. The unloaded Q of the cavities was taken to be $Q_0 = 25500$; for minimum reflected power $Q_L = 2200$ and $\psi = -44.5°$ (remember: $\tan\psi = 2Q_L\Delta\omega/\omega_{rf}$). The results are shown in Figure 4-47. Plotted are the shift in synchronous phase $\Delta\phi$ versus bunch number. We see that, over each train, the variation is linear with bunch number, and that the total phase shift is $-5.9°$, in good agreement with our analytical results. Note that both the length of the gap and the length of the bunch train are short according to our criteria: $|\Delta\bar{\omega} T_g| = 0.003 \ll 1$ and $|\Delta\bar{\omega} N T_b| = 0.2 \ll 2\pi$.

It may occasionally happen that one bunch train has a slightly different charge than the others. To study the sensitivity to this we have repeated the numerical tracking but with the bunches of the first train having only 95% of the nominal charge. The results are shown in Figure 4-48. In this case the maximum phase deviation in the first train has been reduced to 80%, in the other three trains to 95%, of the value found for equally populated trains. Note, however, that the average value of $\Delta\phi$ for all trains has changed by 3°. This average change, however, can easily be corrected by a phase feedback system in the damping ring.

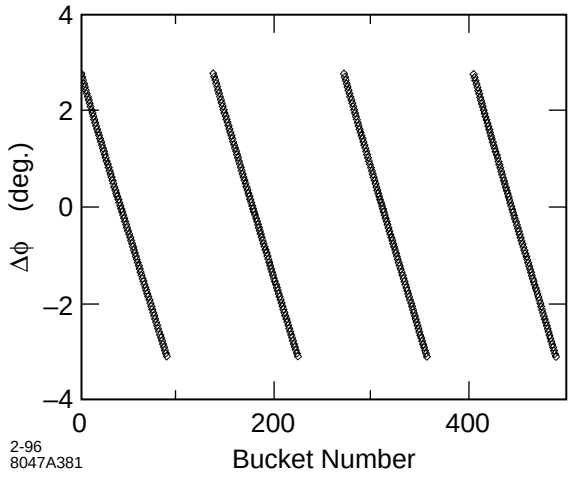

Figure 4-47. *The steady-state, bunch-to-bunch synchronous phase variation vs. bunch number for the NLC damping rings. Note that a more negative value of phase is more toward the front (toward the rf crest).*

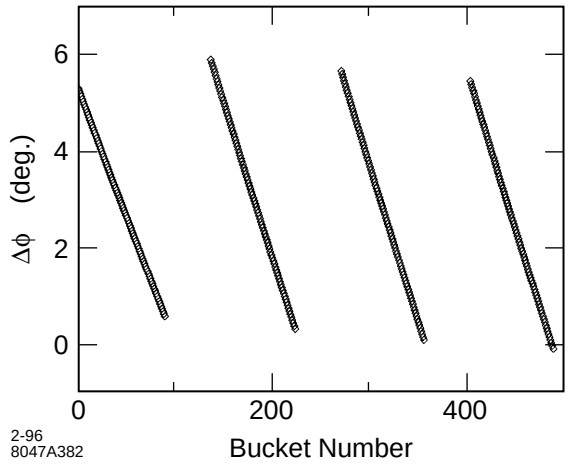

Figure 4-48. *The synchronous phase variation vs bunch number for the case when the bunches of the first train have only 95% of the nominal bunch population while the rest are unchanged.*

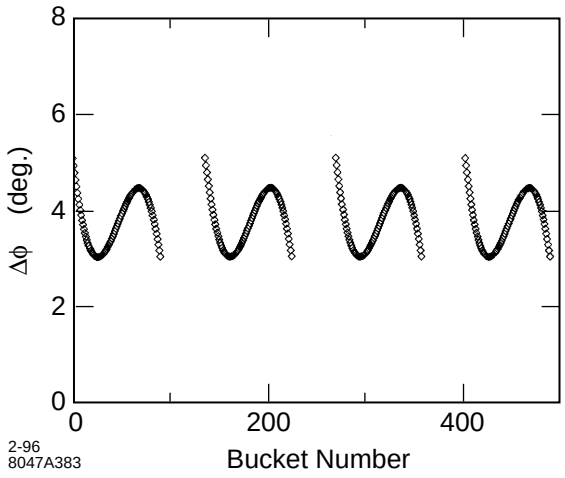

Figure 4-49. *The synchronous phase variation that can be achieved when one passive, lower harmonic cavity is used.*

Compensating the Variation in Synchronous Phase

Given a sufficient amount of extra power and bandwidth in the klystron, the synchronous phase variation discussed above can be compensated by properly varying the generator voltage as a function of time; this method will be studied in future work. However, here we will discuss a method of compensation described in Ref. [Kubo 1993], where the authors find that a properly tuned, passive, lower harmonic cavity can be used to compensate the phase variation due to bunch trains. The frequency of the compensation cavity must be equal to $\omega_{rf} - 2\pi n N_t/T_0$, with n an integer, N_t the number of bunch trains, and T_0 the revolution time. This method of compensation works quite well when the gap length is larger than the length of a bunch train. In our case, however, the gap length is only about half the train length. We will, therefore, also investigate the effect that can be obtained using two lower-harmonic cavities to compensate the synchronous phase variation.

Figure 4-49 gives the tracking results when an optimally-tuned, passive cavity with frequency $\omega_{rf} - 8\pi/T_0$ is included in the damping ring. The parameters of this cavity were optimized numerically. They are: $R/Q = 34\ \Omega$, $Q_0 = 3.43 \times 10^4$, $Q_L = 1.14 \times 10^4$, and $\psi = -85°$. We see from the figure that the maximum phase deviation has been reduced to $2.1°$, which is only a factor of 3 smaller than we had initially. Adding a second, passive cavity, with frequency $\omega_{rf} - 16\pi/T_0$, $R/Q = 18\ \Omega$, $Q_0 = 3.43 \times 10^4$, $Q_L = 1.0 \times 10^4$ and $\psi = -82°$ gives the results shown in Figure 4-50. Now the maximum phase deviation has been reduced to $0.65°$, which is a factor of nine smaller than we started with. Finally, note that the R/Qs of the compensation cavities are very small, so they should not contribute to an instability. One negative point, however, might be that the residual phase variation is nonlinear with bunch number, an effect which may have its own negative ramifications.

At this time, we have decided not to compensate the loading in the rings. The $\pm 3°$ L-band variation across the bunch train can be easily accommodated in the bunch compressors as described in Chapter 5. Furthermore, because the variation is linear across the bunch train, it may be straightforward to correct the resulting energy variation in the prelinac before the second compressor. This would allow a simpler design for the second compressor system.

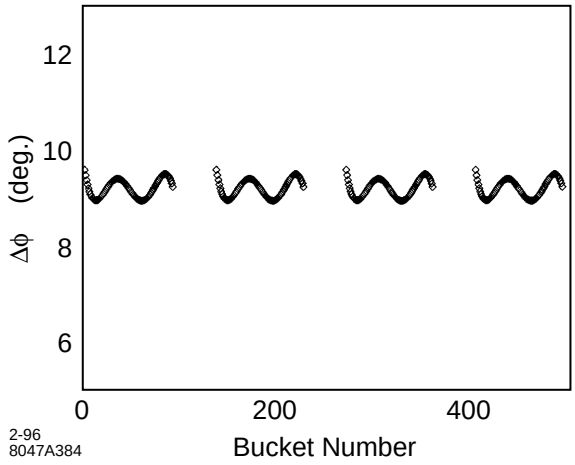

Figure 4-50. *The synchronous phase variation that can be achieved when two passive, lower harmonic cavities are used.*

4.4.5 Coupled Bunch Instabilities

The close spacing of bunches (1.4 ns) within a train in the main damping rings allows for the possibility that bunch wakefields will influence the motion of consecutive bunches. In general, such wakefields arise from narrow-band resonances in the rf cavities and from the finite conductivity of the vacuum chamber wall. Under certain conditions, the wakefields can generate a transverse or longitudinal coherent structure in the relative motion of the bunches which grows exponentially, leading to a loss of beam quality and/or loss of the beam itself. This is referred to as a coupled-bunch instability. The wakefields can also create static offsets in either the transverse or longitudinal position along the bunch train due to the nonuniform filling pattern of the ring. Furthermore, the restraints on beam size and bunch phase at extraction require control of beam oscillation transients from injection errors. These effects are generally proportional to the total beam current and thus are a concern for the 1.2-A design current for the main damping rings.

At the time of this study, the HOMs of the damping ring cavities were not available. Thus, we have estimated these various effects for the main damping rings assuming a scaled-down version of the PEP-II rf cavity as the primary source of narrow-band resonances, where the cavity size has been reduced such that the fundamental mode frequency has increased from 476 to 714 MHz. The strongest monopole and dipole higher-order-modes (HOMs) are given in Tables 4-18 and 4-19. It is also assumed that all HOMs are damped to $Q < 200$. The effects are calculated for two identical rf cells with a total voltage of 1 MV.

Longitudinal

In the longitudinal plane, coupled-bunch oscillations are driven only by the monopole HOMs of the rf cavities. Assuming a uniformly filled ring, the growth rate for dipole oscillations is given by

$$\frac{1}{\tau} = \frac{1}{2}\frac{I_0 \alpha_p f_{rf}}{(E/e)Q_s}\left[Z_{||}\right]_{\text{eff}} \tag{4.41}$$

where the effective impedance is

$$\left[Z_{\|}\right]^{l}_{\text{eff}} = \sum_{p=-\infty}^{p=+\infty} \frac{\omega_p}{\omega_{rf}} e^{-(\omega_p \sigma_\tau)^2} Z_{\|}(\omega_p) \ . \tag{4.42}$$

f_r (MHz)	R_s (kΩ)
3060.85	2.6
1941.55	1.8
2291.94	1.8
4563.48	0.66
1487.27	0.52
4150.84	0.52
3368.43	0.46
3554.05	0.36
5180.54	0.32

Table 4-18. *Strongest rf cavity monopole HOMs.*

f_r (MHz)	$R_\perp$ (kΩ/ m)
1193.2	85
2499.8	72
1988.2	36
2397.2	11.2
2310.6	9.7
4861.2	7.8
3755.4	7.0
3603.0	4.8
3423.6	3.8
4736.2	3.8
3346.5	2.6

Table 4-19. *Strongest rf cavity dipole HOMs.*

The effective impedance and the corresponding growth rate are shown in Figure 4-51. For $Q < 200$ the fastest growth rate falls approximately a factor of two below the radiation damping rate, indicating stable oscillations. The above applies strictly to a uniform fill pattern with every rf bucket filled. The effects of instabilities are typically lessened by nonuniform fill patterns. More detailed simulations are required to study transient effects including the gaps between bunch trains.

The growth rates are insensitive to tuning of the HOM frequencies because of the relatively large bandwidth of the HOMs as compared to the revolution frequency. Landau damping from a tune spread within the bunch is not effective because of the short bunch length. Coupled–bunch shape oscillations, *i.e.*, $m > 0$, are not driven by the HOMs at a significant level. Also, with the nominal detuning, the fundamental mode impedance does not drive any coupled–bunch instabilities at a rate comparable to the radiation damping rate.

Transverse

Coupled-bunch oscillations in the transverse planes are driven by dipole rf cavity HOMs and by the resistive-wall impedance. The HOMs given in Table 4-19 are assumed to be equally strong in the horizontal and vertical planes. The resistive-wall impedance results from the finite conductivity of the vacuum chamber wall and for a round pipe of

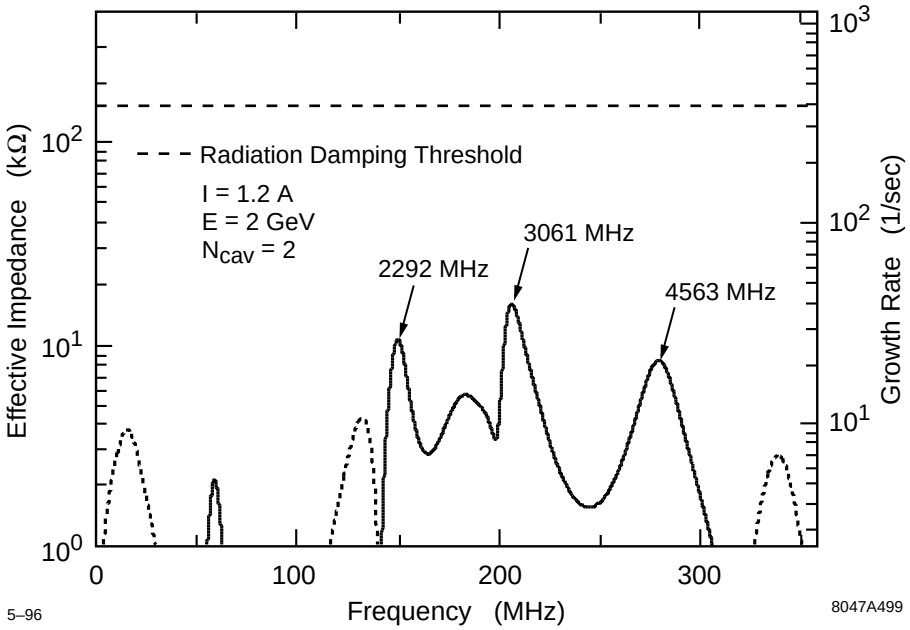

Figure 4-51. *Longitudinal coupled-bunch growth rates.*

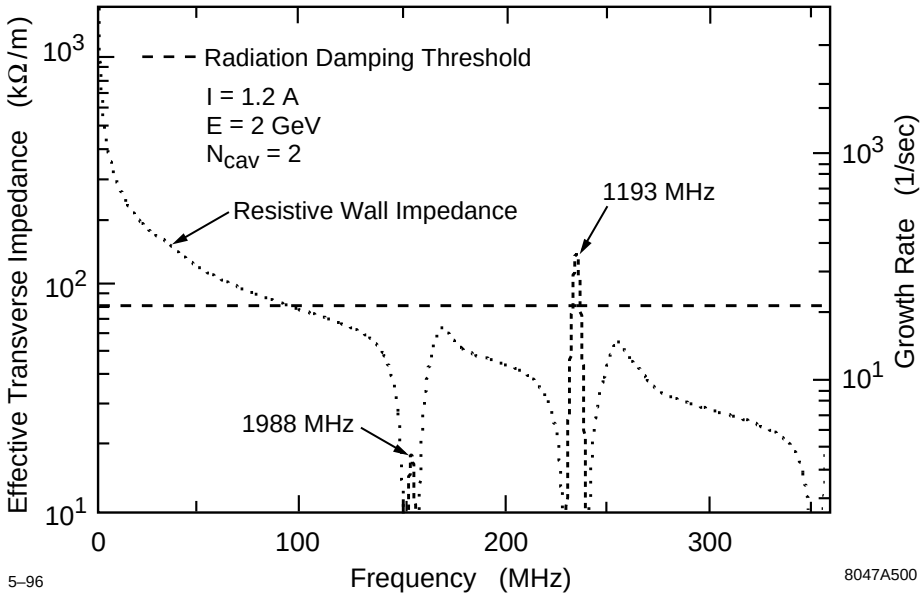

Figure 4-52. *Transverse coupled-bunch growth rates.*

radius b and resistivity ρ is given by

$$Z_{\perp}(\omega) = (1+j)\frac{cL}{\pi b^3}\sqrt{\frac{\rho\mu_0}{2}}\frac{1}{\sqrt{\omega}} \tag{4.43}$$

For a 1.25-cm-radius Al beam pipe, the net resistive-wall impedance is given as

$$Z_{\perp,RW} = (1-j)\frac{0.48}{\sqrt{n}}\ M\Omega/m \tag{4.44}$$

where $n = \omega/\omega_0$.

Assuming a uniformly filled ring, the coupled-bunch growth rate for dipole oscillations of the beam is given by

$$\frac{1}{\tau} = \frac{1}{2}\frac{I_0 f_0}{(E/e)}\beta_{\perp} j[Z_{\perp}]_{\text{eff}} \tag{4.45}$$

where the effective impedance is given by

$$[Z_{\perp}]_{\text{eff}} = \sum_{p=-\infty}^{p=+\infty} e^{-(\omega_p\sigma_\tau)^2} Z_{\perp}(\omega_p) \tag{4.46}$$

The effective impedance and the corresponding growth rates are shown in Figure 4-52. The resistive-wall impedance dominates mainly because of the small vacuum chamber. The large growth rate in excess of radiation damping will require a feedback system to damp transverse beam oscillations; this is described in Section 4.7. Higher-order head–tail modes are not driven at a significant level by the HOMs for $Q < 3000$.

There is a transient beam loading of the transverse impedance analogous to that of the longitudinal which could possibly result in a variable transverse offset along the length of the bunch train. This effect has not yet been studied in detail but it not expected to be significant.

4.4.6 Ion Trapping

The cross section for ionization of the residual gas is larger than that of elastic scattering or bremsstrahlung (compare Section 4.4.9). For carbon monoxide CO and a beam energy of 50 GeV, it is about 2 Mbarn [Rieke 1972]. The main effect of the residual gas on the beam is thus due to the creation of ions. The ions are produced at a rate of about $2\ p$[nTorr] s^{-1} or $6.5\ p$[Torr] m^{-1} ions per electron. The large bunch gap of 60 ns prevents ions from being trapped between bunch trains. Computer simulations may need to be performed to determine the fraction of ions which remains trapped during the gap but this is expected to be extremely small $\lesssim 10^{-3}$.

At the end of a single bunch train the longitudinal density of ions created by the train is 9×10^4 m^{-1} at a pressure of 10^{-8} Torr, assuming 90 bunches of 1.5×10^{10} electrons each. Particles in the trailing bunches then suffer a vertical tune shift of $\Delta Q_y \approx 0.02$. To limit this effect, we are designing the main damping ring vacuum system to achieve a pressure less than 5×10^{-9} Torr.

It has been predicted that the interaction of beam and ions also gives rise to a fast transverse beam-ion instability [Raubenheimer 1995a]. It is because of this instability that the present target for the Damping Rings is a vacuum level as low as 10^{-9} Torr. For an electron beam, the instability mechanism is the following. Ions created by the first bunches perturb the tail of the bunch train. The mutually driven transverse oscillations of beam and ions result in a

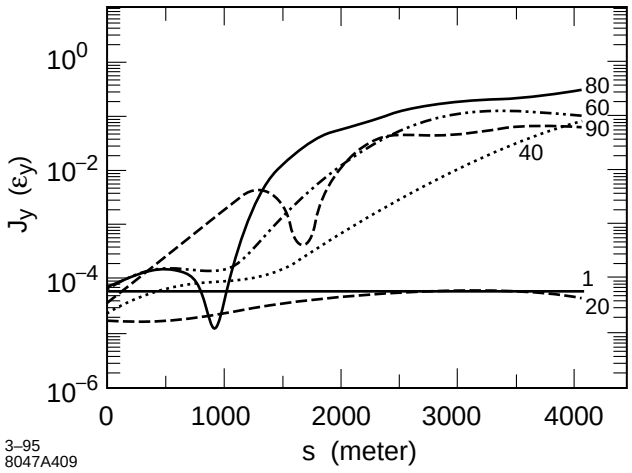

Figure 4-53. *Growth of the action for every twentieth of 90 bunches in the NLC damping ring for a pressure of* 10^{-8} *Torr, an atomic mass of 28 (carbon monoxide), and* 1.5×10^{10} *particles per bunch.*

fast multi-bunch instability. The growth time of this instability at the end of the bunch train is given by

$$\tau_{\mathrm{asym,e-}}^{-1}[\mathrm{s}^{-1}] \approx 5p[\,\mathrm{Torr}]\frac{N_b^{\frac{3}{2}} n_b^2 r_e r_p^{\frac{1}{2}} L_{\mathrm{sep}}^{\frac{1}{2}} c}{\gamma \sigma_y^{\frac{3}{2}} (\sigma_x + \sigma_y)^{\frac{3}{2}} A^{\frac{1}{2}} \omega_\beta} \tag{4.47}$$

where A denotes the atomic mass number of the ions, n_b the number of bunches, N_b the number of particles per bunch, L_{sep} the bunch spacing, r_p and r_e the classical proton and electron radius, respectively, c the velocity of light, and $\omega_\beta \approx 1/\beta_y$. The rise time τ_{asym} in Eq. 4.47 refers to the asymptotic equation (for large times t)

$$J_y \approx \frac{J_{y0}}{8\pi\sqrt{t/\tau_{\mathrm{asym}}}} \exp\left(2\sqrt{t/\tau_{\mathrm{asym}}}\right) \quad . \tag{4.48}$$

where J_y denotes the vertical action of the trailing bunch. The instability amplifies the Fourier component of the vertical bunch-to-bunch displacement which corresponds to the ion-oscillation frequency. Assuming the initial displacements are due to the finite number of electrons, the vertical action at time zero is given by $J_{y0} \approx \sigma_y^2/(N_b n_b 2\beta_y) \sim 3 \times 10^{-24}$ m. The rise time of Eq. 4.47 depends strongly on the number of bunches, the number of particles per bunch and the beam size. Due to the small vertical beam size and the rather large number of electrons, the growth times expected for the different NLC subsystems are exceedingly short.

In the electron damping rings, the predicted rise time for the trailing bunches is 100 ns at a pressure of 10^{-8} Torr. At 10^{-9} Torr the rise time would be 1 μs, which is still too short for a feedback system. However, when the instability grows from Schottky noise, about 200 rise times are required before the oscillation amplitude becomes of the order of the beam size. Moreover, decoherence and filamentation of the ions, not included in the derivation of Eq. 4.47, may lead to a further increase of the rise time by about a factor of two [Stupakov 1995]. Therefore, for the NLC damping rings a pressure of 10^{-9} Torr may be barely acceptable. An analytical treatment of the instability mechanism, computer simulations, possible remedies, and open questions are discussed in Ref. [Raubenheimer 1995a]. Figure 4-53 shows an example of the simulation results. The vertical action for different bunches of the train is depicted as a function of the traversed distance, for a pressure of 10^{-8} Torr. The rise times deduced from Figure 4-53 and the analytical estimate, Eq. 4.47, agree within a factor of two.

A positron bunch train deflects the equally charged ions and does not show the same ion-driven multibunch instability. However, single positron bunches may interact with the ionized electrons, which results in a similar instability, albeit

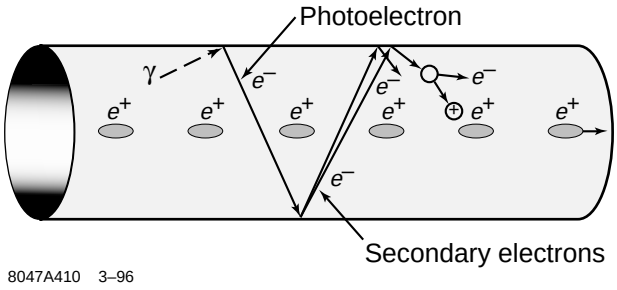

Figure 4-54. *Sketch of the beam-induced electron plasma.*

with larger rise times. In this case, the asymptotic growth rate at the bunch tail can be written as

$$\tau_{\mathrm{asym,e+}}^{-1}[\mathrm{s}^{-1}] \approx 7p[\,\mathrm{Torr}]\frac{N_b^{\frac{3}{2}} r_e^{\frac{3}{2}} \sigma_z^{\frac{1}{2}} c}{\gamma \sigma_y^{\frac{3}{2}} (\sigma_x + \sigma_y)^{\frac{3}{2}} \omega_\beta} \tag{4.49}$$

where σ_z is the rms bunch length. At a pressure of 10^{-9} Torr, the expected instability rise time for the positron Damping Ring is 120 μs. Since this is comparable to the synchrotron period (about 150 μs), the synchrotron motion will prevent the buildup of the instability.

Several possible remedies have been suggested for the multibunch instability [Raubenheimer 1995a]. First, additional gaps in a bunch train will alleviate the effect. Second, it may be possible to design lattices in which the ion frequency is strongly location-dependent. If the instability saturates at an amplitude of about one sigma, it is also conceivable to design damping rings in which the equilibrium emittance is about half the desired emittance. Preliminary simulation results indicate, however, that the saturation is not complete and that further amplitude growth at a smaller rate is possible. Finally, after extraction from the ring, fast kickers could realign the trailing bunches. Until the suitability of such schemes has been demonstrated, it will be assumed that in the damping rings of the NLC an average pressure of or below 10^{-9} Torr has to be maintained, to preserve the vertical emittance.

4.4.7 Positron-Electron Instability

Another instability that has been discussed is the positron-electron instability [Ohmi 1995]. This arises when an intense, positively charged bunched beam produces an electron cloud (or plasma) inside the vacuum chamber in which it travels. The basic mechanism is as follows: photons emitted due to synchrotron radiation hit the inside of the vacuum chamber and create photoelectrons. These, in turn, are accelerated transversely by the positively charged bunches and hit the wall on the opposite side of the vacuum chamber. Depending on their energy, these photoelectrons can be absorbed or can create secondary electrons. In this latter case, the secondaries are, in turn, accelerated, and the process is iterated, as sketched in Figure 4-54.

There are two effects from these electrons: they desorb gas molecules from the walls of the vacuum chamber and possibly ionize them, and they create an electron cloud. The gas desorption effect decreases in importance as the chamber gets "scrubbed" with increased use. But the electron cloud, of course, remains.

For high-enough current, a resonance occurs when the typical traversal time of the electrons across the chamber is equal to the time spacing of the bunches, leading to beam-induced multipactoring [Grobner]. But even for currents well below this threshold, as in the case of the NLC damping ring, the electron cloud still exists and couples the transverse motion of the bunches, leading to a potential coupled-bunch instability.

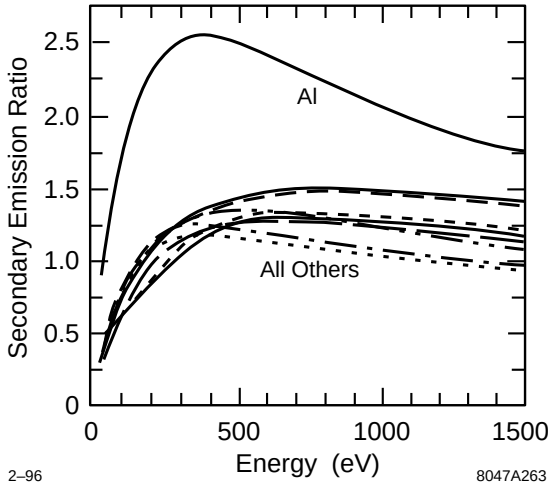

Figure 4-55. *The secondary emission ratio for various metals as a function of the incident electron energy in eV.*

Experimental evidence of such an electron-cloud instability has been reported at the KEK Photon Factory [Izawa 1995]. A related phenomenon has also been observed at CESR [Rogers 1995], in which case the electron cloud is not produced by the mechanism described, but by the trapping action of the combined electric and magnetic leak fields of the ion pumps. Although in this case the electron cloud occupies only a very small fraction of the vacuum chamber, it is enough to produce coupled-bunch motion. A theoretical explanation of the coupled motion based on the plasma idea has been put forward [Ohmi 1995], which predicts fairly fast growth rates for the instability. The predicted value for the onset of the instability is in rough agreement with the observations.

We have developed a simulation code [Furman 1995] and analytic calculations [Heifets 1995] to study this phenomenon at the NLC damping ring and the PEP-II positron beam. An important ingredient of the simulation is secondary electron emission. Figure 4-55 shows experimental measurements of the emission ratio for various metals (these curves are incorporated into the simulation code). Aluminum has the highest ratio, and that all other metals are not too different from each other.

Preliminary simulation results show that, for the nominal main damping ring parameters, an uncoated Al vacuum chamber would lead to a fast avalanche of electrons following injection into the machine. This avalanche would eventually stop due to the repulsive nature of the space-charge force of the electron cloud [Heifets 1995]. Even so, it is likely that the resultant instability would be difficult to control. On the other hand, if the vacuum chamber is coated with any of the other metals indicated in Figure 4-55, the simulation shows that the electron cloud density reaches saturation even if space-charge effects are not taken into consideration. The reason for this equilibrium state is a balance between the predominant absorption of the electrons upon hitting the walls, and the creation of photoelectrons following the passage of every bunch through the bending magnets.

For the nominal Main Damping Ring current and bunch spacing, the characteristic time of the plasma is < 10 ns. Thus a beam gap equivalent to a few bunch spacings makes the plasma disappear altogether. This implies that there will be no turn-to-turn coupling. If a leading bunch oscillates transversely, the electron plasma will act as a coupler and drive the trailing bunches. The amplitude of the driven bunches will grow linearly with time with a characteristic time scale estimated at 0.2 ms. Thus the feedback system will need to be able to damp instabilities of this time scale. However, we should point out that this is a subject of ongoing research and the correct answer may differ substantially.

There have been a number of solutions proposed for this effect. One such solution would place strips of ceramic, coated with thin conducting layer, along the edges of opening of the ante-chamber. Biased with a low DC voltage,

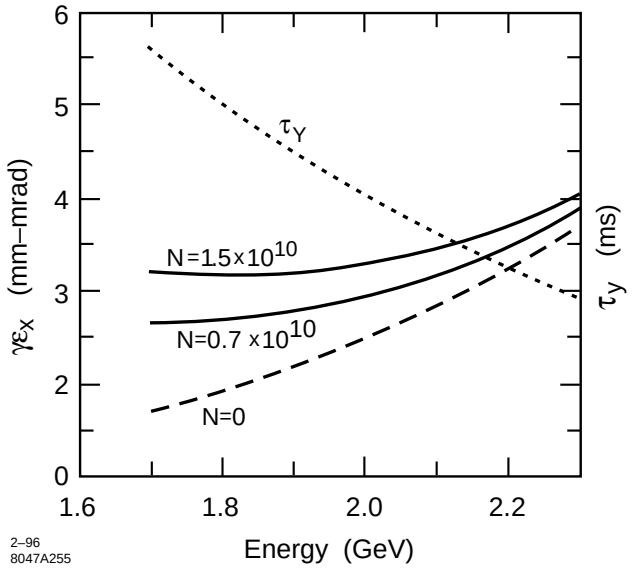

Figure 4-56. *Horizontal equilibrium emittance and vertical damping time versus ring energy for different single bunch charges.*

such a design may prohibit production of the photo-electrons and eliminate the photo-electron driven instability of the positron storage rings.

Finally, this effect may be important in the pre-damping ring as well as in the positron main damping ring. At this time, we have not evaluated the effect for those parameters.

4.4.8 Intrabeam Scattering

Intrabeam scattering is a very significant effect in the main damping rings because of the small normalized emittances; it has negligible effect in the pre-damping ring. In the main damping rings, intrabeam scattering has been calculated with ZAP [Zisman 1986]. Figure 4-56 is a plot of the horizontal emittance and the vertical damping time versus the ring energy. The vertical damping time is the dotted curve and there are three curves for the horizontal emittance: $N = 1.57 \times 10^{10}$ (solid), $N = 0.7 \times 10^{10}$ (solid), and $N = 0$ (dashes). The intrabeam scattering emittance growth was calculated by ZAP. Notice that the emittance decreases to a minimum as the ring energy is decreased to roughly 1.8 GeV. Unfortunately, the vertical damping time increases rapidly as the energy is decreased and, at an energy of 1.7 GeV, the damping time would only allow operation at 120 Hz.

At the nominal energy of 1.98 GeV for 180-Hz operation, ZAP estimates the horizontal emittance as roughly 3.30×10^{-6} m-rad at a charge of 1.5×10^{10} and 2.96×10^{-6} m-rad at a charge of 0.7×10^{10}. But, ZAP calculates the rms growth of the beam size. Because of the fast damping times, a significant fraction of the rms growth is actually contributions to the beam halo and not an increase of the beam core [Raubenheimer 1994]. This results in a correction for the growth of the core that, for the NLC main damping ring parameters, is roughly 30%. Thus, at 1.98 GeV, with the maximum beam charge, we expect the horizontal core emittance to increase to 3.1×10^{-6} m-rad; at lower charge, the growth is less.

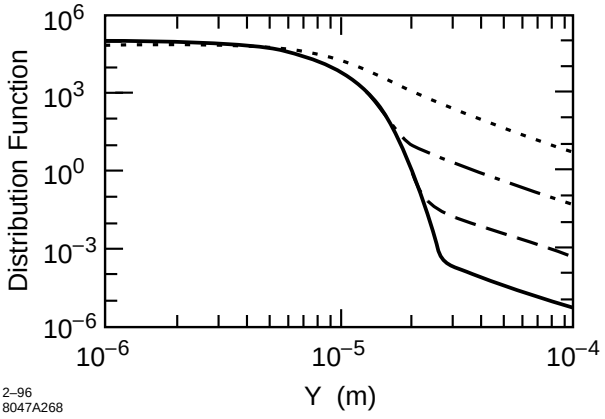

Figure 4-57. *Beam distribution in the NLC damping ring with CO gas pressures of 10^{-12} Torr (solid), 10^{10} Torr (dashed), 10^{-8} Torr (dot-dash), and 10^{-6} Torr (dotted).*

It is important to note that the scattering in the vertical plane will be less than in the horizontal plane [Raubenheimer 1993b]. This arises because intrabeam scattering emittance growth occurs due to changes in the longitudinal particle energy from the scattering. It is similar to the emittance growth from synchrotron radiation, except the intrabeam scattering occurs throughout the ring while the synchrotron radiation only occurs in the bending magnets. In a storage ring, the horizontal dispersion is minimized at the bends while the vertical dispersion, which is due to errors, is relatively uniform in magnitude around the ring. Thus, the intrabeam emittance growth has a much larger relative contribution to the horizontal emittance than the vertical emittance. We have not yet calculated the vertical growth for the NLC parameters, but experience with the KEK ATF damping ring suggests that the vertical emittance growth should be roughly 30% of the horizontal growth. In this case, the vertical emittance growth due to intrabeam scattering will not be significant.

4.4.9 Beam-Gas Scattering

The vacuum pressure in the NLC damping rings will be less than 10^{-8} Torr. This is low enough so that scattering with residual gas atoms does not limit the beam lifetime or dilute the vertical emittance. The tolerable vacuum level is determined from several different effects. First, elastic scattering on atomic nuclei may increase the equilibrium emittance. The cross section for this process is about

$$\sigma_{\rm scatt} \approx \sum_i 4\pi\alpha^2 Z_i^2 (1.4 a_0 Z_i^{-\frac{1}{3}})^2 \tag{4.50}$$

where α denotes the fine structure constant, a_0 Bohr's radius, and Z_i the atomic number. The sum is over all atoms of a molecule. For carbon monoxide, CO, a common molecule in accelerator vacuum systems, we have $\sigma_{\rm scatt} \approx 0.5$ Mbarn. At a pressure of 10^{-8} Torr, an electron undergoes no more than 5 collisions per second, and, therefore, during a vertical damping time of 4.8 ms only a small halo is created around the undisturbed beam core [Hirata 1992, Raubenheimer 1992]. Figure 4-57 shows the beam distribution due to gas scattering for several vacuum pressures [Raubenheimer 1992].

Second, the beam lifetime is reduced by bremsstrahlung in the field of the atomic nuclei [Piwinski 1985]. In this case the cross section is

$$\sigma_{\rm brems} \approx \sum_i \frac{4}{3} 4 r_e^2 Z_i^2 \alpha \ln \frac{E}{\Delta E} \ln \frac{183}{Z_i^{-\frac{1}{3}}} \tag{4.51}$$

where r_e is the classical electron radius, and $\Delta E/E \approx 10^{-2}$ the energy acceptance of the ring. Again for CO, the cross section is $\sigma_{\rm brems} \approx 6$ barn, which translates into a beam lifetime of 5 hours at a pressure of 10^{-8} Torr.

4.4.10 Lifetime Limitations

In a damping ring, it is unlikely that the beam lifetimes could limit the operation of the ring since the beams are stored for a very short time. But, poor beam lifetimes could make commissioning and studying the ring difficult. The primary beam lifetime limitations are excessively small apertures, beam-gas scattering, and the Touschek effect; the latter refers to large-angle collisions between particles within the beam that lead to particle loss.

With adequate design and tolerances, one should be able to avoid the first limitation. In addition, with reasonable vacuum pressures, the lifetime due to beam-gas scattering should not be significant. Assuming a pressure of 10^{-8} Torr in the NLC damping rings, the lifetime due to beam-gas scattering is roughly four hours; this is more than sufficient.

In contrast, the Touschek lifetime will tend to be severe in the main damping rings since it depends inversely upon the particle density in the beam. In the NLC main damping rings, the Touschek lifetime is roughly two minutes. While this is long compared to the operating beam storage time of 22 ms, it may be too short to study the properties of a stored beam. In this case, one can increase the vertical beam size or decrease the number of particles per bunch, thereby decreasing the beam density and increasing the lifetime.

4.4.11 PPDR Collective Limitations

Collective effects are not expected to be significant in the Positron Pre-Damping Ring. The PPDR has a longer bunch length and a larger vacuum chamber, reducing the contributions to the broadband impedance and the resistive-wall impedance. Thus, the growth rates of the coupled-bunch instabilities, that are driven by the resistive-wall impedance, should be well below the radiation damping rate. In addition, the longitudinal microwave threshold should be increased substantially due to the lower impedance and the larger momentum compaction. Finally, issues such as the Touschek lifetime and intrabeam scattering are not relevant because of the large beam emittances.

The one collective issue that may be significant in the pre-damping ring is the positron-electron instability, referred to as the "Ohmi Effect." This may be partially ameliorated by using an ante-chamber to absorb most of the radiation and by covering the inside of the vacuum chamber with titanium nitride or similar coating. In the future, we will verify the importance of the other effects and, hopefully, will have additional data with which to evaluate the "Ohmi Effect."

4.5 RF Systems

There are four distinct rf systems in the damping ring complex: the S-band and L-band energy compressors, and the pre-damping ring and main damping ring rf systems. As discussed in Section 4.2.9, the ring rf systems will be based

on 714-MHz cavities with HOM damping. The present design is based on the PEP-II cavity design but there are many laboratories around the world working on rf cavities with damped HOMs and we will gain from their experience.

In the pre-damping ring, the total rf voltage is 2.0 MV which leads to an energy bucket of $\pm 1.5\%$. Although this is not sufficient to capture the full $\pm 2\%$ energy spread, the L-band energy compressor will reduce the incoming energy spread by at least a factor of two (Section 4.3.3). The injection line rf systems are based on the electron and positron source linac rf systems while, as stated, the damping ring rf systems are based on the PEP-II rf systems.

In the next sections, we will describe the rf systems for the main damping rings and then the pre-damping ring. Next, we discuss the low-level rf control system for the main damping ring. The low-level rf controls are extreme important in these damping rings because of the high beam-loading and very tight stability tolerances on the extracted bunches. To achieve the stability, the low-level rf system requires many layers of feedback but, as has been realized in the SLC damping rings, it is extremely important to understand the interactions between these feedback loops. This is described in Section 4.5.3. Finally, we will outline the energy compressor rf systems; these systems are described in greater detail in Chapter 6.

4.5.1 Main Damping Rings RF Systems

The rf systems of the NLC main damping rings have to provide sufficient voltage to the beam to compensate for losses due to synchrotron radiation (from the dipole magnets and from the wigglers), losses into higher-order modes (HOMs) of the rf cavities, and parasitic losses to vacuum chamber components. The large synchrotron radiation losses, HOM, and parasitic losses result in an rf system with a large power throughput to the beam. The beam current in the cavity is a factor of 11 greater than the generator current needed to provide the gap voltage.

In addition, the large beam current makes the suppression of HOM impedances more important, to avoid uncontrollable coupled-bunch and single-bunch instabilities. Therefore, in addition to providing the required voltage, the systems should present a low-impedance environment to the beam to maximize instability threshold currents, and avoid the necessity for or minimize the power requirements of beam feedback systems.

The frequency of the damping ring rf systems is determined by the bunch spacing in the main linac—the bunches within a train are separated by 1.4 ns—thereby requiring a minimum rf frequency of 714 MHz. Four trains, 90 bunches each, occupy the damping ring at any one time, with 1.57×10^{10} particles per bunch and an average current of 1.2 A.

The accelerating voltage requirement of 1 MV is achievable using conventional copper cavity construction techniques. To alleviate the problems of coupled-bunch instabilities driven by cavity higher-order modes, some type of suppression of the HOMs is required. There are several suitable such monochromatic cavity designs currently being used or designed, which could find application in the NLC damping rings. For example, the ATF cavity being built for KEK uses a cylindrical body, to which end plates are brazed. These plates have nose cone structures and coupling apertures to which the damping waveguides attach, two on each end of the cavity [Sakanaka 1995]. A different design has been developed for DAΦNE, using a bell-shaped cavity structure with a rounded cavity and enlarged beam-pipe apertures to allow modes to propagate past the ends of the cavity. Long tapers connect the cavity to the smaller diameter beam pipe, resulting in a decreased R/Q value for many modes. Damping waveguides are attached to the cavity body, and to the adjacent tapers [Barry 1993].

For this study we choose a cavity based on a design developed for the PEP-II B-factory project. This cavity has a rounded body and reentrant nose cones, providing a large shunt impedance, and three waveguide loads mounted on the cavity body to efficiently suppress the HOMs. Tapers from the cavity nose cone region to the straight section vacuum chamber provide a smooth transition from the scaled PEP-II cavity to the small vacuum chamber, help to minimize the cavity broadband impedance, and also support additional damping waveguides.

Energy	1.98 GeV
Circumference	223 m
RF	714 MHz
Harmonic Number	532
σ_ϵ	0.09%
σ_z	3.9 mm
α	0.000465
$U_{s.r.}$	644 keV/turn
U_{HOMs}	7.5 keV/turn
$U_{parasitic}$	25 keV/turn
V_{RF}	1.0 MV
# Cavities	2
# Klystrons	2
Cavity Wall Dissipation	41.6 kW/cavity
Klystron Power	600 kW/klystron
Shunt Impedance	3.0 MΩ/cavity
Beam Current	1.2 A
Coupling Factor	11
Unloaded Q	25500
Synchronous Phase Angle	42.6°
Optimum Detuning at Full Current	148 kHz
Synchrotron Frequency	5 kHz
Loaded Q	2170
Energy acceptance	$\pm$1.5%

Table 4-20. *Rf system parameters for the NLC main damping rings.*

Other cavity designs are feasible, such as reducing the aperture at the nose cones to the nominal vacuum chamber dimensions, avoiding the use of tapers. This is expected to increase the strength of many HOMs, but the damping waveguides may still provide the required attenuation for these modes and the increase in broadband impedance may be acceptable. A more detailed optimization, including factoring in the cost of different options, will take place in the future.

The main parameters of the NLC damping ring rf systems are listed in Table 4-20. To determine the power requirements of the rf systems, we need to estimate the losses to parasitic modes in the vacuum chamber components. This we have done by scaling from measurements and calculations performed for other, recently designed or built, low-impedance storage rings. As discussed subsequently, the klystron power requirements, two klystrons each rated at 600 kW, appear to be within the capabilities of manufacturers at this frequency.

In addition, transients in the rf system excited by the gaps in the circulating beam and by injection timing mismatches cause a shift in synchronous phase and timing errors along the bunch train. These transients may be suppressed by the use of feedback systems around the rf klystrons and cavities. The required low-level rf system is described in Section 4.5.3.

Cavity Design

The determination of the number of cavities required involves a compromise between their power-handling capabilities and the beam impedance presented by the cavities. Power-handling capabilities of the rf window and coupler, and the

problems of heat dissipation in the cavity walls and apertures are the limitation to the power into each cavity. These problems have been extensively studied for the PEP-II B-factory rf systems, and we choose to follow their lead and use a cavity design based on the PEP-II B-factory cavities.

The basic cavity shape is a reentrant structure with nose cones, similar to the cavities currently used at the KEK Photon Factory, Daresbury SRS, and the ALS at Berkeley. A conventional copper construction is used, with aperture coupling to the feeder waveguide. Re-entrant nose cones are used to optimize the shunt impedance of the fundamental mode. We scale the dimensions of the PEP-II cavities to achieve a resonant frequency of approximately 714 MHz, with a beam-pipe aperture of 6.2-cm diameter at the nose cones. As discussed in Section 4.4.1, the large aperture at the nose cones reduces the broadband impedance of the cavity and is clearly advantageous. To mate the cavity to the adjacent beam pipe, we use long tapers, while maintaining a total cavity length (including tapers) of less than 0.5 m.

Figure 4-58 shows a half section of the cavity model illustrating the coax damping waveguides on the taper but not showing the damping waveguides on the cavity. Calculations with the electromagnetic design code URMEL give a shunt impedance of $R_s = 4.35\mathrm{M}\,\Omega, Q_0 = 36000$. For the B-factory cavities the addition of the damping waveguides reduced the shunt impedance and unloaded Q value by 30% (compared to the URMEL values). Using the same scaling, we calculate a shunt impedance of $R_s = 3.0\mathrm{M}\,\Omega$, $Q_o = 25500$, and $R/Q = 120\,\Omega$ for the NLC damping-ring rf systems.

The total loss parameter for each cavity is computed by ABCI to be $k_{\mathrm{total}} = 1.75\,\mathrm{V}/pC$ for a bunch length of 4.0 mm, of which the fundamental mode contributes 0.27 V/pC, giving the contribution from higher-order modes $k_{\mathrm{HOMs}} = 1.48\,\mathrm{V}/pC$ per cavity.

Three waveguides are attached to the cavity body to damp the higher-order modes. These waveguides are dimensioned to have a cut-off frequency above the frequency of the accelerating mode of the cavity, but below the frequency of the lowest HOM. Thus the power in HOMs may couple through the apertures in the cavity wall to the waveguides, where it is absorbed in a cooled lossy dielectric material. The location of these waveguides is at 30° from the center of the radius of the cavity body, this position being optimized to couple to the strongest HOMs in the cavity [Rimmer 1992]. The waveguides are located equidistantly in azimuth. The location of the lossy material within the waveguide is at a sufficient distance from the cavity aperture to exclude dissipation of the fundamental mode power from evanescent fields in the waveguide. Experience with the PEP-II cavities shows that Q values of HOMs are damped by two orders of magnitude in most cases, and three orders for targeted modes [Rimmer 1992].

Many higher-frequency cavity modes will spread into the tapers, where the delocalizing effect generally decreases their impedance through a reduction in the transit time factor. These modes may be further damped by locating additional damping waveguides on the tapers. There are many modes at relatively high frequencies, capable of driving within-bunch instabilities which are difficult to combat with feedback systems. Effective broadband damping eliminates these problematic modes. At this time, we are performing 2- and 3-D MAFIA studies of the cavity to optimize the placement of the waveguide on the taper and those on the cavity body.

The PEP-II cavities are designed for a maximum power dissipation of 150 kW. To maintain the same power per unit area in the damping ring cavities, we scale by the frequency ratio of the two rings' rf systems squared to obtain 67 kW per cavity maximum power dissipation in the NLC damping rings cavities. De-rating by 30% gives a conservative dissipation goal of 47 kW per cavity or less.

Higher-Order Mode and Parasitic Losses

Cavity HOM losses are determined from the loss parameter k_{HOMs} and the charge per bunch q; U_{HOMs} is the loss per turn to the cavity HOMs

$$U_{\mathrm{HOMs}} = k_{\mathrm{HOMs}} q \tag{4.52}$$

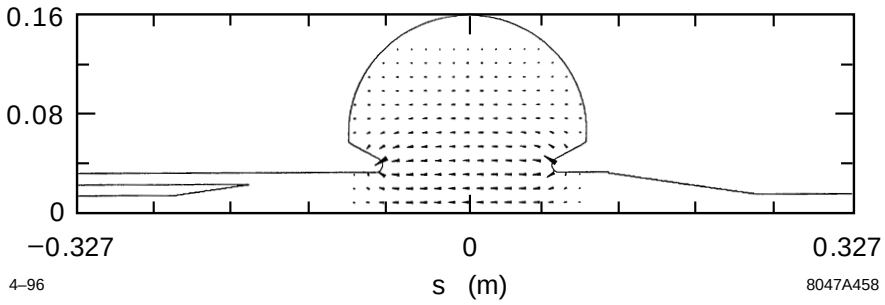

Figure 4-58. *Half section of the rf cavity, without cavity damping waveguides.*

giving $U_{\mathrm{HOMs}} = 3.7$ keV per cavity per turn.

We scale from measurements and calculations of other machines, parasitic losses to vacuum chamber components other than the rf cavities, such as bellows shields, BPMs, kicker magnets, and resistive wall, With careful attention to the design of components, using sophisticated electromagnetic design codes and careful measurements, the parasitic losses can be minimized in modern machines. We choose PEP-II and the ALS as examples of clean, low-impedance machines from which to obtain an estimate of the loss parameter for the NLC damping rings.

For the PEP-II B-factory, the total loss parameter for vacuum chamber components excluding the rf cavities has been estimated to be 6 V/pC, for a bunch length of 10 mm [PEP-II 1993]. Scaling the loss parameter with bunch length as k$\sim \rho^{-1.5}$, with machine circumference as 220/2200, and with the ratio of the vacuum chamber diameters as 6.2/2.8, gives $\mathrm{k_{parasitic}} = 6.9\,\mathrm{V/pC}$.

The ALS is a very similar machine to the NLC damping rings, in that the circumference and the bunch length are almost identical in the two machines. The vacuum chamber radius in the ALS is larger than in the NLC damping rings. Measurements of the ALS vacuum chamber components indicate a loss parameter of approximately 5.8 V/pC (excluding cavities) [Corlett 1993]. Scaling to the NLC damping ring vacuum chamber radius, we estimate $\mathrm{k_{parasitic}} = 15\,\mathrm{V}/pC$. Finally, the calculations in Section 4.4.1 give a $\mathrm{k_{parasitic}} = 5\,\mathrm{V}/pC$. Assuming a value of 10 V/pC, yields losses of $\mathrm{U_{parasitic}} = 25$ keV per turn. Of course, it should be noted that the parasitic losses are very small compared to the synchrotron radiation losses and thus the design is insensitive to the exact value.

Voltage Requirements

The voltage required to compensate for the synchrotron radiation loss, due to both dipole bend magnets and the wigglers, is $\mathrm{U_{SR}} = 644$ keV per turn. In addition, the vacuum chamber parasitic losses are $\mathrm{U_{parasitic}} = 25$ keV per turn, and the rf cavity HOM losses $\mathrm{U_{HOMs}} = 3.7$ keV per turn per cavity. For two rf cavities, the total loss per turn is 677 keV. In order to provide an energy acceptance of $\pm 1\%$, the cavity voltage must be at least $\mathrm{V_{rf}} = 0.85$ MV. To provide some contingency for additional energy acceptance and bunch length control, we take the cavity voltage requirement to be $\mathrm{V_{rf}} = 1.0$ MV.

Power Requirements

The cavity power dissipation is given by

$$\mathrm{P_c} = \frac{\mathrm{V_{RF}^2}}{2\mathrm{R_s}} \tag{4.53}$$

and each cavity dissipates 41.6 kW, based on two cavities, giving a total $\mathrm{P_c} = 83$ kW. This is within the estimated power-handling capability of 47 kW per cavity.

The power delivered to the beam is determined from the synchrotron radiation, HOM losses, and parasitic losses is

$$P_b = I_o(U_{\mathrm{SR}} + U_{\mathrm{HOMs}} + U_{\mathrm{parasitic}}) = I_o U_{\mathrm{losses}} \tag{4.54}$$

where $U_{\mathrm{losses}} = 677$ keV per turn, $\mathrm{I_o} = 1.2$ A for an average beam current, and the power to the beam $\mathrm{P_b} = 812$ kW.

The total rf power required $\mathrm{P_{rf}} = \mathrm{P_b} + \mathrm{P_c} = 895$ kW. Feeding each cavity independently would require two klystrons rated at least 450 kW. Providing a 20% overhead for rf feedback, and 10% for losses in transmission to the cavities, each klystron would be rated at 600 kW.

Coupling Factor and Loaded Q

To be able to obtain the condition of a matched cavity with full beam loading, the cavity coupling factor β_o is determined from

$$\beta_{\mathrm{o}} = \mathrm{I} + \frac{\mathrm{P_b}}{\mathrm{P_c}} \tag{4.55}$$

and we find $\beta_{\mathrm{o}} = 10.7$. The loaded quality factor of a cavity is then

$$\mathrm{Q_q} = \frac{\mathrm{Q_o}}{\mathrm{l} + \beta_{\mathrm{o}}} \tag{4.56}$$

and Q_l = 2170. The filling time $2Q_l/\omega = 0.97$ μs. The synchronous phase angle ϕ_{s} is determined from the total loss per turn U_{losses} and the rf voltage

$$\sin\phi_s = \frac{U_{\mathrm{losses}}}{\mathrm{V_{rf}}} \tag{4.57}$$

which gives ϕ_{s} = 42.6°. The optimum cavity detuning frequency $\delta\mathrm{f}$ is determined from

$$\delta_{\mathrm{f}} = \frac{\mathrm{f_{rf}}}{2\mathrm{Q_0}}\frac{\mathrm{P_b}}{\mathrm{P_c}}\cot\phi\ \mathrm{s} \tag{4.58}$$

where $\delta_{\mathrm{f}} = -148$ kHz, which is small compared to the orbit frequency of 1.36 MHz. Growth times of coupled-bunch modes driven by the accelerating cavity mode are likely to be long.

RF Parameters with Three Cavities

The possibility of using three rf cavities instead of two has been investigated, to reduce the power dissipation in the cavities, the throughput rating of the rf vacuum windows, and the power rating of the klystrons. Table 4-21 lists the parameters changed from the two-cavity case. Klystron power requirements are reduced to 350 kW per klystron, including 20% overhead for feedback systems. Window throughput power is also reduced by 40% to 350 kW. The cavity wall losses are reduced from 42 kW per cavity to less than 20 kW per cavity. Optimal cavity detuning increases to 222 kHz, and the coupling factor is increased to almost 16.

Transient Suppression Using Feedback or Feedforward

The nonuniform bucket population generates transients in the rf system, and the beam sees a nonuniform accelerating voltage. Each bunch in a train has its own individual synchronous phase angle, and the spacing between bunches changes to accommodate this. The use of sub-harmonic cavities, feedback around the rf system, and feedforward in the rf system are being evaluated to reduce the spread in bunches along the rf waveform.

# Cavities	3
U_{HOMs}	11.3 keV/turn
Cavity Wall Dissipation	18.5 kW/cavity
# Klystrons	3
Klystron Power	350 kW/klystron
Coupling Factor	15.7
Synchronous Phase Angle	42.8°
Optimum Detuning at Full Current	222 kHz
Loaded Q	1529

Table 4-21. *Rf system parameters with three cavities.*

Klystrons and accessories

The necessary rf power at 714 MHz will be provided by high-power klystrons. Depending upon the number of cavities and the overhead required for feedback and feedforward, the power could be supplied by three klystrons feeding three cavities, two klystrons feeding two cavities or one super-power klystron driving a pair of cavities. The choice will depend on economic as well as technical considerations. Klystrons exist with up to 1.2-MW CW output in the 350-508-MHz region and power supplies, circulators and loads have been developed to handle this power level. This technology can be readily adapted to the higher frequency and there is already R&D underway in the industry on 1-MW tubes in the 700-MHz frequency range for applications such as tritium production.

There is considerable commercial activity in this frequency range for the television broadcast industry and many mature products exist at the 50-70-kW CW power level. For one- or few-off applications it is possible to combine the output from several of these tubes to produce a higher-power supply such as that used at the SPS at CERN. This station used eight 60-kW TV klystrons (Phillips YK1190 series), producing 450 kW at 800 MHz (newer, higher-power tubes are now available). Given the relatively high volume of production of these transmitter tubes it may be cost-effective to build a high-power source this way with minimal R&D investment.

RF cavity windows

Approximately 600 kW per cavity (into two cavities) will be required to support 1.2 A of beam current at 1 MV total voltage, and overhead (in peak voltage) is required for feedback systems, so the rf window will be a critical component. Both coaxial and disk-type windows routinely operate on high-power klystrons at 1-1.2-MW CW, and cavity windows have been developed for PEP-II and other machines for up to 500 kW throughput. These technologies can be readily scaled to 714 MHz. Additional safety margin could be achieved by supplying the power through two windows per cavity which would provide a very reliable system. Using three cavities per ring would also reduce the power per window significantly.

4.5.2 Pre-Damping Ring RF Systems

The rf systems of the NLC pre-damping rings are based on “monochromatic” cavities as described for the main damping rings in Section 4.5.1. These systems serve to provide sufficient voltage to the beam to compensate for losses due to synchrotron radiation, losses to higher-order modes (HOMs) of the rf cavities, parasitic losses to

vacuum chamber components, and to provide a sufficient rf potential well to capture the injected beam. The resulting accelerating voltage requirement of 2 MV is achievable using four conventional copper cavities.

In order to determine the power requirements of the rf systems, we estimate the losses to parasitic modes in the vacuum chamber components by scaling from the losses estimated for the main damping rings, as described in Section 4.5.1. For the pre-damping ring, with smaller machine circumference and larger beam pipe diameter than the main damping rings, we estimate $\mathrm{k_{parasitic}} = 7$ V/pC.

We choose to use four cavities and two klystrons, with pairs of cavities fed from a single klystron. The klystron power rating of 440 kW appears to be within the capabilities of manufacturers at this frequency.

Table 4-22 lists the main parameters of the NLC pre-damping ring rf systems.

Voltage Requirements

The voltage required to compensate for the synchrotron radiation losses is $\mathrm{U_{s.r.}} = 371$ keV per turn. In addition, the vacuum chamber parasitic losses are $\mathrm{U_{parasitic}} = 17$ keV per turn, and the rf cavity HOM losses $\mathrm{U_{HOMs}} = 3.7$ keV per turn per cavity. For four rf cavities, the total loss per turn is 404 keV.

A larger cavity voltage is required to capture the injected beam, and at a nominal cavity voltage $\mathrm{V_{rf}} = 2.0$ MV, a sufficient energy acceptance of $\pm 1.46\%$ is obtained.

Power Requirements

The cavity power dissipation is given by

$$\mathrm{P_c} = \frac{\mathrm{V_{rf}^2}}{2\mathrm{R_s}} \tag{4.59}$$

and 41.6 kW is dissipated in each cavity, based on 4 cavities, giving a total $\mathrm{P_c} = 167$ kW. This is within the estimated power handling capability of 47 kW per cavity (see Section 4.5.1).

The power delivered to the beam is determined from the synchrotron radiation, HOM losses, and parasitic losses:

$$P_b = I_o(U_{s.r.} + U_{HOMs} + U_{parasitic}) = I_o U_{\mathrm{losses}} \tag{4.60}$$

$U_{\mathrm{losses}} = 404$ keV per turn, and for an average beam current $\mathrm{I_o} = 1.2$ A the power to the beam $\mathrm{P_b} = 485$ kW.

The total rf power required $\mathrm{P_rf} = \mathrm{P_b} + \mathrm{P_c} = 652$ kW. Feeding two cavities from one klystron requires two klystrons rated at 326 kW. Providing approximately 20% overhead for rf feedback, and 10% for losses in transmission to the cavities, each klystron would be rated at 440 kW.

Coupling Factor and Loaded Q

To be able to obtain the condition of a matched cavity with full beam loading, the cavity coupling factor β_o is determined from

$$\beta_o = 1 + \frac{\mathrm{P_b}}{\mathrm{P_c}} \tag{4.61}$$

and we find $\beta_o = 3.9$. The loaded quality factor $Q_l = 5190$, and the filling time $2Q_l/\omega = 2.3\ \mu$s.

Energy	1.98 GeV
Circumference	171 m
RF Frequency	714 MHz
Harmonic Number	408
σ_ϵ	0.0977%
σ_z	7.5 mm
α	0.00511
$U_{s.r.}$	371 keV/turn
U_{HOMs}	16 keV/turn
$U_{parasitic}$	17 keV/turn
V_{rf}	2.0 MV
# Cavities	4
# Klystrons	2
Cavity Wall Dissipation	42 kW/cavity
Klystron Power	440 kW/klystron
Shunt Impedance	3.0 MΩ/cavity
Beam Current	1.2 A
Coupling Factor	3.9
Unloaded Q	25500
Synchronous Phase Angle	11.7°
Optimum Detuning at Full Current	197 kHz
Synchrotron Frequency	31.5 kHz
Loaded Q	5190
Energy acceptance	$\pm$1.46%

Table 4-22. *Rf system parameters for the NLC pre-damping ring.*

The synchronous phase angle ϕ_s is determined from the total loss per turn U_{losses} and the rf voltage

$$\sin\phi_s = \frac{U_{losses}}{V_{rf}} \tag{4.62}$$

which gives $\phi_s = 11.7°$. The optimum cavity detuning frequency δf is determined from

$$\delta f = \frac{f_{rf}}{2Q_o}\frac{P_b}{P_c}\cot\phi_s \tag{4.63}$$

$\delta f = -197$ kHz, which is small compared to the orbit frequency of 1.75 MHz, therefore growth times of coupled-bunch modes driven by the impedance of the accelerating cavity mode are likely to be long.

4.5.3 Low-Level RF Systems

The low-level system includes various regulating feedback loops, controls, and protection interlocks. Most of these constituents are common to other storage ring and damping ring rf systems and therefore pose no unusual design challenges. The design goal is to ensure ease in diagnosis of rf-related problems while minimizing the complexity of the rf system: anticipated error sources are corrected for locally and regulation of each klystron-beam-cavity interaction is independently maintained. The function of the low-level rf system is

- to regulate the cavity voltage and beam phase, and
- to minimize the effects of transient beam loading caused by injection and extraction.

Cavity voltage and beam phase regulation is maintained by passive feedback while transient loading in the cavities will be minimized using feedforward at injection. Similar beam-loading compensation techniques will be tested and used at PEP-II [PEP-II 1993] and the KEK Accelerator Test Facility (ATF) damping ring [ATF 1995]. The feedforward algorithm, which is discussed in detail below, also allows beam injection at a high duty cycle.

The stability of the rf system and the particle beam in the main damping rings has been studied using a numerical model of the beam-cavity interaction with multiple feedback loops. The study has yet to be applied to the positron pre-damping ring, however, the low-level rf system designs are expected to be quite similar. Unique to the NLC damping rings are the high beam currents (about a factor of 10 increase compared to the SLC). Analyses of transient loading at injection have therefore been performed. The simulations will be extended to study synchronous phase transients due to the gaps between bunch trains, which are discussed in Section 4.4.4.

Low-Level Controls

A block diagram of the low-level control system is shown in Figure 4-59. The rf from the main NLC oscillator is phase-shifted using feedback from the interaction point (IP) collision time (as determined by the arrival time of e^+ in one linac and the e^- in the other). This global phasing of the front end (source, injector linac, etc.) is required since the single-turn injection/extraction scheme, which minimizes beam phase and bunch length variations in steady-state operation of the damping rings, disallows independent phasing of beam phase at injection to and extraction from the damping rings. The phase-shifted rf from the main oscillator is frequency-divided to 714 MHz, amplified as necessary, and used as the phase reference for the damping ring rf system. A separate voltage-controlled oscillator (VCO) is provided to allow the ring frequency to be varied (for measurement of the chromaticity, for example).

Beam Phase Loop. Deviations in damping ring timing are corrected using a phase feedback loop which uses the beam phase measured with a damping ring BPM and adjusts the phases of the source, prelinac, and damping ring. The bandwidth of this loop is limited by the minimum frequency for coherent synchrotron oscillations ($\approx$2 kHz at full current).

Referring to Figure 4-59, a common local oscillator provides rf input to the two klystrons. Each klystron powers a one single-cell cavity with higher-order mode damping for coupled-bunch modes. A circulator upstream of each cavity isolates the klystron from reflected power arising from cavity detuning or the sudden absence of beam. Additional protection is provided by an rf switch upstream of each klystron which is activated by standard protection interlocks. There are slow interlocks including those for cavity vacuum and for water flow and temperatures in the klystrons, cavities, and circulator loads. Fast interlocks protect against reflected power faults and arcs in the klystrons and circulators.

Five feedback loops are used to stabilize the beam and accelerator. These include loops to regulate the klystron output, the cavity resonant frequency, and the cavity phase and amplitude. In the heavily beam-loaded limit, the cavity amplitude and phase loops should ideally correct for beam-induced transients. Using feedforward, however, because the phasor voltage of the cavity is maintained independent of the beam current or the change in beam current, the gain requirements of these loops is significantly reduced. The precise gain and bandwidth requirements in the feedback design have yet to be determined.

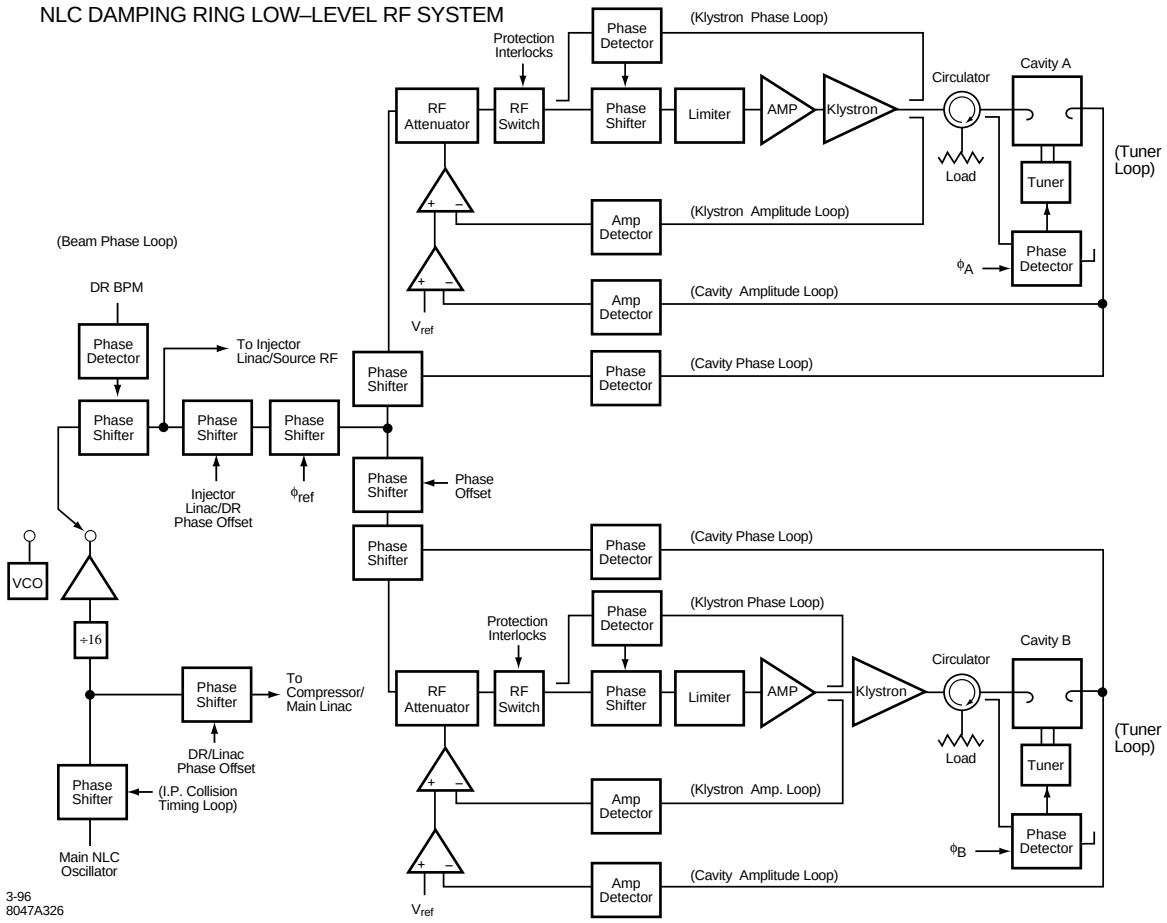

Figure 4-59. *Block diagram of the low-level control system for the NLC damping rings.*

Klystron Amplitude and Phase Loops. Slow, high gain feedback loops are used to correct for klystron high-voltage power supply ripple and other sources of phase or amplitude error. The input to both loops is a measure of the klystron forward power. The phase of this signal is compared with the input rf phase and the difference is used to shift the phase of the input rf. In the klystron amplitude loop, the rf signal is converted to DC with an amplitude detector. The difference in this amplitude from the error signal of the cavity amplitude feedback is used to adjust an rf attenuator upstream of the klystron.

Cavity Amplitude Loops. To regulate against slow changes in the cavity voltage, due to long-term thermal variations for example, the amplitude of each cavity is maintained at an externally specified level, $V_{\rm ref}$. The error signal is used to adjust an rf attenuator upstream of the klystron. The bandwidth is high and limited by the minimum frequency for coherent beam oscillations (≈ 2 kHz at full current).

Cavity Phase Loop. This loop maintains the phase of the net cavity voltage with respect to phase of the input rf by adjustment of an rf phase shifter. The bandwidth is limited to ≈ 2 kHz at full current.

Cavity Tuner Loops. A single loop per cavity is used to correct for thermal variations and reactive loading by the beam. For fast filling of the ring (see below), the tuner positions are fixed at externally specified angles, ϕ_a and ϕ_b, to minimize the reflected power from the cavities when operating at full current. The bandwidth of these loops is limited by the speed of the mechanical plungers ($\approx$1 Hz).

Feedforward Algorithm for Beam Injection

Because of the very high beam currents, beam-induced loading of the cavities at injection is a concern in the damping ring rf system design. Studies have shown that without compensation (either feedforward or direct feedback [Pedersen 1975]), beam-loading of the rf system could result in beam loss and instabilities in the regulation. A feedforward algorithm was devised to correct the injection transients. While the beam-loading limit was not a concern for the steady-state operation of the damping rings, direct feedback was also considered to help damp the transients.

Shown in Figure 4-60 is the parameter space for voltage regulation for the NLC main damping ring. The beam current I_b, which is twice the total DC current, is plotted as a function of the cavity tuning angle ϕ_z, which is the angle between the total current and total cavity voltage and is a measure of how far off resonance the cavity is being driven. The steady-state full current operating point is shown by the circle. The shaded area shows Robinson's region of instability [Robinson 1962] in the high-current limit. (The low current limit corresponds to $\phi_z > 0$.) The dotted curves are contours of constant loading angle, ϕ_l; along the line $\phi_l = 0$ the reflected power is minimized. The solid curve corresponds to a maximum total klystron output power of 1.2 MW. In the steady-state, the cavity voltage will be maintained at the nominal value of 1 MV for operation anywhere within the region bounded by the klystron power curve and the lower right quadrant of Figure 4-60. Operation outside this region results in loss of regulation of the cavity voltage, due to insufficient klystron power, and eventually beam loss. Transient loading or klystron nonlinearities may reduce the stable operating region. The klystrons are specified to deliver a maximum of 1.2-MW peak power to ensure linearity of the klystron response.

There are two possible schemes for injecting to full current. To minimize the total reflected power in the injection process, the tuning angle ϕ_z could be preset just before each train is injected such that $\phi_l = 0$ after the train is injected. This corresponds to moving along the $\phi_l = 0$ line in Figure 4-60. However, this scheme is time consuming since it is limited by the slow motion of the tuners. A faster scheme involves one preset of the tuners to ${\phi_z}^*$, when the beam is absent, followed by consecutive injection of all 4 trains. While the reflected power is not insignificant during initial detuning without beam, it is within the specifications of the circulators. In the interest of maintaining a high duty cycle and allowing for maximum flexibility and compatibility to the remainder of the accelerator, the fast injection scheme has been developed. (However this does not preclude the alternative.)

Two techniques for correcting for the beam-induced transients at injection have been studied. Based on recent experiences and success at the SLC, the use of direct feedback was considered first. While it is possible to inject all the trains, there are a number of disadvantages introduced by the loop:

- The required gain places a tight tolerance on the total delay (less than 210 ns for an open loop gain of 2.5) and hence on the delay time in the klystron.
- The required gain introduces coupled-bunch modes that are supported by the cavity.
- Because the transient is corrected $after$ it is detected, residual cavity voltage and phase oscillations still persist.

The second technique is based on pre-conditioning the cavity phase and amplitude based on knowledge of the incoming charge. Using this feedforward algorithm, the total cavity current and voltage as well as the phase angle between them are held constant during the injection process. The process is depicted using phasors in Figure 4-61. Here V_c is the total cavity voltage (which is the vector sum of the generator and beam voltages), I_c is the total cavity current, ${I_b}^{(k)}$

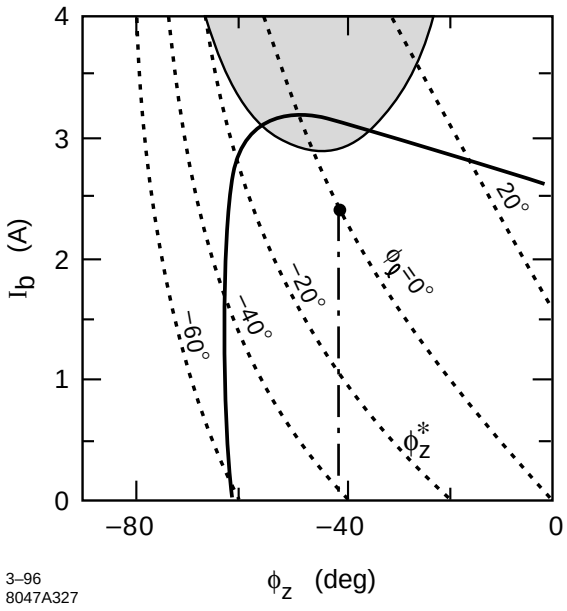

Figure 4-60. *Parameter space for voltage regulation for the main damping ring with 1.2 MW rf power. Here, the beam current $I_b = 2I_{dc}$ is plotted versus the tuning angle ϕ_z. The shaded region is that limited by Robinson instability and the dotted lines are contours of constant loading angle. The nominal operating point is shown at $\phi_l = 0$.*

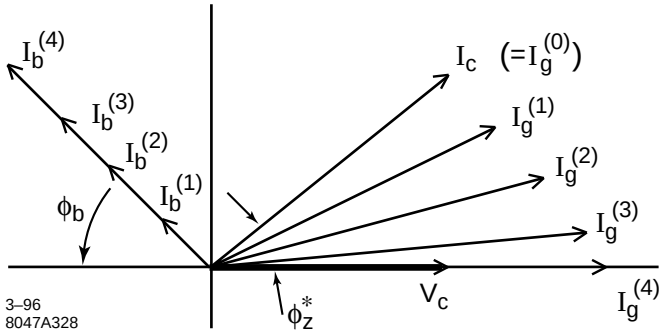

Figure 4-61. *Feedforward algorithm illustrated using phasors.*

and $I_g{}^{(k)}$ are respectively the beam and generator currents for train k, ϕ_b is the synchronous phase angle measured with respect to the crest, and $\phi_z{}^*$ is the cavity tuning angle for which the loading angle is zero at full current.

The principle of the injection procedure, using feedforward, is as follows (for the case of a zero-to-full-current ramp):

1. With beam off, deactivate tuner loops and detune for $\phi_l = 0$ at maximum current; that is, set the tuner position to $\phi_z{}^*$.
2. Set the external references (see Figure 4-59) $V_{\rm ref} = SI_g$ for the desired cavity voltage, where S is the transconductance of the klystron, and $\phi_{\rm ref} = \phi_z{}^*$.
3. Inject train 1.

4. Increment $V_{\rm ref}$ by $\Delta V_{\rm ref} = S\Delta I_g$ and $\phi_{\rm ref}$ by $\Delta\phi_{\rm ref}$ and inject train 2.
5. Repeat step 4 until all trains have been injected.
6. Reactivate tuner loops.

This procedure can be executed at maximum duty cycle so that the total time for injection is 4 cycles, or 22.2 ms at 180 Hz. Similar procedures are used for initial turn on with low beam currents or with low repetition frequencies. These are described in the section on the machine protection system (MPS) in Chapter 16.

The required changes in the reference voltage and reference phase are:

$$\Delta I_g = \frac{V_c/R + {I_b}^k \cos {\phi_b}^k}{\cos {\phi_b}^k} - \frac{V_c/R + {I_b}^{k+1} \cos {\phi_b}^{k+1}}{\cos {\phi_b}^{k+1}} \quad , \tag{4.64}$$

and

$$\Delta\phi = \tan^{-1}\left[\frac{\tan {\phi_z}^* + \frac{{I_b}^k R}{V_c} \sin {\phi_b}^k}{1 + \frac{{I_b}^k R}{V_c} \cos {\phi_b}^k}\right] - \tan^{-1}\left[\frac{\tan {\phi_z}^* + \frac{{I_b}^{k+1} R}{V_c} \sin {\phi_b}^{k+1}}{1 + \frac{{I_b}^{k+1} R}{V_c} \cos {\phi_b}^{k+1}}\right] \tag{4.65}$$

A potential systematic error associated with feedforward is that the cavity voltage will be regulated to the specified value, $V_{\rm ref}$; if the incoming charge is of different current than anticipated, then the amplitude feedback loop would regulate to an incorrect voltage.

Simulations of Low-Level rf System

Numerical simulations of the low-level rf system were performed by modifying existing software used in SLC rf system analysis [Minty 1995b]. In the simulations, the parameters of Table 4-20 are used. The model includes two (linear) klystrons, two rf cavities, and various feedback loops which include realistic nonlinear elements such as time delays and filters. At present, the cavity is modeled as a narrow-band resonator so that only beam interactions with the fundamental cavity mode are analyzed. Synchrotron radiation damping has not been taken into account.

The simulated response of the cavity voltage and beam phase to the injection of the first train is shown in Figure 4-62 for three cases: no transient loading compensation (solid), correction with direct feedback using a loop gain of 2.5, and correct phasing of the loop to minimize the transients (dot-dashed), and correction with feedforward (dashed). The results are summarized in Figure 4-63, in which the peak-to-peak cavity voltage and phase oscillations are plotted as a function of train number using direct feedback (a) or using feedforward (b). As can be seen, the correction of the beam-transients is substantially improved with the feedforward algorithm.

Figure 4-64 shows simulation results for the injection procedure outlined above for a zero to full current ramp. The feedforward references, as calculated from Eqs. 4.64 and 4.65, are also shown, along with the required generator and reflected powers. Notice that the Robinson damping time is shorter for the higher the current; this arises because of the fixed tuning angle. Also worth noting is the decrease in the coherent synchrotron oscillation frequency with current; as the beam current is increased the phase of the beam with respect to the generator crest becomes smaller resulting in a reduced restoring force for coherent phase perturbations. This effect must be taken into account in the feedback loop designs. Further analysis of stability tolerances imposed by the feedforward algorithm are in progress.

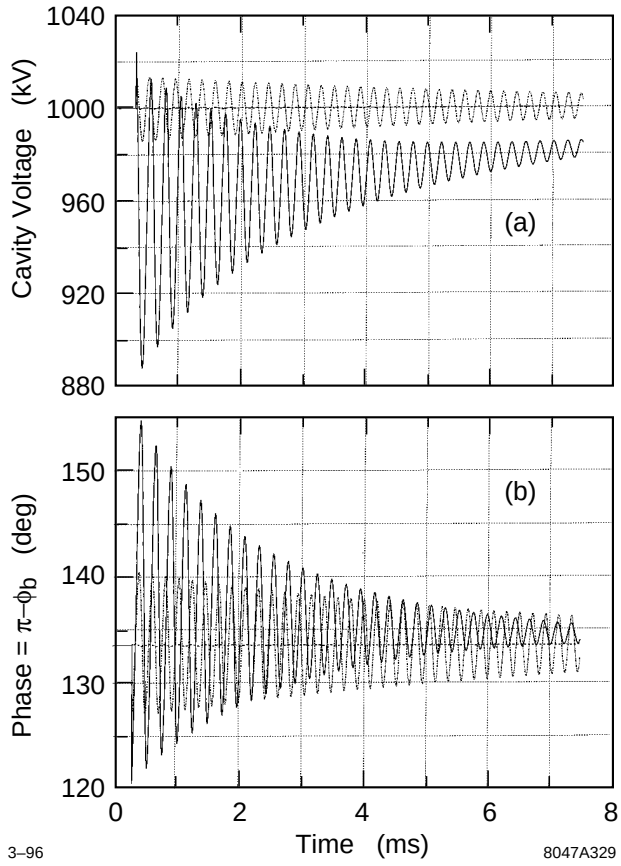

Figure 4-62. *Simulations of injection transients in the cavity voltage (a) and beam phase (b) at injection of the first train. The largest oscillations arise without feedback or feedforward; the direct rf feedback reduces the amplitude of both the voltage and phase oscillations but reduces the damping of the oscillations; the feedforward system reduces the oscillations to essentially zero.*

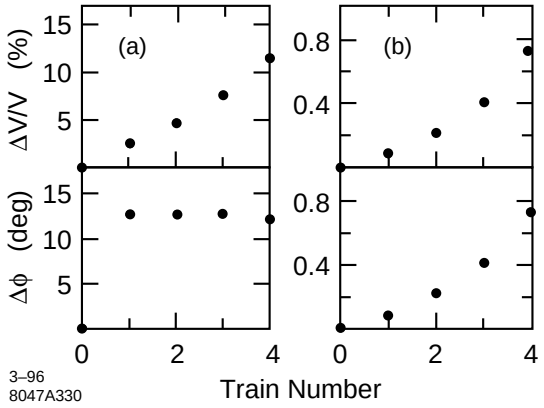

Figure 4-63. *Simulated peak-to-peak cavity voltage and phase oscillations as a function of train number. The transients are corrected either with direct feedback (a) or feedforward (b).*

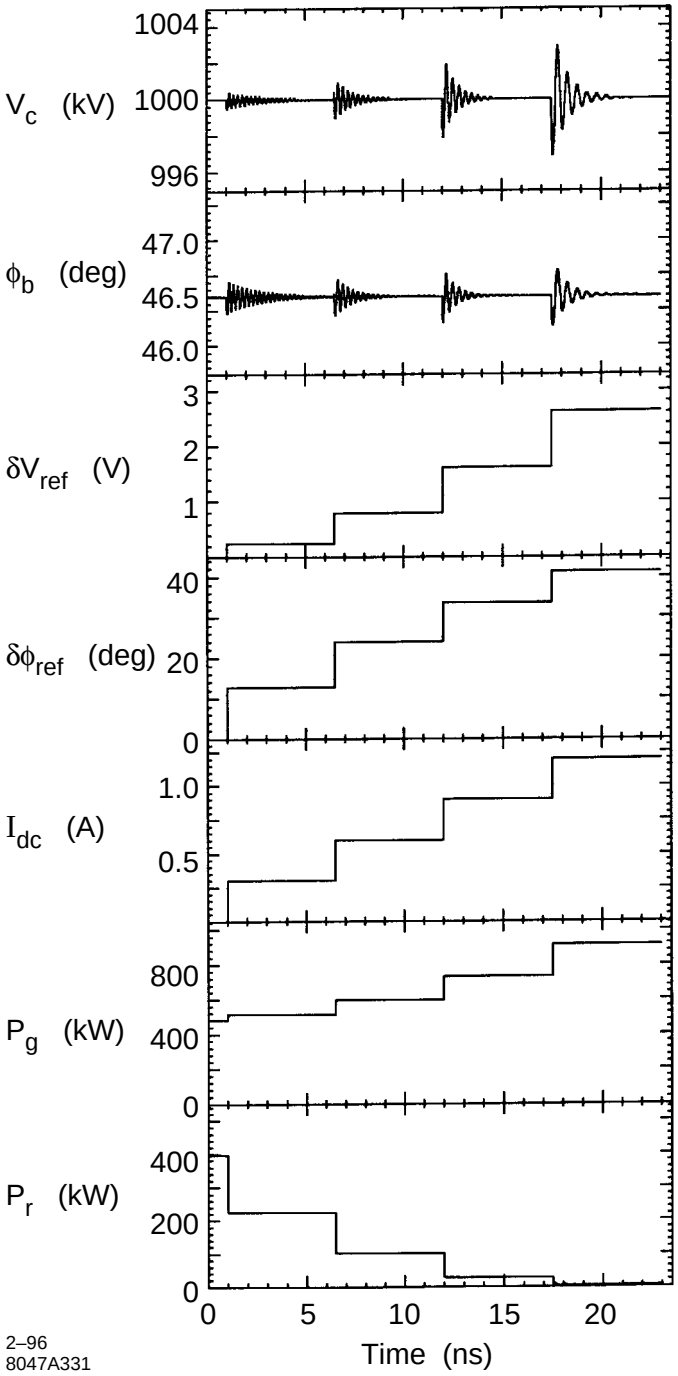

Figure 4-64. *Simulated current ramp from no beam to full current. Plotted are the cavity voltage V_c [kV], the beam phase ϕ_b [deg], the change in reference voltage $V_{\rm ref}$ [V], the change in reference phase $\phi_{\rm ref}$ [deg], the DC beam current I_b [A], the generator power P_g [kW], and the reflected power P_r [kW].*

	Electron	Positron
f_{rf} (MHz)	2856	1428
V_{rf} (MV)	42	80
L_{rf} (m)	2.5	4
Gradient (MV/m)	21	20
Structure Type	DDS	Detuned
Multibunch loading Comp.	ΔT	ΔT

Table 4-23. *Parameters of the rf systems for the electron and positron energy compressors.*

4.5.4 Energy Compressors

The electron and positron injection lines include rf sections that are used to reduce the incoming beam energy spread and energy jitter. Parameters of the energy compressors are given in Section 4.3.3. The electron compressor uses an S-band rf system while the positron system uses an L-band system; the L-band rf system is needed for the positron line because the beam emittance and beam size are too large for the apertures in the S-band structures.

The structures are shortened versions of those used in the electron and positron source linacs and are described in Chapter 6. The parameters for the injection line rf structures are listed in Table 4-23. In both cases, S-band and L-band, we use the ΔT (early injection) multibunch beam-loading compensation technique described in Chapter 6. This is the preferred method since it does not require additional off-frequency structures or klystrons. The technique can compensate for the full range of beam current by adjusting the klystron output.

4.6 Vacuum Systems

4.6.1 Main Damping Ring

The main damping ring vacuum system has been designed to attain a vacuum pressure less than 10^{-9} Torr. Because of the small vacuum chamber aperture and the large amount of synchrotron radiation, attaining such a pressure by simply pumping the beam chamber is unreasonable. Just to to attain a pressure of 10^{-8} Torr in the arcs without an ante-chamber would require placing a 400 L/s pump every 20 cm.

For these reasons, the arc and wiggler vacuum chambers have ante-chambers where the pumping is performed. At this time, we have a fairly advanced design for the arc chamber—this has allowed us to make accurate estimates of the ring impedance—and are working on the design of wiggler vacuum system.

Arcs

The NLC arc vacuum chamber is patterned after the Advanced Light Source (ALS) vacuum system. The vacuum chamber in each 4-m-arc cell will be constructed from two chamber sections and connected with a single bellows to the next arc cell chamber. The chambers will be machined in two halves from aluminum and then welded. Constructing

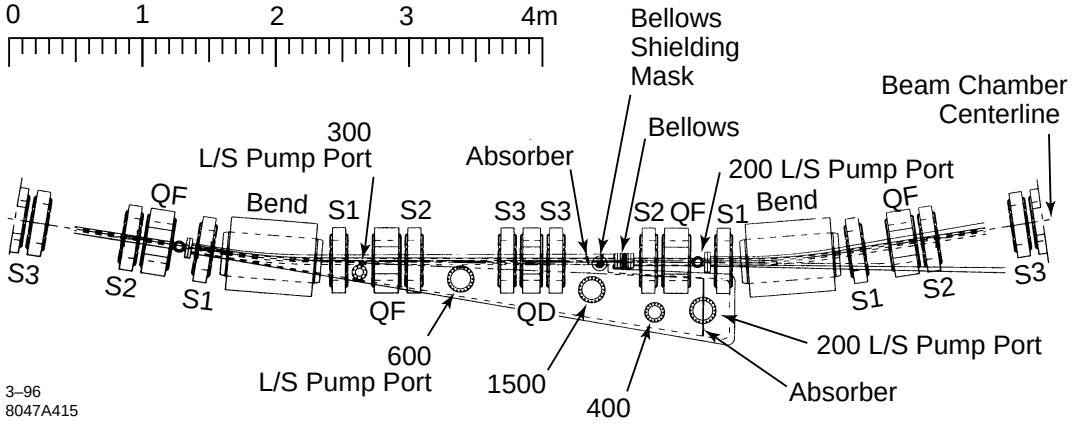

Figure 4-65. *Arc vacuum chamber in the NLC main damping ring.*

the chamber from machined-aluminum rather than extrusions readily allows for complicated shapes while maintaining very high construction tolerances.

The arc beam chamber is circular with a 12.5-mm radius and a 5-mm-high slot that couples it to an ante-chamber. Because of the small chamber radius, the 5-mm slot subtends a relatively large angle and allows 99.8% of the synchrotron radiation power to escape the beam chamber. This is actually a greater percentage of the radiation than escapes the ALS vacuum chamber which uses a 1-cm slot. Of course, because of the smaller dimensions, the alignment and construction tolerances will be tighter than those on the ALS chambers.

The chamber of a single arc section is illustrated in Figure 4-65 and a cross-section of the vacuum chamber inside a quadrupole magnet is shown in Figure 4-66. The chamber will be machined to accommodate the magnet poles and the arc magnets are designed as "C" magnets, allowing the ante-chamber to exit the sides of the magnets. The minimum wall thickness is 2.5 mm at the quadrupole poles, leaving 0.5 mm between the chamber and the magnet poles for alignment purposes. In the magnets, the 5-mm coupling slot is tapered to 8 mm in the ante-chamber and the wall thickness is increased to 11 mm.

The primary photon stop is at the end of the ante-chamber. The ante-chamber is designed with two vertical aperture constrictions to which reduce the flow of desorbed gas from the photon stop to the beam chamber. This allows for differential pumping which greatly reduces the pumping requirements. The vertical cross-section of the chamber in the photon stop region is shown in Figure 4-67.

The design of the beam chamber bellows is illustrated in Figure 4-68. The design is based on the ALS bellows. A smooth rf coupling within the bellows is achieved by maintaining the thin BeCu flex band under tension between either end of the internal plates. Thermal expansion of the beam pipe (1 mm for an 11°C in the 4-m chamber sections) is easily accommodated by fold-over fingers bridging a slot between the end of the flex band and the upstream end flange. During installation, when larger compression is required, the flex band is allowed to bow outward from the beam chamber centerline.

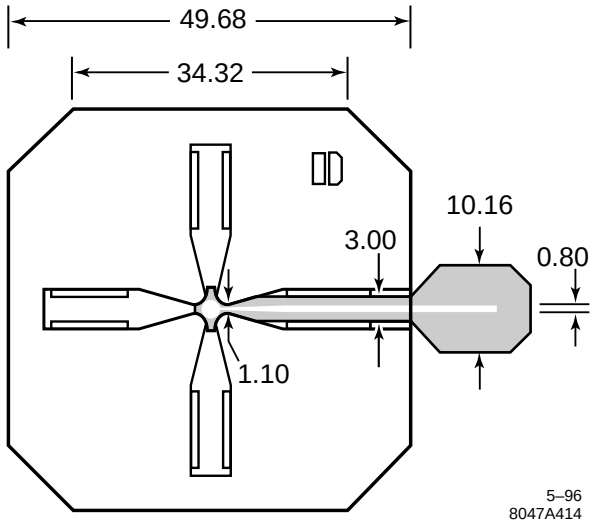

Figure 4-66. *Arc vacuum chamber in a quadrupole magnet.*

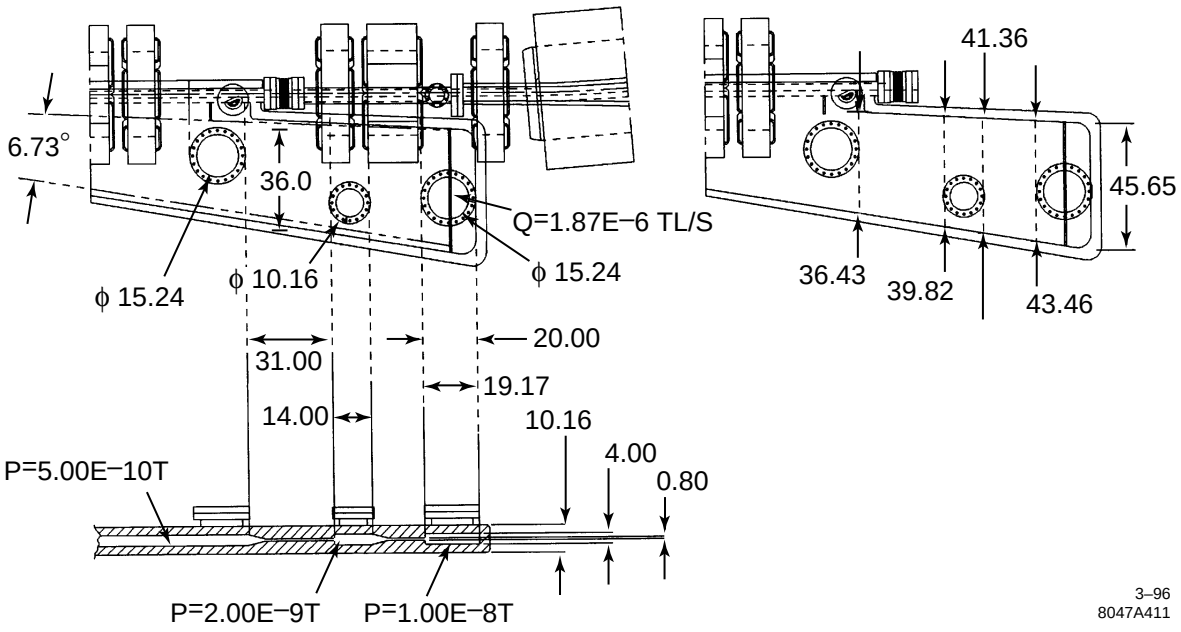

Figure 4-67. *End of arc cell chamber with photon stop and bellows and associated mask. The vertical ante-chamber profile shows aperture constrictions to reduce pumping requirements.*

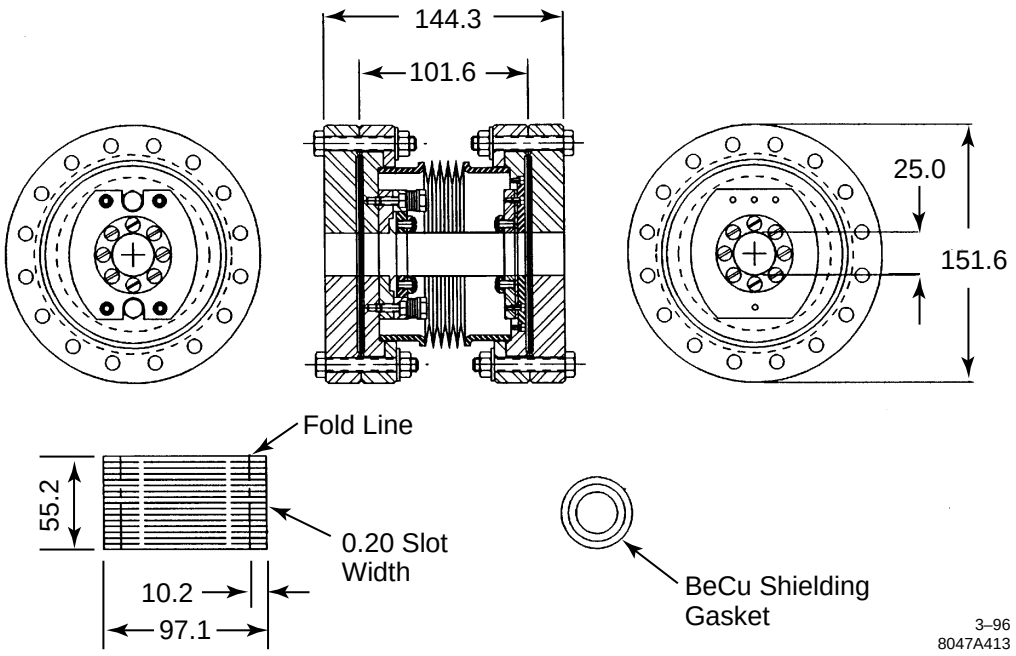

Figure 4-68. *Arc vacuum chamber bellows design.*

The rf liner in the bellows has the same dimensions and profile as the beam chamber, and, to simplify the design, the slot and ante-chamber are terminated just upstream. A mask which extends 2 mm into the beam chamber shields the bellows from the synchrotron radiation. The linear power density on the bellows mask and absorbers is kept just under 100 W/cm, which compares favorably with PEP and PEP-II values. The impedance of the slot termination, mask, and bellows have been calculated using MAFIA and are discussed in Section 4.4.1.

The initial vacuum design was based on NonEvaporable Getter (NEG) vacuum pumps that were supplemented with small ion pumps. Presently, we are considering using titanium sublimation pumps similar to those that are used in the ALS and will be used in the PEP-II Low Energy Ring. Assuming a desorption rate of 2×10^{-6} molecule per photon (thermal desorption is negligible), the total pumping per cell to attain a vacuum pressure of 10^{-9} Torr is 3200 L/s. The pressure profile in the beam chamber is illustrated in Figure 4-69.

Finally, it is anticipated that the arc vacuum system will baked once before installation. At this time, we have not decided if it is necessary to install the capability for *in-situ* baking. Catastrophic vacuum vents are rare. If one does occur, it is likely that the the chamber could be scrubbed using the intense synchrotron radiation from the beams. Of course, while the chamber is being scrubbed, the ring performance would likely be very poor, but the scrubbing should not take very long. This is the procedure that is used in the SLC damping rings and it was also the procedure used in the ALS to recover after the only unplanned vacuum vent experienced thus far.

Wiggler Regions

The wiggler straight section vacuum chamber is approximately 35-m long. It extends inside the arc from one side of the straight section to allow the absorption of the synchrotron radiation from the last wiggler magnets. The vacuum

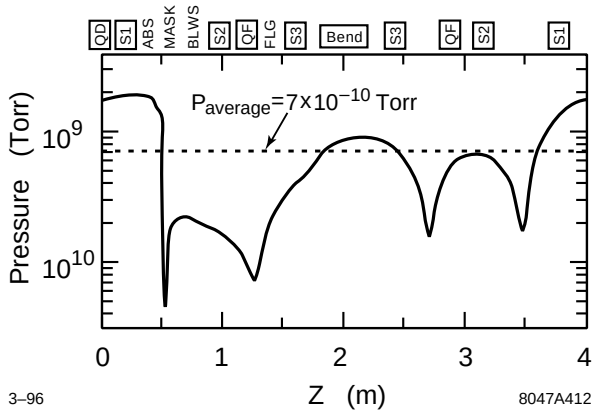

Figure 4-69. *Vacuum pressure in the arc beam chamber.*

chamber is aluminum and is designed to absorb approximately 400 kW of synchrotron radiation power. The cross section of the vacuum chamber together with a cross section of a wiggler magnet and the supporting frame is shown in Figure 4-70. As is seen from the picture, the vacuum chamber has a beam chamber that is roughly 45 mm by 16 mm and an antechamber on either side with a slot height of 10 mm. The antechamber slots are sloped at 0.25 radian angle, forming a water cooled dump to absorb the synchrotron radiation generated by the wiggler magnets. The vacuum pumping is performed by distributed Nonevaporable Getter (NEG) pumps which are located behind the dump surfaces at the end of each slot.

The design of the distributed NEG pumps is a departure from conventional NEG designs and follows the approach adopted for a vacuum chamber of the wiggler straight section of the Low Energy Ring of PEP-II B-Factory [Heim 1995]. Here, an SAES ST707 strip is cut into individual `wafers' using a laser sheet metal cutting machine. The cutting is performed under an argon purge to prevent oxidation. The NEG wafers are then slipped over a 9-mm diameter steel tube which is a combination of vacuum barrier and support rod. Between each wafer there is a 2-mm-thick stainless-steel wire-ring spacer. Each pump contains approximately 11 m of NEG strip per meter of length. This provides a distributed pumping speed of 385 liters per second per meter with a getter capacity of 1.1 Torr-liters per meter. The NEG pump is activated by a commercial tubular heater inserted inside the tube. The heater is outside of the vacuum space and it doesn't require an electrical feed-through. In addition, replacement of a failed heater does not require venting the wiggler vacuum chamber. The stainless steel rf screen separates the dump area from the NEG pumps. The purpose of the screen is to block rf TE modes from propagating down the slots and heating the NEG. The distributed NEG pumps will be supplemented by discrete ion pumps to pump hydrogen during NEG activation and methane during machine operation.

The wiggler vacuum chamber will be fabricated from two aluminum plates. Two pieces make up the top and bottom halves of the chamber. Each plate is machined on the outside first to form the water cooling passages and the magnet pole pockets. After the water cooling passages have been TIG closure welded, the interior aperture and dump surfaces are machined. A second TIG welding operation is required to join the top and bottom plates and to attach an aluminum-to-steel adapters to each end. Finally, the stainless steel end flanges are welded to the adapters.

The chamber will be vacuum baked at 150° for one or two days, then argon gas glow-discharge cleaned and, finally, coated with the layer of the titanium nitride to reduce photoelectron emission.

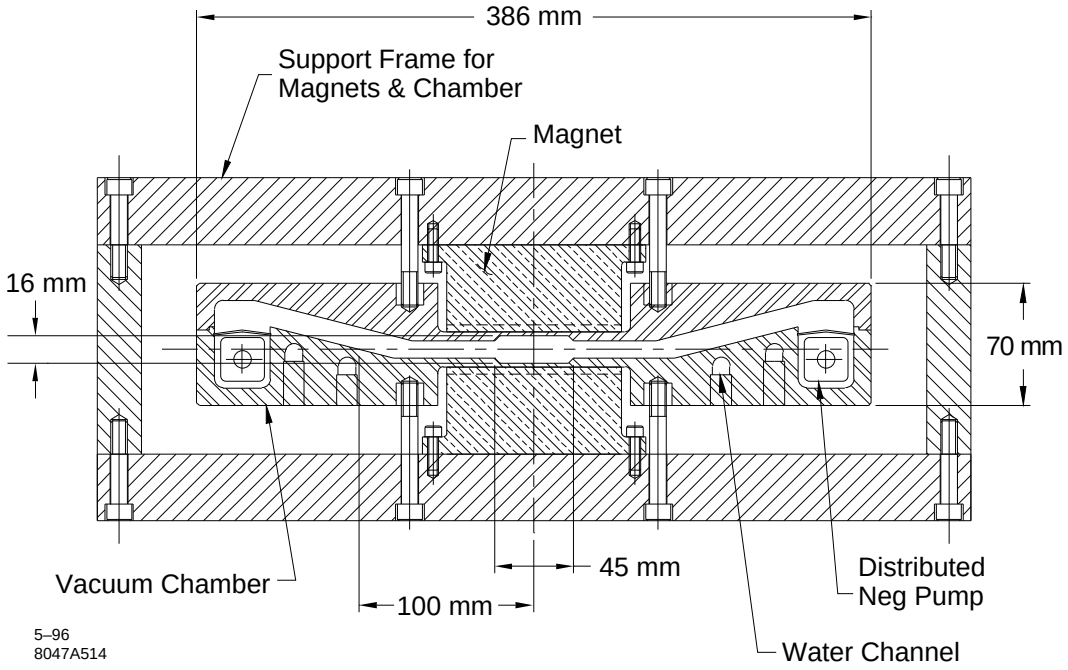

Figure 4-70. *Schematic of the cross section of the wiggler vacuum chamber, the cross section of the wiggler magnet, and the supporting frame.*

Injection/Extraction Region

At this point, we do not have a design for the vacuum system through the injection/extraction region of the main damping ring but we do not expect it to present significant difficulties. In concept, the arc ante-chamber will be terminated after the last matching bend. The circular 1.25-cm-radius beam chamber will continue for roughly 3 m to the rf cavities. In the present design, the aperture is increased before the cavities in a 15-cm taper to a 3.1-cm radius. After the two rf cavities, the chamber would taper back to the 1.25-cm radius to pass through the ceramic chamber of the extraction kicker system. Following the extraction kickers, the chamber would be increased to a 1.6-cm radius and then would become elliptical as the horizontal half width is increased to 2.5 cm to allow for the extracted beam. The chamber will maintain this elliptical profile between the two septa and then taper back down to pass through the injection kickers. Finally, the arc ante-chamber will resume at the matching bend.

Effort will be needed to maintain smooth transitions from one cross-section to the next. We will also need to consider how to minimize the impedance due to the septa which will be mounted in large vacuum canisters. Finally, we will need to design the coated ceramic chambers for the kickers and the numerous pumping ports that will be required to maintain the 1-nTorr vacuum pressure in this conductance-limited system.

4.6.2 Pre-Damping Ring

The vacuum system for the pre-damping ring has not been designed yet but the vacuum requirements are relatively loose; a pressure of 10^{-8} Torr will be sufficient. It has been assumed that the chamber would be constructed from

aluminum like the main damping ring chambers. Of course, since the tolerances are much looser, it would probably be formed by extrusion rather than be machined from aluminum stock.

As noted in Section 4.3.2, the chamber aperture in the arcs must have inner dimensions of 6 cm by 3.6 cm to accommodate the edge emittance of 0.09 m-rad and leave $\pm$2-mm clearance for steering. Although it is not required from the vacuum point of view, an ante-chamber will probably be used though the arcs because it eases the handling of the radiation power. In addition, the ante-chamber would reduce the number of secondary electrons which may cause the positron-electron instability discussed in Section 4.4.7. To further reduce the number of secondary electrons, the aluminum chamber could be coated.

4.6.3 Transport Lines

The vacuum system in the injection, extraction, and transfer lines has not been completed. The system must include valves to isolate the damping rings from the source linacs and the bunch compressors. The vacuum pumping is primarily needed to counter the thermal outgassing. In these sections, the vacuum pressure should be less than 10^{-8} Torr.

4.7 Feedback and Feedforward Systems

The damping rings will require numerous feedback and feedforward systems. Some of the rf feedback systems were described in the section on the low-level rf control, Section 4.5.3. This includes feedback loops around the klystrons and cavities as well as timing feedback loops from the bunch compressors and feedforward loops from the sources. In this section, we describe the transverse coupled bunch feedback systems and some of the transverse feedbacks needed to maintain the beam trajectory. In addition, we will review the requirements on some of the other global feedback and feedforward systems.

4.7.1 Coupled Bunch Transverse Feedbacks

As described in Section 4.4, the transverse coupled-bunch growth rates in the main damping rings require feedback damping. This section describes a bunch-by-bunch feedback for the main rings that is similar to that planned for the PEP-II rings.

The fastest growing coupled-bunch modes in the main damping ring are those driven by the transverse resistive-wall impedance. Because the pre-damping ring vacuum aperture is much larger than that in the main damping rings, the resistive-wall impedance is not expected to be significant and thus a coupled-bunch feedback system will probably not be necessary in the pre-damping ring; this will be verified in the future.

Main Damping Ring Feedback Design

The coupled-bunch growth rates calculated for the main damping rings indicate that a feedback system will be required to maintain stability of transverse beam oscillations. It is expected that the longitudinal oscillations will be stable and will not require a feedback system.

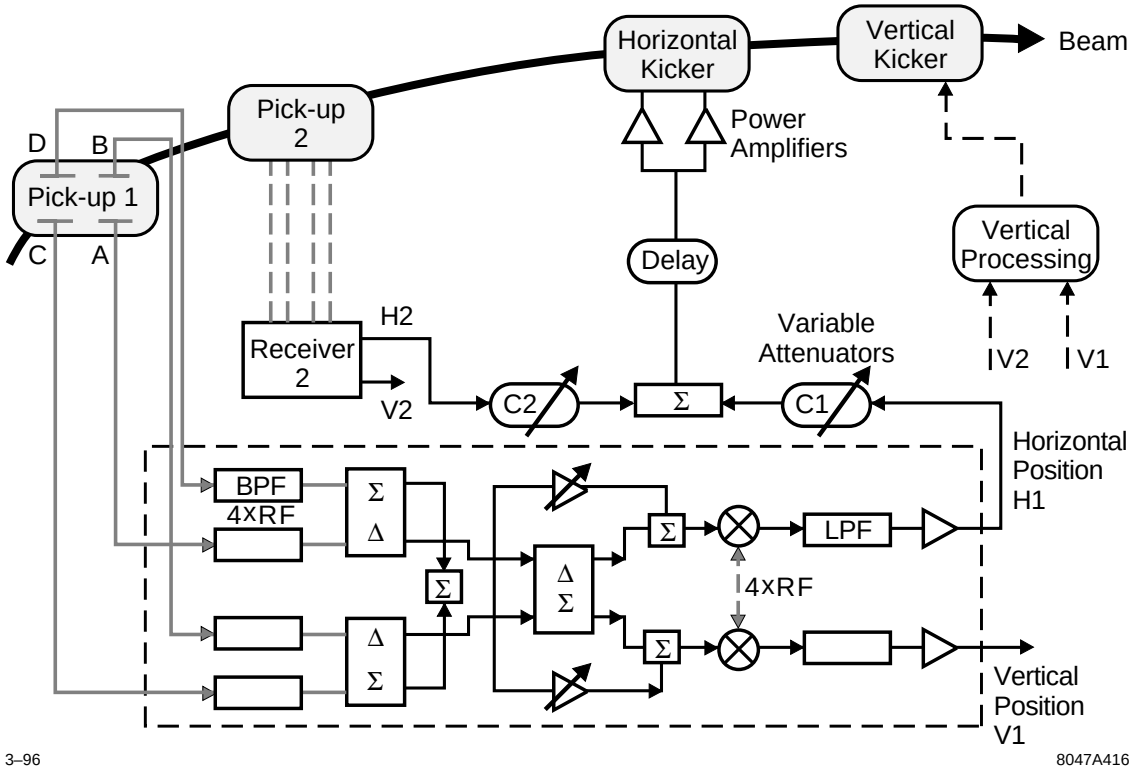

Figure 4-71. *Schematic of the coupled-bunch feedback system.*

As shown in the calculations of coupled-bunch growth rates, the transverse impedance excites a fairly broadband spectrum of beam modes, although the dominant modes are driven by the resistive-wall impedance up to about 50 MHz. We propose a bunch-by-bunch system that acts independently on each bunch, damping all possible coupled–bunch modes. For a bunch spacing of 1.4 ns, this implies that the minimum system bandwidth be at least 357 MHz. This bandwidth requirement poses the most difficult design restrictions on the system.

The transverse feedback system (TFB) can, in principle, be operated in any one of many frequency bands (0–357 MHz, 357–714 MHz, etc.). To minimize expensive wide-band high-power driver amplifier power, we chose to operate in the 0–357-MHz frequency band, where the impedance of a stripline-pair kicker is greatest. In addition, the kicker impedance is largest at the lower frequencies of the dominant coupled-bunch modes.

The design of the main damping ring TFB system follows the design of a system recently commissioned at the Advanced Light Source [Barry 1993] and one planned for PEP-II [Barry 1995]. The main damping ring TFB system would differ only in the frequency bandwidth and the total power required. A block diagram of the system is shown in Figure 4-71. Two sets of button pickups, located approximately 90° apart in betatron phase, are used to detect beam moments $I\Delta x$ and $I\Delta y$. The individual button signals are processed at 2.84 GHz ($4\text{x}f_{rf}$) to benefit from greater button sensitivity at higher frequency, combined via hybrids, and demodulated to baseband. The baseband-moment signals are combined in proportion according to the Twiss parameters at the pickups and the phase advance from pickups to kicker. The signal is delayed the appropriate amount for coincidence with the bunch at the kicker. Not shown in the figure is an element for rejection of an orbit offset at the pickup. The offset rejection can implemented in several ways, for example, as a notch filter.

As mentioned, the kicker is a 50-Ω stripline pair operated in difference mode with a length of one-half the bunch spacing (21 cm). The kicker impedance is given by

$$R_{k,\perp} = 2\ Z_L \left(g_\perp \frac{l}{b} \frac{\sin(\omega l/c)}{(\omega l/c)} \right)^2 \quad , \tag{4.66}$$

where $Z_L = 50\ \Omega$, l=21 cm, and b= 1.5 cm is half of the stripline separation, and $g_\perp$ is the coverage factor and assumed to be close to unity. This configuration yields a kicker impedance of 19.6 $k\Omega$ (at $\omega = 0$). The broadband power required is given by

$$P_{k,\perp} = \frac{V_k^2}{2R_{k,\perp}} \quad , \tag{4.67}$$

where V_k is the kicker voltage. Specification of this voltage is discussed in the following section on computer simulations.

Computer Simulations

This section describes computer simulations of the coupled-bunch oscillations and the corresponding feedback system used to damp the oscillations. The purpose of performing these simulations is twofold. The first is to determine the growth rates for the actual filling pattern which are difficult to calculate analytically. The second is to empirically determine how much power is required for the system to satisfactorily damp coupled-bunch oscillations. To this end, we can include effects such as injection beam transients, pickup and kicker noise, DC orbit offsets, etc.. In particular, the simulations include the limiting of the feedback response at larger beam oscillation amplitudes. The results described here represent a first attempt to find an adequate feedback voltage for damping injection beam offsets assuming a perfect feedback system; further optimization will be performed in the future.

The beam dynamics in this study are simulated using common tracking techniques at a single point in the ring, where difference equations are used to describe the discrete time evolution of the beam oscillations and wake voltages [Siemann 1983, Thompson 1989]. This approximation is valid for all of the effects we wish to study, especially since most of the wake voltages are localized at the rf cavities. One notable exception is the distributed wake of the resistive-wall impedance, which results from the skin effect on the inner vacuum chamber wall. The local approximation for the resistive-wall wake is valid when the corresponding growth or damping rate is slow compared to the betatron oscillation period. This condition is true for all cases studied here. Tracking is done in both transverse directions, which we generically label x. The turn-by-turn difference equations for x and $x^{'}$ for a linear lattice are given by

$$x_{i+1} = \cos 2\pi Q_x x_i + \beta_x\ \sin 2\pi Q_x x_i^{'}(1 - 2\lambda_x) \tag{4.68}$$

$$x_{i+1}^{'} = -\frac{1}{\beta_x} \sin 2\pi Q_x x_i + \cos 2\pi Q_x x_i^{'}(1 - 2\lambda_x) + \frac{\Re(\tilde{V}_{w,i+1})}{E} \tag{4.69}$$

where the tracking is assumed to be at a symmetry point with $\beta^{'} = 0$ and zero dispersion. The tunes and β functions are assumed to be constant as a function of amplitude and energy. Amplitude-dependent tunes generally lower the effective coupled-bunch growth rates but here we are restricting ourselves to a worst-case scenario with no nonlinearities.

The transverse wake voltage from dipole HOMs is found by summing the contributions from all previous bunch passages. Tracking of the wake voltage is done by treating it as a complex phasor, $\tilde{V}_w$. The difference equation for $\tilde{V}_w$ is given by

$$\tilde{V}_{w,i+1} = \tilde{V}_{w,i} e^{(j\omega_r + \frac{\omega_r}{2Q})\Delta t} - j2k_\perp q\ x_{i+1} \tag{4.70}$$

where $k_\perp$ is the transverse loss parameter, ω_r is the angular resonant frequency, and x is the transverse offset at the location of the HOM.

As mentioned above, the resistive-wall wake voltage is the only non-localized wake of concern. The approximate localized wake voltage for a round pipe is given by

$$V_{w,rw}(t) = qx\frac{lc}{\pi b^3}\sqrt{\frac{\mu_0\rho}{\pi}}\frac{1}{\sqrt{t}} \tag{4.71}$$

where l is the length of the vacuum chamber (usually the ring circumference), ρ the material resistivity, and b the chamber radius. The voltage for bunch passage must be remembered and individually recalculated each iteration. The resistive-wall wake is cutoff after four turns.

Main Damping Ring Feedback Systems

The TFB system measures a transverse position error and produces the appropriate angular kick to correct the error which is applied to the beam on a subsequent turn. Because the tracking in this simulation is done at only a single point in the ring, we are currently using a linear combination of the transverse position measured on the two previous turns to calculate the correct kick given by

$$V_{fb} = G_{fb}E\left(\frac{x}{\beta_x \tan\phi_x} - \frac{x_{-1}}{\beta_x \sin\phi_x}\right) \tag{4.72}$$

where G_{fb} is the TFB gain and usually ranges from 0.03–0.3, x and x_{-1} are the positions on the current and previous turns, and $\beta_\perp = 6.5$ m in the NLC simulations. The feedback voltage limits at the maximum amplifier output voltage.

A simulation result for the case of 4 trains of 90 bunches, filled to a total beam current of 1.2 A, is shown in Figure 4-72. The injected train is offset at injection by 500 μm; with the assumed value of $\beta_\perp = 6.5$ m, this corresponds to an injection offset that is $1.2\sigma_{x,y}$. Figure 4-72 shows the transverse offset of all bunches versus turn number, and Figure 4-73 shows the corresponding feedback voltage. The feedback voltage was limited to 1500 V for this case. The injected bunches saturate the feedback and damp linearly in time until the amplifier comes out of saturation, whereupon they damp exponentially. The stored bunches are excited to very small amplitudes but are quickly damped.

A maximum voltage of 1500 V corresponds to broadband power of 60 W. Although this seems like a rather modest requirement, it is reasonable considering the relatively small offsets at injection. We expect the power to scale roughly as the square of the offset so considerably more power is needed for larger offsets. Furthermore, we have not yet considered the effects of residual orbit offset and noise which also consume power.

4.7.2 Stored Orbit Feedbacks

In addition to the coupled-bunch feedback system just described and the rf feedbacks described in Section 4.5.3, we plan to implement transverse position feedbacks in the damping rings. These will be used to maintain the beam orbit to prevent variations in the extracted beam trajectory and to prevent emittance growth or dynamic aperture reduction due to orbit shifts. Similar feedback systems are installed in most synchrotron light sources where the stability requirements are severe because of the long distances from the radiation source point to the experimental stations.

Because the revolution rate in the rings is roughly 1.3 MHz, these feedback systems are not limited by the sample rate like most other beam-based feedbacks in the linear collider. Of course, they are still limited by the corrector slew rate which depends upon the corrector magnets, the power supplies, and the vacuum chamber. Since most destabilizing effects are relatively low frequency, we do not believe that the feedbacks need to respond to frequencies above 30 Hz. In this case, the correctors can be simple air-core dipole magnets mounted around the normal vacuum

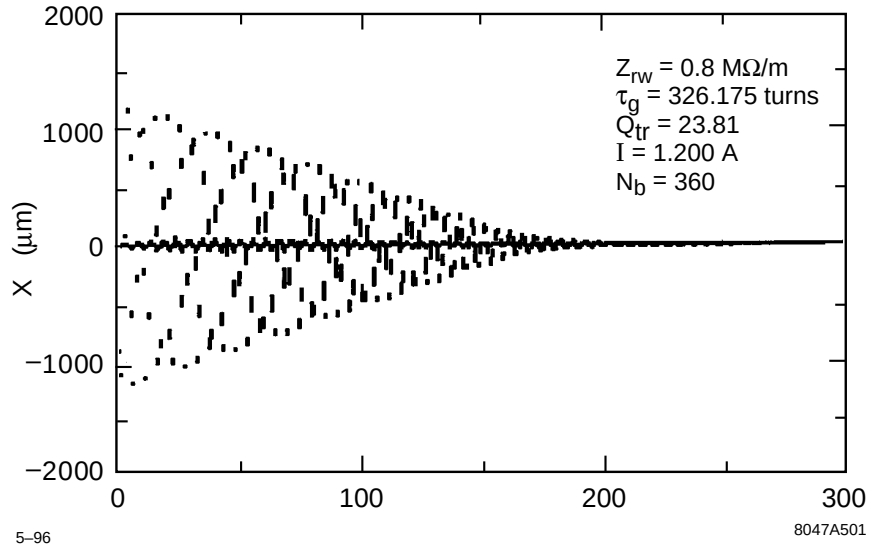

Figure 4-72. *Bunch position after a train is injected into a main damping ring with a 500-μm offset; it is difficult to resolve the individual bunches in the trains.*

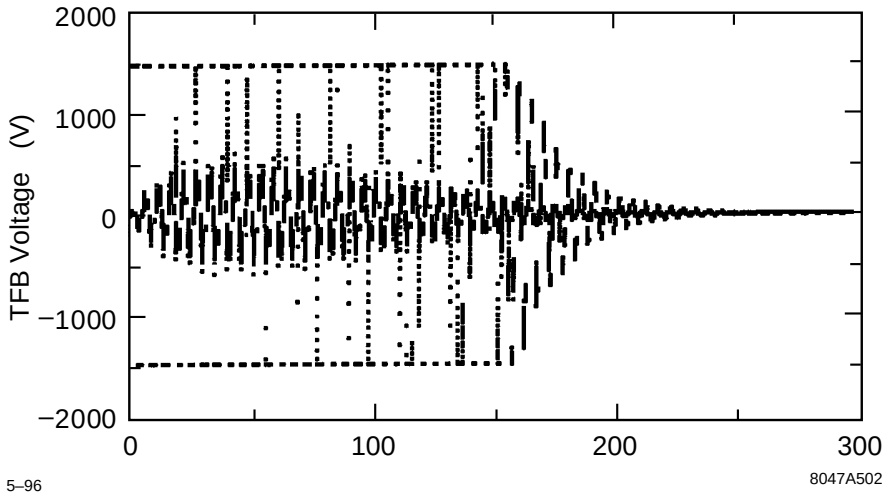

Figure 4-73. *Feedback voltage after a train is injected into a main damping ring with a 500-μm offset (1.2 sigma); notice that the feedback saturates at roughly 1.5 kV.*

chamber; they would be placed in the injection and extraction region where the vacuum chamber does not have an ante-chamber. Finally, although the feedback systems will be much more important in the main damping rings than in the pre-damping ring, they will likely be used to improve the operational stability in all three rings.

4.7.3 Injection Feedbacks

In addition, to the transverse position feedbacks in the damping rings, we will use fast beam-based feedbacks in the injection lines to stabilize the incoming trajectories, energy, and intensity:

- Bunch-by-Bunch Energy
- Bunch-by-Bunch Intensity
- Bunch Train Energy Spread
- Transverse Phase Space

These systems are similar to those used throughout the SLC and described in Appendix D.

4.7.4 Extraction Feedbacks

As in the injection lines, we will use fast beam-based feedbacks in the extraction lines to stabilize the outgoing trajectories. In addition, there will be a fast multibunch kicker system to correct for small (static) bunch-to-bunch position errors arising from the damping ring extraction kickers—these kickers are described in Chapter 7. There will also be a feedback for the damping ring phase based on the extracted beam trajectory through the bunch compressor; this is described in Section 4.5.3.

Finally, there will be an intensity feedforward system that will adjust the beam loading compensation in the linacs to fluctuations in the bunch train charge; a similar system is used in the SLC to stabilize the electron beam energy. The bunch train charge will be measured near the end of the store cycle. Without a feedforward system, the tolerance on variations in the bunch train charge is 0.3% to limit the energy deviation at the IP to 0.1%. It is expected an intensity feedforward system will reduce the bunch train intensity jitter tolerance by over a factor of five by adjusting the linac beam loading compensation to the measured beam charge. In addition, the feedforward system would automatically trigger the beam dumps, either at the end of the linac or at the end of the first or second bunch compressor, if the deviation in bunch train charge exceeds specified limits; such a system is needed to limit backgrounds in the detector at the IP.

4.8 Vibration and Stability

4.8.1 Vibration

Vibrations of the quadrupole magnets due to the ground motion will cause the beam trajectory to vary. The two dominant sources of vibrations are ground motion that is transmitted and possibly amplified by the magnet supports,

and a man-made noise, *e.g.*, generated by cooling water flow in the magnets [Turner 1995]. The latter, however, is more difficult to analyze, because much will depend on water cooling system and magnet supports design. Regardless, with proper design, the effect of cooling and other man-made sources should be minimal. For example, in the ALS synchrotron light source, the magnet cooling was measured to increase the magnet vibration by roughly 1 nm [Greene 1992]; motion at ten times this amplitude is still acceptable.

The effect of the vibrations on the beam trajectory depends crucially on the correlation from magnet to magnet. For high frequencies, when the wavelength of the ground waves is smaller than the distance between the quadrupole magnets, the magnet vibrations are uncorrelated. In this case, each magnet contributes independently in inverse proportion to the square of its focal length to the perturbation of the closed orbit. In the intermediate range corresponding to the wavelengths larger than the distance between the magnets, but smaller then the dimensions of the ring, one can expect resonant effects in the dependence of the closed orbit distortion on the frequency [Rossbach 1988]. At very small frequencies, when the wavelength becomes much larger than the size of the ring, the main components of the ground motion will be a rigid displacement and a tilt of the ring, which do not distort and displace the closed orbit relative to the magnets. However, the amplitude of the ground vibrations grows sharply when the frequency decreases.

The vertical perturbation of the closed orbit can be characterized by its deviation $y_B(s)$ from the ideal trajectory. We denote the value of this function at the location of ith quadrupole magnet by y_{Bi}. It is given by

$$y_{Bi} = \sqrt{\beta_i} \sum_i G_{ij} y_j \quad , \tag{4.73}$$

where β_i is the beta function and y_i is the displacement of the ith quadrupole, and the coefficients G_{ij} are computed from the known parameters of the lattice.

The matrix elements G_{ij} should satisfy the following sum rules,

$$1 = \sqrt{\beta_i} \sum_j G_{ij} \quad , \tag{4.74}$$

$$\left\{ \begin{array}{c} x_i \\ z_j \end{array} \right\} = \sqrt{\beta_i} \sum_j G_{ij} \left\{ \begin{array}{c} x_j \\ z_j \end{array} \right\} \quad . \tag{4.75}$$

The first of these two equations is due to the fact that if the entire ring shifts vertically as a rigid body by one unit, the closed orbit moves together with the ring by the same distance. The second equation expresses that the tilting of the ring in either x or z direction would also cause the same tilting of the orbit. These two sum rules are particularly important in the limit of low frequencies when the main components of the ground motion are the shifts and the tilts of the ring. Equations 4.74 and 4.75 guarantee that they do not produce distortions of the closed orbit relative to the magnets, and only the deformations of the shape of the ring would contribute to the closed orbit perturbation.

In order to eliminate rigid shifts and tilts of the closed orbit which go together with the ring and do not move the beam trajectory in the vacuum chamber, we consider the average square of the difference between the orbit and the magnet displacements,

$$\delta y_i^2 = \left\langle \left(y_{Bi} - y_i \right)^2 \right\rangle . \tag{4.76}$$

Using Eq. 4.74, we find that

$$\left\langle \delta y_i^2 \right\rangle = \sum_i G_{ij} G_{ik} \left[\left\langle y_i^2 \right\rangle - 2 \left\langle y_i y_j \right\rangle - \left\langle y_j y_k \right\rangle \right]. \tag{4.77}$$

The expectation value of the mixed product $\langle y_i y_j \rangle$ can be expressed in terms of the two-dimensional power spectrum of the ground motion, $P(\omega, k)$,

$$\left\langle y_i y_j \right\rangle = \int_0^\infty \frac{d\omega}{2\pi} \int_0^\infty P(\omega, k) \cos(k l_{ij}) \frac{dk}{2\pi} \quad , \tag{4.78}$$

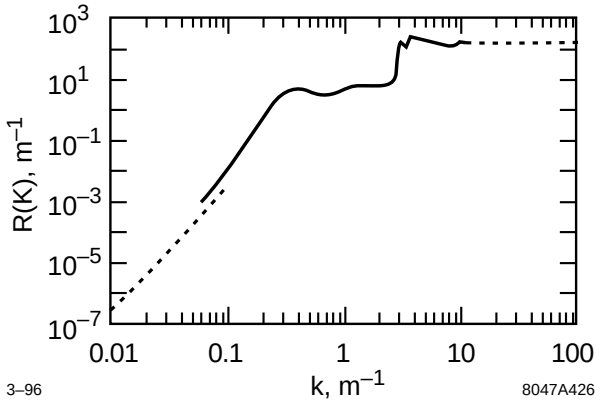

Figure 4-74. *Plot of the averaged response function for the NLC damping ring.*

where l_{ij} denotes the distance between the ith and the jth quadrupoles. We use the following representation for $P(\omega, k)$, $P(\omega, k) = P(\omega)\,\mu(\omega, k)$, where $P(\omega)$ is the integrated power density of the ground motion, and $\mu(\omega, k)$ describes the correlation of the ground motion at different points. In the model developed in Appendix C.2, this function is equal to

$$4 \Big/ \sqrt{\omega^2 / v(\omega)^2 - k^2} \quad , \tag{4.79}$$

where v denotes the velocity of the ground waves. In our calculations, we used a simpler model assuming that

$$\mu(\omega, k) = \begin{cases} 2\pi v(\omega)/\omega, & k < \omega / v(\omega) \\ 0, & k > \omega / v(\omega) \end{cases} \quad , \tag{4.80}$$

where $v(\omega)\ [\mathrm{m/s}] \approx 450 + 1900 \exp(-\omega/4\pi)$, and ω is measured in s^{-1} [Adolphsen 1995]. Qualitatively, this dependence tells that the contribution to the function $\mu(\omega, k)$ at the frequency ω comes, with equal weights, from the waves with the wavenumbers below $\omega / v(\omega)$ only. For the original model in Appendix C, the weights are not equal, with a larger contribution coming out from the vicinity of $k = \omega / v(\omega)$.

The final expression for δy_i^2 takes the form

$$\left\langle \delta y_i^2 \right\rangle = \beta_i \int_0^\infty \frac{d\omega}{2\pi} P(\omega)\, R_i\left(\frac{\omega}{v(\omega)}\right) \quad , \tag{4.81}$$

where $R_i(k)$ is the response function for the lattice at the location of the ith quadrupole. We average this function over the ring and denote it as $R(k)$; it is plotted in Figure 4-74.

For large ω, ($\omega > 2\pi \times 250\ Hz$), R approaches the high-frequency limit of uncorrelated quadrupole vibrations. It is approximately constant in this region with a value of about $R \approx 160\ m^{-1}$ shown by the horizontal dashed line in Figure 4-74. For very small frequencies, one can prove that $R \approx Ak^4$, where $A \approx 30\ m^3$; this asymptote is also shown in Figure 4-74 by a dashed line.

Assuming a spectrum of ground motion [Juravlev 1995]

$$P(\omega) \left[\frac{\mu m^2}{Hz}\right] \approx \frac{1.6 \times 10^{-3}}{\omega^4} \quad , \tag{4.82}$$

where ω is given in s^{-1}, we found the following value for δy_i upon integration in Eq. 4.81 from zero to infinity,

$$\sqrt{\langle \delta y_i^2 \rangle} = 0.14 \text{ nm} \quad . \tag{4.83}$$

This is negligibly small in comparison with a typical vertical size of the bunch of the order of 5 μm.

The high frequency limit of the function R can easily be translated into the tolerance for the uncorrelated motion of the quadrupoles in order the beam trajectory vary less then 10% of the vertical size of the beam. For the nominal emittance $\gamma\varepsilon_y = 2 \times 10^{-8}$ m-rad, the uncorrelated vibration of the quadrupoles should not exceed 18 nm.

Finally, if the trajectory motion is too large, one can use a global orbit feedback to stabilize the trajectory in the ring. Because of the high-revolution frequency, this is a straightforward feedback system (see Section 4.7).

4.8.2 Stability

In addition to the high frequency motion of the ground, there are alignment and electronic drifts that need to be controlled. To maintain the vertical emittance the closed orbit must not drift by more than 10 μm. This implies a tolerance on the magnet alignment and, more importantly, on the BPMs and BPM electronics. The primary sources of drift are thermal fluctuations and slow movement of the ground.

To estimate the effect of the ground fluctuations, we use the ATL-model which predicts that the rms difference in the displacement of any two points is given by $\Delta y^2 = A\,T\,L$ where A is a coefficient, T is the time, and L is the distance between the two locations. Using a coefficient of $A = 5 \times 10^{-7}\ \mu\text{m}^2 s^{-1} m^{-1}$, which is an upper limit on the value that has been measured at SLAC (see the discussion in Appendix C), we find that the stored orbit will vary by 10 μm after roughly 24 hours. This is not a significant limitation—it is reasonable to expect to correct the closed orbit every 24 hours. Furthermore, this trajectory variation would be substantially reduced by a global orbit feedback as discussed in Section 4.7.

Of course, it does not do any good to re-correct the closed orbit if the BPM readbacks are drifting due to either electronic variations or physics drifts. This is where the tolerance on the thermal stability is very important. To minimize the BPM drifts, we will anchor the BPMs to the magnets so that they are constrained transversely and temperature in the ring tunnel will be maintained to a fraction of a °C, while that in the electronics racks will be stabilized to 1°C. With this thermal regulation, we would hope to limit the BPM drifts to less than 10 μm over 24 hours.

4.9 Alignment and Supports

The main damping rings and downstream systems all have very tight alignment and field tolerances to prevent dilution of the transverse emittances. In all cases, these tolerances will be attained using beam-based alignment techniques where the alignment accuracy depends on beam measurements and not mechanical systems; the techniques to be used in the damping rings are described in Section 4.9.3.

To attain the desired vertical emittances and dynamic aperture, the magnets in the main damping rings must be aligned to the level of 50∼100 μm in the vertical plane and $100 \sim 200\,\mu$m in the horizontal plane; these tolerances are specified in Sections 4.3.8 and 4.3.9. In addition, the vacuum chamber must be aligned at the level of ∼500 μm to prevent synchrotron radiation from hitting the inside of the beam chamber. Of course, these tolerances refer to the alignment over a relatively short distance (1 or 2 cells) and not globally.

To attain these tolerances, we plan to rely on beam-based alignment of the quadrupoles and sextupoles. Unfortunately, one cannot do the same for the combined-function bending magnets; these need to be aligned using conventional techniques to 200-μm rms (see Section 4.3.8).

In the downstream systems (X-band linacs, final focus, etc.), the alignment will be implemented using remote magnet movers. In the damping rings the tolerances are sufficiently loose that there is some question as to whether magnet movers are required; once the alignment is known, one could mechanically perform the differential moves to attain the desired alignment. Mechanical alignment could only be considered if the alignment is stable at the 50-μm level for months—experience from the ALS and calculations using the "ATL" model would suggest that this is the case. Regardless, the mover question will be determined in the future; for this design, we have assumed magnet movers.

4.9.1 Girders and Supports

The girder and support systems are still being designed. The concept is similar to that adopted in the collimation section and the final focus. The supports would be mounted on a low concrete girder attached directly to the floor. The magnet movers would then be mounted on the girders and aligned using shims. Finally, the magnets would be mounted on the movers.

The movers could be similar to the linac movers, described in Chapter 7. These are based on the SLAC Final Focus Test Beam (FFTB) magnet movers and have a range in excess of ± 1 mm in x and y with a 0.3-μm step size. Of course, the damping rings do not such high precision and a simpler design would probably be adopted.

4.9.2 Mechanical Alignment

Mechanical alignment will be used to pre-align the quadrupoles and sextupoles in the damping rings and to align the elements that cannot be aligned using beam-based alignment, *i.e.*, the bending magnets, vacuum chamber, and rf cavities. The required alignment is 200 μm, which is well within the capabilities of modern equipment.

4.9.3 Beam-based Alignment

Attaining the required magnet alignment, in the main damping rings, through purely mechanical systems will be difficult. For this reason, we plan to use beam-based alignment to determine the positions of the quadrupoles and sextupoles with respect to the beam. Quadrupole beam-based alignment is being used at MAX-lab [Rojsel 1994], LEP [Barnet 1994], ALS [Robin 1995] and SSRL. In all these rings, it is possible to adjust the fields in each quadrupole individually, either with separate power supplies or with additional trim windings. All techniques vary the quadrupole field and measure the orbit variation; the magnitude of the orbit change is proportional to the quadrupole-to-beam offset.

The actual algorithm used to deduce the offsets is somewhat different in each of the laboratories, but once the quadrupole-to-beam offset is determined, it is referenced to the adjacent BPMs. The quadrupole-to-BPM offsets are then used to either re-align the magnets or to steer the beams through the center of the quadrupoles.

How accurately one can measure these quadrupole-to-BPM offsets depends upon several quantities: the reproducibility of the BPMs, stability of the correctors and other magnets, and physical motion of the machine. At the ALS, the

quadrupole-to-BPM offset can be measured with a repeatability that is better than ± 5 microns [Robin 1995]. This is at the level of the BPM noise and is well within the necessary tolerances required in the NLC.

Sextupole beam-based alignment is being used at KEK [Kamada 1994] and at DESY [Herb 1995]. In these measurements, a local orbit bump is made in a section of the ring containing one sextupole. All the sextupoles in that family are then varied as a whole and the change in the resulting orbit is measured. The amplitude of the orbit bump is changed and the measurement is repeated. The horizontal deflection then depends quadratically upon the orbit offset while the vertical deflection is linear in the offset:

$$\theta_x = 0.5 K_2 l (\Delta X + x_m)^2 \qquad \theta_y = K_2 l \Delta X y_m \quad , \tag{4.84}$$

where $K_2 l$ is the integrated sextupole strength, ΔX is the orbit offset, and x_m and y_m are the sextupole misalignments. By fitting the resulting oscillations, the sextupole center was inferred a resolution of several hundred microns in TRISTAN [Kamada 1994].

This process will be simplified in the NLC damping rings because all of the sextupoles will have individual power supplies and the BPMs will have 1-μm resolution. To estimate the resolution of technique, we assume that the orbit is moved in five steps by a total of ± 250 μm in the sextupole while measurements are made of the closed orbit with the sextupole on and off; it is necessary to turn the sextupole on and off to isolate the individual magnet—alternately, one could use a remote magnet mover to move just the sextupole to be aligned. By using all of the ring BPMs to fit the resulting betatron oscillations to a single kick at the sextupole location, the effective BPM resolution should decrease to roughly 0.1 μm. Of course, systematic errors will degrade this effective resolution and thus we will assume a 0.5-μm effective resolution. In this case, one should be able to determine the vertical alignment of the sextupole with a resolution of roughly 20 μm; this is clearly sufficient, although higher resolution could be obtained with a larger orbit step size.

Unfortunately, this technique will be slow. To align all of the sextupoles in each of the main rings will probably take many hours. There are several possible directions in which one may try to improve the speed of the measurement. First, putting an additional winding on four of the six poles of the sextupole would provide a quadrupole field [Raubenheimer 1995b, Kikuchi 1995]. This would allow one to use the quadrupole beam-based alignment techniques to find the quadrupole center which should be close to the sextupole magnetic center; this should be significantly faster. Second, one could vary multiple sextupoles at once and fit for a number of kicks at the same time; this will degrade the resolution but it will still probably be sufficient. Third, one could vary the sextupole strength and measure the tune variation. For example, turning off a sextupole in which the beam is horizontally offset by 50 μm will cause tune changes of roughly $\Delta\nu \approx 0.001$—easily measurable. Unfortunately, applying this technique to the vertical alignment is more difficult, although it may be possible by operating on the difference coupling resonance and measuring the resulting tune separation. All such combined approaches require additional research.

At this point, we have not estimated the frequency with which beam-based alignment would have to be used. If it is required often (daily), the alignment system must be highly automated and the magnets would need to be mounted on movers. Fortunately, the alignment tolerances are relatively loose (compared to the rest of the collider) and it is expected that alignment would only need to be performed at the beginning of a run. Experience at the ALS suggests that the alignment is stable to better than 50 μm over periods of six months or more [Robin 1995].

One of the important problems that needs to be resolved is how the BPMs are mounted to the magnets. At the ALS, the BPMs are mounted in the vacuum chamber and this is free move transversely. Thermal fluctuations then cause the BPM positions to drift by as much as 50 μm. Designs have been suggested that allow the BPMs to be mounted in the chamber but will constrain the transverse movement at the magnets; this is clearly desirable.

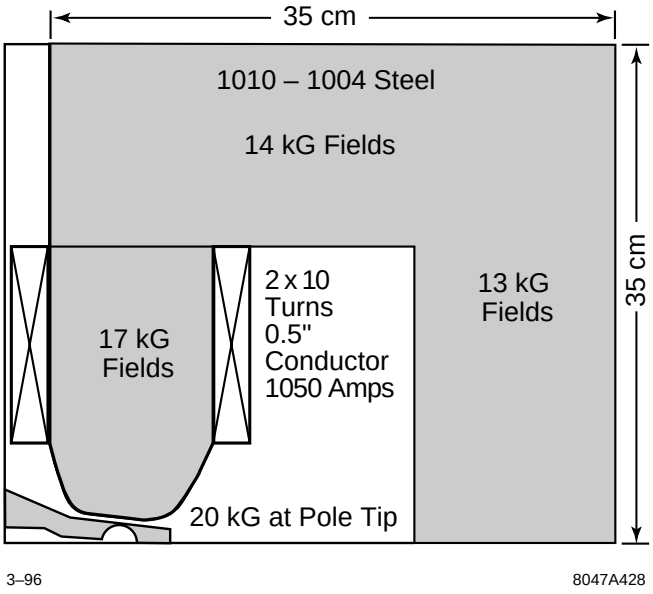

Figure 4-75. *Main damping ring "C" bend magnet cross section.*

4.10 Magnet Design and Power Supplies

4.10.1 Main Damping Rings

Bending Magnets

The required field parameters of the bending magnets are listed in Table 4-24 for nominal energy of 1.98 GeV. The magnet is a high-field combined-function magnet with a 15-kGauss field and a relatively strong quadrupole gradient. The full aperture at the beam pipe location is 3.2 cm and the required good field region is ± 0.5 cm.

To determine the feasibility of the bending magnets, we completed a first pass at the design of an "H" magnet using the 2D computer code POISSON and the 3D code TOSCA. Although the "H" style magnet seemed possible, the required fields and the geometry naturally lend themselves to a "C" style magnet. Thus, we have modeled a similar design with POISSON based on the "C" geometry; this magnet is illustrated in Figure 4-75 with a blowup of the pole in Figure 4-76.

In both cases, the required fields are attained using standard 1010 magnet iron with peak fields in the pole tip of 19.6 kGauss. The fields are sufficiently high that saturation effects cause the relative quadrupole and higher multipole components to vary as a function of excitation. The deviation of the magnetic field from a simple dipole field with a linear gradient is plotted in Figure 4-77 for three different excitation currents. The variation of the relative quadrupole is $\sim$1% but it, as well as the variation in the sextupole component, is easily compensated; the higher-order multipoles are not significant.

The magnet is a sector magnet and, because the sagitta is substantial (1.3 cm), the magnet pole must be curved along the beam trajectory. At this time, we have not considered construction techniques although it seems most likely that

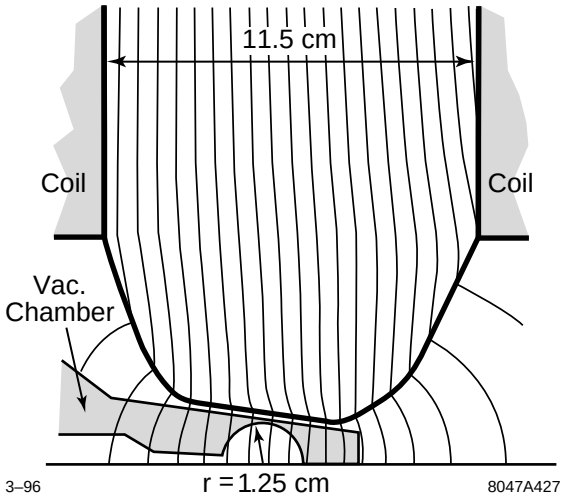

Figure 4-76. *Main damping ring "C" bend magnet pole.*

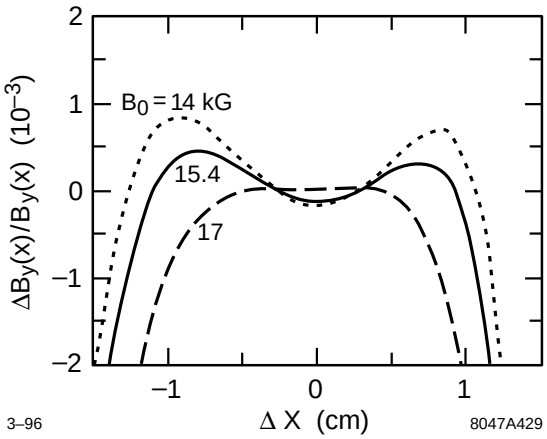

Figure 4-77. *Main damping ring "C" bend magnet multipoles versus excitation for ring operation from 1.8 GeV to 2.2 GeV.*

the magnets would be machined with solid cores to accommodate the curvature; the KEK ATF dipole magnets are being constructed in a similar fashion. We have estimated that a construction tolerance of 25 μm is needed to attain the required field quality.

The ends of the poles will be chamfered at a 60° angle. For convenience, we plan to use removable end pieces on the magnets. Here, the last 4 cm (or so) of the pole is removable to allow straightforward optimization of the fringing fields and future modifications; similar pole-ends are used on the SLC damping ring bending magnets. At this time, we have not studied the fringing fields at the magnet ends of the "C" magnet design. Although the "H" magnet design and other previous experience with combined function magnet design [Raubenheimer 1993a] leads us to believe that they should not be difficult, in the future, we will model the magnet in 3D and include the fringing fields in the dynamic aperture calculations.

Dipole Magnet Designs:	2
Main Bends:	
Number	38
Magnetic Length	68.4 cm
Half Gap	1.6 cm
Amp-turns	40,900
$B_{0\,\mathrm{eff}}$	15.3 kGauss
$B_1\ (dB_y/dx)$	126 kGauss/ m
Matching Bends:	
Number	4
Magnetic Length	40 cm
Half Gap	1.6 cm
Amp-turns	34,500
$B_{0\,\mathrm{eff}}$	13.0 kGauss
$B_1\ (dB_y/dx)$	107 kGauss/ m

Table 4-24. *Dipole magnet parameters for main damping rings at 1.98 GeV.*

It is also important to include the fringing field when calculating the radiation damping rate [Rivkin 1985]. To this extent, we have quoted the field in terms of $B_{0\,\mathrm{eff}}$ which is defined as:

$$B_{0\,\mathrm{eff}} \equiv \sqrt{\int_{-\infty}^{\infty} ds \frac{B_0^2}{L_B}} \tag{4.85}$$

and is the quantity that determines the synchrotron radiation damping. In general, the peak field in the center of the dipole will be slightly greater than $B_{0\,\mathrm{eff}}$ because of the fringe fields.

The main dipole magnet coils will be constructed from two layers, with 10 turns per layer, of 0.5-in square water-cooled conductor to provide a total of 45,000 A-turns for operation at 2.2 GeV. The matching bends have half the integrated field and gradient of the main bending magnets. To reduce the fringing fields, we increased the length and decreased the fields. Since the magnets have the same ratio of field to gradient as the main bending magnets, they would be constructed with the same cross section as the main bends but powered with 38,000, rather than 45,000 A-turns, for 2.2-GeV operation. At this time, we have not considered whether an additional trim coil will be needed to account for the different saturation behavior of the matching the main bending magnets.

All of the bends in each ring will powered by a single 100-kW power supply rated at 800 V and 1250 A. The stability of the main power supply is not very critical. Only low-frequency variations penetrate the vacuum chamber. Thus, the primary effect of bend power-supply fluctuations are slow shifts of the stored beam energy. This has three effects: (1) the bunch compressor converts the energy changes to changes in the beam phase and therefore energy fluctuations at the IP (this effect is discussed further in Chapter 5), (2) in regions of dispersion, the close orbit shifts, and (3) the betatron tunes change by an amount proportional to the uncorrected chromaticity.

In general, the most severe limitation is that on the extracted beam energy. To limit the fluctuations to 1/20 of the rms beam energy spread, the power supplies must regulate better than $\Delta I/I = 5 \times 10^{-5}$. This will cause tune variation at the level of 0.002 and 0.001 in the horizontal and vertical planes and it will cause the beam energy to fluctuate at the IP by roughly 0.05%. The horizontal and vertical orbit shifts at the extraction point, which are proportional to the residual dispersion, will be much less than 1/10 of the respective beam sizes.

Magnet	Quan.	K1 (m^{-2})	B_{pole} (kGauss)	Mag. Len. (cm)	Aper. (cm)
QFH (Arc Quad)	72	7.9	7.9	20	1.5
QDH (Arc Quad)	36	-6.0	6.0	15	1.5
QFHM (Arc Matching)	4	7.5	7.5	20	1.5
QDHM (Arc Matching)	4	-7.1	7.1	15	1.5
QM2 (Eta Matching)	4	8.9	8.9	20	1.5
QM3 (Inj/Ext Matching)	2	-5.3	5.3	15	1.5
QM4 (Inj/Ext Matching)	2	6.7	6.7	20	1.5
QM5 (Inj/Ext Matching)	2	-2.0	2.7	15	2.0
QM6 (Inj/Ext Matching)	2	2.0	2.7	15	2.0
QFX (Inj/Ext cells)	2	2.9	5.9	15	3.0
QDX (Inj/Ext cells)	2	-2.3	3.1	15	2.0
QM3W (Wiggler Matching)	2	-5.3	5.3	15	1.5
QM4W (Wiggler Matching)	2	6.3	6.3	20	1.5
QM5W (Wiggler Matching)	2	-0.4	0.8	15	3.0
QM6W (Wiggler Matching)	2	0.4	0.8	15	3.0
QFW (Wiggler cells)	2	2.8	5.6	15	3.0
QDW (Wiggler cells)	2	-1.0	2.0	15	3.0

Table 4-25. *Quadrupole magnets for NLC main damping ring vers. 6.11 at 1.98 GeV.*

Quadrupole Magnets

The required parameters of the quadrupole magnets are listed in Table 4-25 for the at the nominal energy of 1.98 GeV. Five basic magnet designs are needed:

1. A 20-cm magnetic length with a maximum 10.3-kGauss pole-tip field (at 2.2 GeV) and a 1.5-cm radius aperture for the dispersion matching.
2. A 20-cm magnetic length with a maximum 9.3-kGauss pole-tip field (at 2.2 GeV) and a 1.5-cm radius aperture for the arc QFs.
3. A 15-cm magnetic length with a maximum 8.2-kGauss pole-tip field (at 2.2 GeV) and a 1.5-cm radius aperture for the arc QDs.
4. A 15-cm magnetic length with a maximum 5-kGauss pole-tip field (at 2.2 GeV) and a 2.0-cm radius aperture for the injection and extraction region.
5. A 15-cm magnetic length with a maximum 7-kGauss pole-tip field (at 2.2 GeV) and a 3.0-cm radius aperture for the wiggler region.

The larger-radius quadrupoles are needed in the wiggler and injection and extraction regions to accommodate the wiggler region vacuum chamber and the injected and extracted beam trajectories. The five families are summarized in Table 4-26.

Quadrupole Magnet Designs:	5
Arc QFs:	
Number	80
Magnetic Length	20 cm
Inscribed Radius	1.5 cm
Max. $B_{\rm pole}$	9.3 kGauss
Main Coil	15 turns
Max. Current	410 A
η QFs:	
Number	4
Magnetic Length	20 cm
Inscribed Radius	1.5 cm
Max. $B_{\rm pole}$	10.3 kGauss
Main Coil	17 turns
Max. Current	410 A
Arc QDs:	
Number	44
Magnetic Length	15 cm
Inscribed Radius	1.5 cm
Max. $B_{\rm pole}$	8.2 kGauss
Main Coil	15 turns
Max. Current	350 A
Inj/Ext Quads:	
Number	6
Magnetic Length	15 cm
Inscribed Radius	2.0 cm
Max. $B_{\rm pole}$	5 kGauss
Wiggler Quads:	
Number	10
Magnetic Length	15 cm
Inscribed Radius	3.0 cm
Max. $B_{\rm pole}$	7 kGauss

Table 4-26. *Quadrupole magnet parameters for NLC main damping rings at 2.2 GeV.*

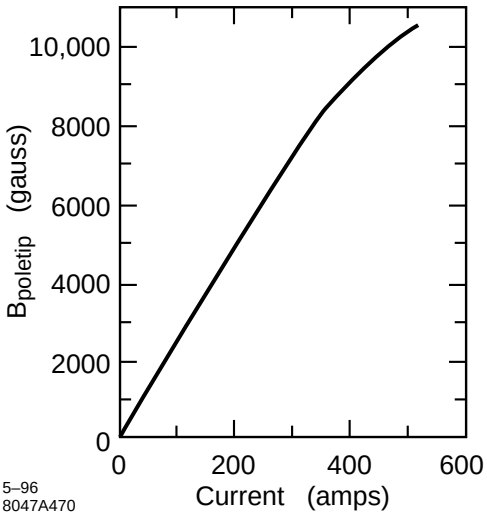

Figure 4-78. *Pole-tip field versus current for symmetric arc quadrupole design.*

As discussed in Section 4.3.9, we have assumed that the quadrupoles would be constructed in two pieces, as was done for both the ALS and APS synchrotron light sources; this will reduce the random multipoles arising from construction errors. Thus, we assumed an uncorrelated pole-to-pole error (significantly reduced relative to four-separate-pole construction) of 0.77 mils (20 μm) rms in the pole placement in the transverse plane and the two-pole correlated contribution which can characterized in terms of a relative translation (in the transverse plane) and rotation of the two halves. The former we assumed to be 1.5 mils (40 μm) in each of the two dimensions, and the latter to be 1.1 mr, corresponding to a linear displacement of 8.9 mils (225 μm) at a 20-cm arm length. The resulting multipoles are described in Section 4.3.9.

The design of the arc quadrupole magnets is further complicated by the vacuum ante-chamber. The ante-chamber is 3-cm high and in excess of 25-cm wide as illustrated in Figure 4-66. Thus, it is not reasonable to design the magnet around the chamber. We are pursuing two approaches of accommodating the ante-chamber: first, a symmetric design where iron is removed from the mid-plane on both sides of the magnet, and, second, the asymmetric case where iron is only removed from one side of the midplane. The former approach has been adopted at the APS storage ring and latter was adopted for the ALS ring. In both cases, the systematic magnet multipoles were corrected using shims to levels below our tolerances (see Section 4.3.9).

These two cases have been modeled with POISSON and the pole-tip field versus current for the symmetric case is plotted Figure 4-78.

The straight-section quadrupoles have larger apertures but are thought to be more straight-forward and we have not yet modeled them. In the injection/extraction magnets, there is no ante-chamber and the large bore wiggler magnets were sized to encompass the wiggler section ante-chamber easily; we will re-size these magnets after the wiggler vacuum chamber design is completed.

Each quadrupole will have an independent power supply which adds substantial flexibility to the lattice design and simplifies the beam-based alignment procedures since an additional trim winding is not needed on each quadrupole. The disadvantage of the independent supplies may be the additional cost.

The primary effect of quadrupole power-supply fluctuations are changes in the betatron tunes and the orbits. We have calculated tolerances on the power supplies assuming independent power supplies which have uncorrelated

Magnet	Quan.	K2 (m^{-3})	$B_{\rm pole}$ (kGauss)	Mag. Len. (cm)	Aper. (cm)
S1	76	-220	2.1	9	1.7
S2	76	+460	4.5	9	1.7
S3	76	-420	4.1	9	1.7

Table 4-27. *Sextupole Magnets for NLC Main Damping Ring at 1.98 GeV.*

Sextupole Magnet Designs:	1
Arc Sextupoles: Number	216
Magnetic Length	9 cm
Inscribed Radius	1.7 cm
Max. $B_{\rm pole}$	5.5 kGauss
Main Coil	10 turns
Trim Coil	29 turns
Max. Current	260 A

Table 4-28. *Sextupole magnet parameters for NLC Main Damping Ring.*

fluctuations. The tolerance to limit the fluctuations in the tunes to 0.001 is $\Delta I/I = 2 \times 10^{-4}$. Further assuming an rms orbit displacement in the quadrupoles of 500 μm, this power-supply tolerance will cause horizontal and vertical orbit fluctuations of 0.5% and 5% of the respective beam sizes. Finally, if the quadrupoles were on string supplies or if the power supply fluctuations are correlated, the magnitude of the orbit errors does not change (assuming random orbit offsets) but the sensitivity to the tune variation increases by roughly a factor of 10, making the tolerance $\Delta I/I = 2 \times 10^{-5}$.

Sextupole Magnets

The required parameters of the sextupole magnets are listed in Table 4-27 for the nominal energy of 1.98 GeV. All the sextupole magnets have similar parameters and would likely be constructed from the same design; these parameters are summarized in Table 4-28.

Like the quadrupole magnets, the design of the sextupole magnets is complicated by the vacuum ante-chamber. Because we would like to use trim coils in the sextupoles to implement dipole and possibly skew quadrupole correction, we are only pursuing the asymmetric, where iron is only removed from one side of the mid-plane, approach of accommodating the ante-chamber; this philosophy has been adopted at the ALS ring.

This magnet has been modeled with POISSON and a plot of the pole-tip field versus current appears in Figure 4-79. In addition, a drawing of the whole magnet is shown in Figure 4-80.

In addition to the main coils, we are planning to use trim windings on some magnets as dipole correctors. The present magnet modeling has include a single trim winding capable of producing pole-tip fields of roughly 600 Gauss; this is more than sufficient for the dipole correction.

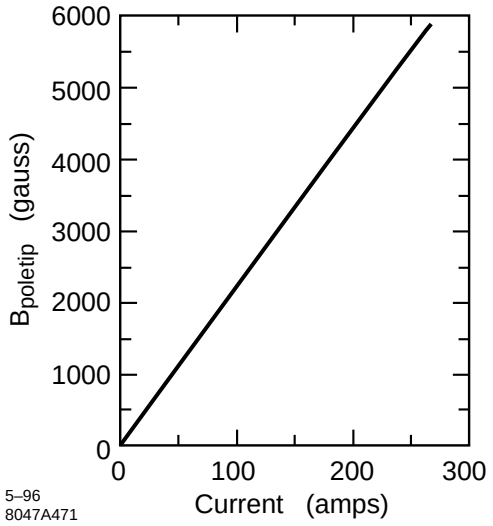

Figure 4-79. *Pole-tip field versus current for asymmetric arc sextupole design.*

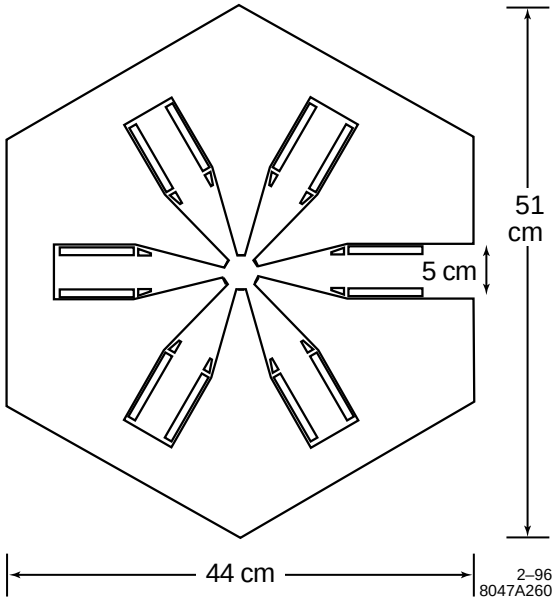

Figure 4-80. *Main damping ring sextupole design.*

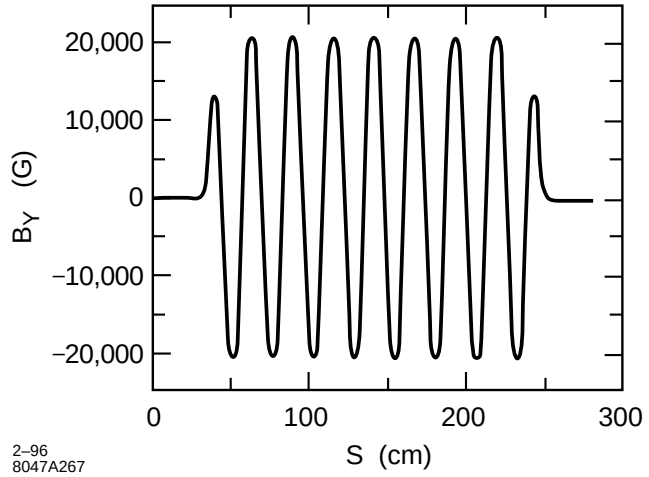

Figure 4-81. *Measured wiggler field in SSRL BL-9 wiggler [Baltay].*

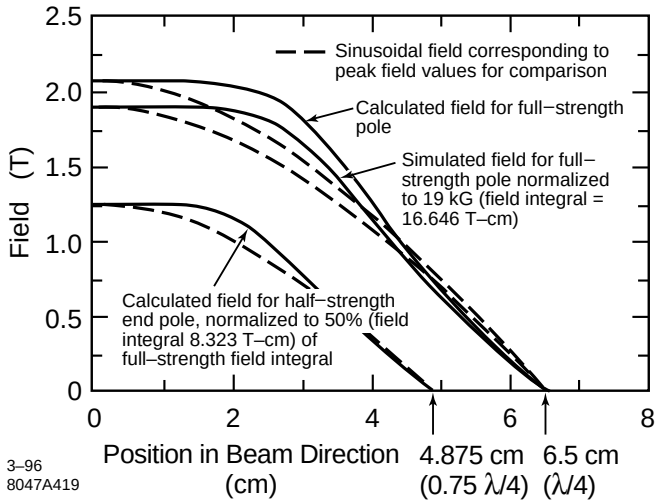

Figure 4-82. *Field from SSRL BL-9 wiggler using shaped poles [Baltay].*

Wiggler Magnets

The main damping rings require roughly 25 m of strong wiggler to attain the desired damping times. The two parameters that are relevant for a damping wiggler are the integral of $B_y^2(s)$, which determines the damping, and the quantum excitation which is determined by the wiggler period and the field. To achieve the desired vertical damping time of 4.63 ms, the integral of B_y^2 over the length of the wiggler must be 6200 kGauss^2-m, and to constrain the emittance dilution, the quantum excitation due to the wiggler should be less than that of the arcs.

We have chosen to consider a relatively short, high-field, short-period device. If we assume a sinusoidal field with a peak field of 22 kGauss (close to the saturation of Vanadium Permendur), then we need a length of 25.6 m and a period of roughly 25 cm. Using simple scaling laws, it is thought that such a device could either be constructed as an electro-magnetic wiggler or as a permanent magnet hybrid wiggler.

The SSRL Beam-Line 9 wiggler nearly meets our requirements [Baltay]. It is a hybrid wiggler with a length of 2.14 m, a 26-cm period, and a peak field of 20.5 kGauss. Because the wiggler poles were designed to optimize the total flux, the field is not sinusoidal and the integral of B_y^2 averaged over one period is within 1% of the required field in the main damping rings. When the matching poles at the ends of the wiggler are included, the field is within 3% of the required field. The measured field profile along the wiggler is plotted in Figure 4-81 and a comparison between the normal sinusoid field pattern and that of the wiggler is plotted in Figure 4-82 [Baltay].

Our goal in choosing the wiggler parameters was to minimize the length of wiggler needed and thereby the cost. It was thought that, for a given technology, the costs scaled with length. At a later time, it may be decided that this was not an optimal choice. In that case, we could increase the length, decreasing the peak field and increasing the wiggler period. For example, it might be more reasonable to consider a 30-m wiggler with a peak field much less than 20 kGauss, and a 30-cm period. Alternately, we could increase the ring energy—the required peak field scales as $1/\sqrt{\gamma}$.

Injection and Extraction Septa

For the injection and extraction scheme shown in Figures 4-13 and 4-14, there are 3 m of space for the septa. As an initial design, we have assumed a DC current sheet septa that has a 1-cm vertical aperture and is composed of two pieces: an 83-cm segment and a 1-m section; the two sections are separated by 15 cm. The initial section has a 5-mm-thick blade and a 2-kGauss field while the second section has a 15-mm-thick blade which would consist of three turns of conductor and a 6-kGauss field. Both sections would be powered in series with roughly 1800 A, producing a total bend angle of 115 mr. The current density in the blades is 36 Amps/mm^2 which is roughly one third the current density in the SLC damping-ring septa blades. The cooling channels have not been studied yet but the requirements are relatively loose; a coolant flow of roughly 1 GPM will limit the temperature rise to 6°C in the first section and 30°C in the second segment.

The dipole field quality along the injected and extracted beam trajectories is less than 2×10^{-4} over a radius of 3 mm; this is roughly 2 sigma of the injected beam. Finally, both septa require back-leg coils to decrease the field on the close orbit. A back-leg trim of 15 A-turns on the first segment will reduce the field on the closed orbit to much less than 0.5 Gauss with an insignificant gradient, and a back-leg trim of 150 A-turns will reduce the field from the second segment to similar levels.

The tolerance on the septum field is determined from the extracted beam angular divergence at the septum which is roughly 8 μr. Thus, to limit the extracted beam fluctuations to less than 1/10 of the beam size, the septum field must be stabilized to roughly $\Delta I/I \sim 5 \times 10^{-6}$. This field tolerance should be eased by a factor of 10 by powering a compensation bend in series with the septum as is discussed in Section 4.3.1.

The compensation bending magnet has not been designed. It is required to have an integrated field of 7.7 kGauss-m. In the present design, we have assumed a magnetic length of 80 cm and a field of roughly 10 kGauss. The length and design of the magnets will be adjusted so that the current needed to excite these compensation magnets will be equal to the current needed for the septa so that both can be powered in series.

Correction Coils

The ring will need dipole, quadrupole, and skew quadrupole correctors. The quadrupole correctors are required to optimize the dispersion match through the arcs and wiggler, and the skew quadrupole correctors are needed to correct the betatron coupling and vertical dispersion. The number, placement, and strength of the quadrupole and skew quadrupole correctors has not been determined. With independent power supplies, additional quadrupole trims will not be necessary and, with magnet movers on the quadrupoles or sextupoles, additional skew quadrupole trims will not be needed.

Each standard arc cell will require one vertical dipole corrector and two horizontal dipole correctors which we have nominally placed at the S1 and S3 sextupoles. These correctors should have maximum strengths of 33 G-m which corresponds to a 0.5-mr deflection. Simulations of the trajectory correction show that the typical strength of the correctors is roughly 120 μr. Assuming uncorrelated variation, the corrector power supplies must regulate at the level of $\Delta I/I \lesssim 1 \times 10^{-4}$ to limit the vertical orbit jitter to one tenth of the vertical beam size.

As stated, in the arcs, we plan to use trim windings to the sextupoles to generate dipole fields as is done in the ALS. This choice saves space along the beam line, and makes it relatively easy to generate horizontal magnetic field for the vertical steering despite the vacuum ante-chamber. Also sextupole trims generate a more uniform dipole field than trim winding on the quadrupoles. Additional trim windings on the sextupoles could be used to generate skew quadrupole fields for correction if needed.

In the wiggler straight section, we plan to use trim windings on QFW and QDW quadrupoles for the horizontal and vertical correction. These quadrupoles have larger bore and smaller corrector strengths are required so we are not concerned about the sextupole fields introduced. These correctors should have maximum strengths of 16 G-m, which corresponds to a 0.25-mr deflection. The corrector power supplies must also regulate at the level of $\Delta I/I \lesssim 1 \times 10^{-4}$ to limit the vertical orbit jitter to one-tenth of the vertical beam size. In addition, we could add trims to the ends of each wiggler sections for additional horizontal correction. No estimate of the required strengths has been made.

In the injection and extraction straight section, we need additional orbit correction to optimize the trajectory through the septa. At this point, we have not studied these needs and have only assumed correctors located at the focusing and defocusing quadrupoles that are similar to the wiggler straight section. It will be straightforward to add additional dipole correctors in this region since the vacuum chamber will not include the ante-chamber and will be relatively clear.

4.10.2 Pre-Damping Ring

Bending Magnets

The bending magnets for the pre-damping ring are combined-functions magnets with a 17.5-kGauss effective field and a gradient of 33 kGauss/m; the required good field region is ± 2 cm. The vertical aperture is 4.4 cm which is 6-mm larger than the vacuum chamber height, leaving roughly 2.5 mm for the vacuum chamber wall. Parameters of the magnets are listed in Table 4-29.

At this time, we have not modeled the magnet and may have to modify the parameters subsequently. Because the magnet is a high-field gradient magnet, the fields may be difficult to attain without significant saturation. Although the magnet could be designed to operate with a saturated pole, the saturation will cause the relative field components to vary as a function of the excitation. This may make changing the ring energy difficult. If necessary, we could consider using additional trim magnets to provide the bending or we could construct the pole from Vanadium Permendur which saturates at a higher magnetic field.

Quadrupole and Sextupole Magnets

The quadrupoles and sextupoles in the pre-damping ring have larger apertures than in the main damping ring but similar construction issues apply. The arc magnets will need to accommodate the vacuum ante-chamber and thus will probably be constructed with an asymmetric design. The injection and extraction region quadrupoles have larger

Magnet	Quan.	$B_{0\,\mathrm{eff}}$ (kGauss)	dB_y/dx (kGauss/m)	Mag. Len. (cm)	$\frac{1}{2}$ Gap (cm)
BB (Main Bends)	28	17.5	33	80	1.9
BM (Matching Bends)	4	17.5	0	40	1.9

Table 4-29. *Pre-damping ring bending magnets for Vers. 3.4.*

Arc QFs:	
Number	42
Magnetic Length	26 cm
Inscribed Radius	3.5 cm
Max. B_{pole}	8.8 kGauss
Arc QDs:	
Number	56
Magnetic Length	15 cm
Inscribed Radius	3.5 cm
Max. B_{pole}	5.1 kGauss
Inj/Ext Quads:	
Number	6
Magnetic Length	20 cm
Inscribed Radius	4.0 cm
Max. B_{pole}	4.3 kGauss
Arc Sexts:	
Number	112
Magnetic Length	9 cm
Inscribed Radius	3.0 cm
Max. B_{pole}	2 kGauss

Table 4-30. *Quadrupole and sextupole magnet parameters for NLC pre-damping rings at 2.2 GeV.*

apertures. Although we have not yet started designs of the magnets, they are not expected to be difficult. Table 4-30 lists the magnets and requirements.

Corrector Magnets

The dipole correction fields will be generated in the arcs using trim windings on the sextupoles as is planned for the main damping rings. In the straight sections, the dipole fields would be generated with trim windings on the quadrupoles.

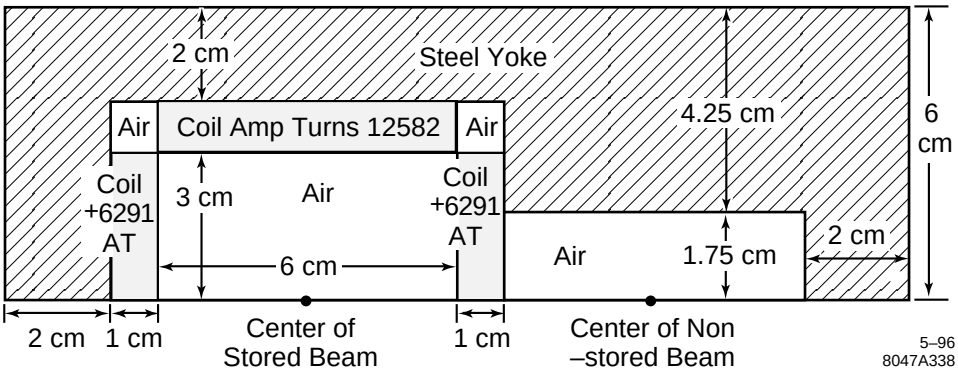

Figure 4-83. *Upper half of a single Panofsky quadrupole for pre-damping ring injection and extraction regions; the present design uses a dual Panofsky quadrupole.*

Injection/Extraction Septa

In the present design, the injection and extraction septa are vertically deflecting Lambertson septa. This is not considered a liability in the pre-damping ring because the vertical emittances are still large. A Lambertson septum can provide strong magnetic fields with greater reliability than a current-sheet septum. The fields in the septa are assumed to be 5 kGauss with a 2.3-cm-thick blade. At this time, no design exists but these parameters are quite relaxed.

Panofsky Quadrupoles

To ease the requirements on the injection and extraction kickers, we plan to use a dual Panofsky quadrupole as the horizontally focusing quadrupole next to the two septa. This provides horizontal focusing of both the stored and injected or extracted beams but does not deflect their trajectories. The dual quadrupole is 50-cm-long and has a gradient of 60 kGauss/m. The apertures are 6.2 cm by 6.2 cm with a 2-cm-thick central blade. The required current density is roughly 20 A/mm^2 which is a factor of six less than that in the SLC damping ring septa; these currents should be straightforward to attain. A preliminary single quadrupole design is illustrated in Figure 4-83.

4.10.3 Injection and Extraction Kickers

Damping ring injection is accomplished by bringing the beam toward a ring straight section at a large enough angle to clear the conventional magnets, bending it nearly parallel to the ring orbit with a DC septum magnet, and bending it onto the ring orbit with a pulsed kicker magnet at the point where the injected and stored orbits cross. Extraction is accomplished by analogous components, in the reverse order. The overall NLC design optimization requires that several trains of bunches must be damped simultaneously. The rise and fall times of the kicker magnetic field must be less than the gap between bunch trains, and the field must be flat for the duration of the train. The NLC parameters allow 60 ns for kicker rise and fall times, and require a 130-ns flattop.

These parameters are similar to those of the SLC damping rings. The SLC damping rings have revolution periods of 120 ns and each ring stores two bunches. The e^+ ring kickers extract and inject one bunch each cycle (the other bunch remains for more damping), while the e^- ring kickers inject and extract both bunches each cycle (one for collisions, one to produce more positrons). The SLC e^+ kickers demonstrate injection and extraction with 60-ns rise and fall

Parameter	Value
Rise time	60 ns
Falltime	60 ns
Flattop	130 ns
Repetition rate	180 Hz
Beam Energy	2.0 GeV
Injected Invariant Emittance	1.0×10^{-4} m-rad
Extracted Invariant Emittance	3.0×10^{-6} m-rad
Insertion Lattice	90° FODO
Insertion Quad Spacing	2.9 m
Beta at Kicker	5.0 m
R_{12} from kicker to septum	6 m
Kick Angle	2.5 mr
Injection Kick Tolerance	$\pm 3.5 \times 10^{-3}$
Extraction Kick Tolerance	$\pm 0.5 \times 10^{-3}$

Table 4-31. *NLC main damping ring kicker requirements.*

times without disturbing other stored bunches. The SLC e^- kickers demonstrate injection and extraction with 60-ns rise or fall times of 60-ns-long bunch trains (albeit containing only two bunches) on a single pulse.

The SLC kickers are implemented with thyratron pulsers, discharging coaxial cables, or oil-filled Blumleins through cables into transmission line magnets with resistive terminations. The magnets use ferrite flux returns and distributed capacitance with loaded epoxy dielectric. The kicker beam pipes are ceramic, with a thin metallic coating to decouple the magnets from the beam at high frequencies. This basic topology, with some parametric changes, is also appropriate for the NLC kickers.

However, several iterations of design over several years were required to produce kicker systems that were operationally reliable and met the SLC performance specifications. Some additional development and demonstration will be required for the NLC. The large aperture (the result of the large emittance) in the NLC e^+ pre-damping ring poses quantitatively larger difficulties than in the SLC case. On the other hand, some of the NLC parameters are more favorable than for SLC, and allow straightforward solutions to the new problems.

Main Damping Rings

The e^- and e^+ main damping rings are identical, and there is little difference in the requirements for injection and extraction, so the same kicker system may be used in all four cases. (The e^+ pre-damping ring kickers are discussed elsewhere, since the requirements are somewhat different.) The requirements are listed in Table 4-31. The tolerances correspond to a centroid jitter of 10% of the beam sigma.

For a transmission line magnet, the field rise time is the sum of the electrical pulse rise time and the magnet transit time. We budget half of the 60-ns rise time to the electrical pulse, leaving 30 ns for the magnet transit time, as for the SLC. The kick angle and beam energy determine the product of field and length. Combined with the horizontal aperture, this determines the total magnetic flux. Combined with the transit time, this determines the voltage, independent of length. The height is fixed by the aperture requirement, then the length essentially determines the required current, or equivalently the magnet and pulser impedance. For the SLC, the available length is short, resulting in an impedance of 12.5 Ω. This requires a large capacitance per unit length, and degrades the thyratron rise time. The kicker length of 1.2 m is chosen for the NLC to produce an impedance of 50 Ω, requiring 16 times less capacitance per unit length

Parameter	Value
Electrical transit time	30 ns
Horizontal aperture	30 mm
Vertical aperture	30 mm
Length	120 cm
Field	139 Gauss
Current	332 A
Voltage	16.7 kV
Inductance	1.51 μHenry
Capacitance	596 pF
Impedance	50 Ω

Table 4-32. *NLC main damping ring kicker magnet parameters.*

than for the SLC. Despite the higher impedance, the magnet voltage is less than half that required in the SLC (this is indirectly the result of the lower emittance). The SLC kicker magnets are 9-cell LC transmission lines with ferrite flux returns, and a similar construction (albeit physically longer) would have adequate bandwidth to meet the NLC requirements. The kicker magnet parameters are listed in Table 4-32.

Kicker Pulsers

Kicker pulsers very similar to those used in the SLC would probably be adequate for the NLC. For three of the four kickers in the SLC (all but e^- extraction), a simple pulser circuit with a charge-line discharged by a thyratron is operationally adequate, although it does not strictly rise from 0.0% to 100.0% or fall from 100.0% to 0.0% in 60 ns. The coherent damping time of the SLC damping rings is fast enough that the midstore kicks in the e^+ ring due to rise and fall times in excess of 60 ns does not degrade the stored beam emittance (although it is operationally preferred to adjust the ring tune so the two midstore kicks tend to cancel). The rise time of the e^- injection kicker and the fall time of the e^- extraction kicker are irrelevant, because there are no other bunches in the ring at those times. Any kick on the turn after e^- injection from excessive fall time damps away rapidly. The case of SLC e^- extraction is more complex and is discussed below.

Since in the NLC, rise or fall times in excess of the 60-ns nominal would only affect bunches that remain in the rings, slight precursors or tails would presumably be tolerable. If this is the case, simple thyratron cable discharge pulsers would be adequate for the NLC main damping rings. With a continuous coaxial charge line, the pulse is intrinsically flat, with only a very slight droop from attenuation in the charge-line cable, plus any residual ringing from the thyratron switching.

Should the flatness of the pulse not meet the specification, it is possible to install an identical kicker magnet in the extraction line outside the ring, at a point related by a $\pm I$ transport matrix to the ring kicker. If the pulser feeds both magnets in parallel, and the cable delays are set appropriately, kicker pulse errors induced at the first magnet will be canceled by the second magnet. It is not unreasonable to expect an order of magnitude relaxation of the flatness tolerance by this technique.

Since the system impedance is higher than for SLC, the thyratron rise time should be somewhat better for the NLC. If the rise and fall times from a simple thyratron pulser are not adequate, several strategies are available. The budget for thyratron rise and fall time can be increased by reducing the magnet transit time. The rise and fall time of the thyratron pulse can be improved, at the expense of more complexity. Or thyratrons could be replaced by other switches, such as spark gaps or solid-state devices.

Cutting the magnet length in half gains 15 ns, but requires twice the current and voltage. Two half-length magnets fed in parallel also gains 15 ns, with no increase in voltage but a doubling of (total) current. Reducing the magnet capacitance per unit length by a factor of four would also gain 15 ns, but would double the impedance and thus the voltage. There is room in the lattice for two such magnets fed in parallel, which could operate at the same voltage and (total) current as the original design but still gain 15 ns of transit time.

In the SLC e^- ring, both bunches are extracted on a single pulse, so a degraded rise time results in one of the two bunches receiving a kick on the turn before extraction. The thyratron pulser is augmented by a saturating ferrite pulse-sharpening filter that removes thyratron prepulse (produced by the intermediate grids in the multistage thyratrons), and part of the slow early rise of the current waveform. This device does not degrade the pulse flatness, but does degrade the fall time. Also, a peaking capacitor in parallel with the charge-line is used to make the current overshoot initially, which makes the field reach the 100% level more quickly, but both degrades the flatness and the fall time (a smaller capacitance value would improve the rise time with minimal flatness degradation, but for the SLC rise time is more important). Since the "bunch train" only has two bunches in the SLC, a single pulse shape adjustment is adequate to make the kick magnitude equal at the two times of interest. It is implemented by oil-filled, motor-adjustable, variable-impedance insertions in the charge-lines.

All of the above pulser modifications degrade the fall time. For SLC e^- extraction, any fall time degradation is irrelevant and is not corrected. For the NLC, one could "use" bunch trains in such an order that the (trailing) train that is disturbed by a slow fall time is the one that will remain in the ring the longest for additional damping. If pulser modifications are used to improve the rise time for the NLC, another thyratron could also be added to the pulser, which would be fired to define the end of the pulse, circumventing the degradation in fall time. This technique is standard for long pulse kickers in proton machines.

Spark gaps, since they operate at high pressure rather than near-vacuum, have much higher dI/dt than thyratrons. With laser-triggering to reduce time jitter to tolerable values, and adequate engineering for erosion reduction and/or rapid replacement, spark gaps could be a thyratron alternative with better rise time and fall time.

Solid-state FETs are now available with rise times better than 10 ns, up to about 1000 V and about 100 A, and have the advantage that they can be turned off as well as on. They can be run in parallel for higher currents, and can be stacked in series for higher voltages. A series-switched FET pulser to produce a 20-kV pulse would require about 40 stages (since the charge voltage is twice the pulse voltage), each stage with several FETs in parallel to handle the current. It is not trivial to trigger a FET stack in such a way that none of the FETs is ever over-voltaged and destroyed, but it is not beyond the state of the art. The number of stages can be reduced by using a transformer, although more parallel FETs are needed in each stage, and the transformer loses some of the rise time improvement.

If the magnet is divided into enough segments fed in parallel (about 20), the voltage required is low enough that a few FETs in parallel could drive each segment directly. The engineering challenges with this approach are that the impedance becomes so low that the FETs must be located very close to the magnet, and the magnet is no longer a transmission line, so it is more difficult to obtain a flat pulse shape.

Pre-Damping Ring

The e^+ pre-damping ring must accept and rapidly reduce the large emittance of the undamped positrons. The pre-damping function is separated from the final damping largely due to the tradeoff between damping rate and final emittance, but the separation has the side benefit of making the kickers less difficult. The requirements for the injection kicker are listed in Table 4-33; the extraction kicker is similar except the required kick angle is 6.7 mr instead of 8 mr. The large emittance results in a large kick angle which require very high kicker power levels, but also relaxes the tolerances compared to the main damping rings.

Parameter	Value
Rise time	60 ns
Fall time	60 ns
Flattop	130 ns
Repetition rate	180 Hz
Beam Energy	2.0 GeV
Injected Invariant Emittance (edge)	6.0×10^{-2} m-rad
Extracted Invariant Emittance (rms)	1.0×10^{-4} m-rad
Insertion Lattice	90° FODO
Insertion Quad Spacing	2.9 m
Beta at Kicker	5.0 m
R_{12} from kicker to septum	6 m
Injection Kick Angle	8.0 mr
Injection Kick Tolerance	$\pm 10 \times 10^{-3}$
Extraction Kick Tolerance	$\pm 1.6 \times 10^{-3}$

Table 4-33. *NLC e^+ pre-damping ring injection kicker requirements.*

Parameter	Value
Electrical transit time	30 ns
Horizontal aperture	62 mm
Vertical aperture	45 mm
Number of feeds	6
Length per feed	28.9 cm
Field	308 Gauss
Current	1104 A
Voltage	18.4 kV
Inductance per feed	0.854 μHenry
Capacitance per feed	3070 pF
Impedance	16.6 Ω

Table 4-34. *NLC e^+ pre-damping ring kicker magnet parameters.*

Achieving a 30-ns magnet transit time in a single magnet would require 80 kV, which is far outside of the SLC experience, so the magnet is divided into four segments driven in parallel at roughly 20 kV. To keep the total length reasonable, the magnet impedance is chosen to be 16.6 Ω. This is 50% higher than the SLC kickers, but requires roughly the same capacitance per unit length. The pre-damping ring kicker magnet parameters are listed in Table 4-34.

The pre-damping ring kicker pulser parameters are essentially identical to those for the main ring kicker pulsers, apart from the lower impedance level. However, six such pulsers are needed for injection, and five for extraction. The lower impedance makes the rise time and fall time requirement somewhat harder to meet, although by using two thyratrons in parallel for each pulser, the impedance per tube can be increased back to the same as for the main ring kickers. (The SLC e^- pulsers demonstrate the feasibility of parallel thyratrons.) The same types of magnet modifications and pulser modifications discussed in connection with the main ring kickers could be used for the pre-damping ring kickers, but the more relaxed tolerances may make them unnecessary.

4.10.4 Transport Lines

The magnets used in the injection, extraction, and other transport lines are straightforward and will not be described.

4.11 Instrumentation for the Main Damping Rings

The emphasis for the damping ring instrumentation is to provide sufficiently high-resolution monitoring to meet the performance requirements for emittance and stability. In particular, the main damping rings require precise control of the beam position in the ring magnets as well as high-resolution beam size measurements to monitor the damping process. The beam-based alignment procedures also require high resolution BPMs to determine small orbit shifts as magnets are varied and to track sources of beam jitter. Finally, the multibunch stability requirements demand accurate bunch-to-bunch measurements of bunch intensity, position, and phase.

4.11.1 Beam Position Monitors

The BPM system is scaled from the PEP-II BPM system using "button" BPM electrodes and BPM processors with a 10-MHz bandwidth that will average over roughly twenty bunches in a train. Each BPM module will contain on-board DSP and memory to allow for multi-turn averaging and other data manipulation. Using the present PEP-II ADC's, the maximum measurement rate would be once every $7\ \mu$s (roughly once every 10 turns).

The button-style BPMs have the advantage of lower beam impedance and simpler construction compared to stripline monitors. We have assumed buttons with an 8-mm diameter in a 1.25-cm-radius beam pipe as described in Section 4.4.1.

Three BPMs are required per arc cell to ensure coverage of all betatron phases and provide some redundancy in monitoring. This makes for 114 arc BPMs, plus eight matching section BPMs, nine wiggler section BPMs and seven straight-section BPMs, giving a total of 138 BPMs per ring. The arc BPMs will be centered in each of the S1 and one of the S3 sextupoles rather than in the quadrupoles, since the orbit tolerances are tightest in the sextupoles.

The tightest resolution requirement is in monitoring the position of the stored orbit since it impacts the vertical equilibrium emittance and is needed for the beam-based alignment of the magnets. Here, 1-μm resolution is required with a 1-μm rms stability over a few hours, and 10-μm stability over 24 hours. Similar requirements are found elsewhere in the NLC, but the stored orbit measurement is made easier by measuring over many turns and applying filtering and signal processing techniques in the BPM electronics to extract the beam signal. The proposed system should have a single turn resolution of

$$\sigma \sim 1\ \mu\mathrm{m}\sqrt{1+\left(\frac{0.5\,\mathrm{A}}{I_{\mathrm{train}}}\right)^2} \tag{4.86}$$

for the average position of twenty adjacent bunches. This is more than sufficient for normal operation and for low current studies the 1-μm resolution could be obtained by averaging over many turns.

Of course, the stringent BPM stability requirement might only be met if remote sensing of magnet positions is also implemented in the ring. BPMs reveal relative changes between the beam and the magnet holding the BPM, but are blind to thermal and seismic drifts in magnet position. The stability issues were discussed in Section 4.8.2.

Specifications for single-turn measurement resolution are considerably looser $\sim 50\,\mu$m as it is used mainly for diagnosing injection errors. The more important criterion for the single-turn measurements is the resolution of individual bunches within each train. A small number (minimum two) of dedicated BPMs will be needed to resolve bunch-to-bunch injection errors. Similarly, bunch-to-bunch errors in the stored beam, which arise from instabilities, can be detected by the same two high-bandwidth BPMs. The bunch spacing in the train suggests a 1-GHz bandwidth is required to discriminate individual bunch motion. The high-bandwidth processor can be used in conjunction with a resonant stripline BPM, turned to have notches in the response at the revolution harmonics thereby enhancing the betatron sidebands.

The limited redundancy in the specified number of arc BPMs is rapidly consumed by the number of special-purpose BPMs: two BPMs are required for single-turn phase space reconstruction; sample-and-hold BPM sum signal is used for peak current monitoring of transient bunch length instabilities; high-bandwidth signal path ($\sim$30 GHz) is required from one BPM for spectral analysis of bunch length instability phenomena; several additional pickups are used for phase monitoring and rf feedback systems.

4.11.2 Beam Size Monitors

Measurement of the beam size in the ring is required to monitor the damping process and to verify that the desired equilibrium emittance is attained. Imaging of visible synchrotron radiation gives an immediate diagnostic of the injected beam size and condition. The gated cameras used in the SLC damping rings can resolve turn-by-turn changes in beam size but will not distinguish individual bunches in the NLC train.

Unfortunately, the fully-damped beam is too small to resolve by visible light. The diffraction-limited resolution is given by [Hofmann 1982]

$$\Delta y = 0.6\gamma\sqrt{2\lambda\lambda_c} \tag{4.87}$$

where $\lambda_c = \frac{4\pi}{3\gamma^3}$, giving at best a 26-$\mu$m resolution, whereas the vertical equilibrium beam size in the arc dipoles is 6 μm.

The visible synchrotron light will be an excellent diagnostic for the beam before it reaches the equilibrium beam size, but measurement of the final spot would require at least a factor 20 shorter wavelength. This would require a monitor operating in the XUV to soft X-ray regime, for which there is no easy design solution.

An alternative to a beam size monitor is to measure the equilibrium beam size with a scanning "laser wire" as proposed at many other points along the NLC. The scanning process probably loses the turn-by-turn beam size information, but this should not be an issue for the stored beam. It may also be possible to design a laser scanner that could scan the beam size quickly compared to the damping time, *i.e.*, $\lesssim 1$ ms.

4.11.3 Bunch Length Measurement

Streak camera measurements of the visible synchrotron radiation yield bunch length and bunch distribution data on a turn-by-turn basis and can further discriminate between individual bunches in the train. Additional confirmation of bunch length can be made with the extracted beam profile at a high-dispersion location downstream of the bunch compressor; this is discussed further in Chapter 5. Finally, transient bunch length behavior in the rings can be observed on the BPM signals, as mentioned above.

4.11.4 Polarization Measurement

Unfortunately, it may be difficult to measure the polarization in the ring because of backgrounds due to synchrotron radiation and particle loss. Regardless, the polarization of the electrons can be measured in the extraction line using a Compton laser polarimeter. Depolarizing resonances are only likely to be encountered in the ring if the energy is changed to achieve shorter damping times for faster repetition rate operation.

4.11.5 RF Diagnostics

The damping ring bunches should be phase-locked to the main linac rf system at the level of 0.1°. Beam loading introduces a phase offset across the bunch so high-bandwidth systems must be used to detect the phase of individual bunches. Stable operation of the rf system under the heavy beam loading will require extensive monitoring of phase and power levels throughout the klystron and feedback systems; this is discussed further in Section 4.5.3.

4.11.6 Ion Measurements

Ion effects can be a serious performance limitation and may work in an unpredictable way. The onset of ion accumulation may be observed with gated beam loss monitors which detect electrons scattered from the ion cloud although this would likely be difficult due to backgrounds. The effect of the ions may be to cause tune shifts in the beam during the store time. Dynamic tune changes such as these can be monitored by gated excitation of the betatron tunes.

4.11.7 Conventional Diagnostics

This would include numerous betatron tune measurement systems based on turn-by-turn BPM analysis, spectrum analyzers, beam excitation systems, etc.. Also included are machine-protection systems that are routinely monitored, for example, during machine repetition rate changes.

4.12 Conclusions and Comments

In this chapter, we have described the damping ring complex for the NLC. The damping rings are designed to produce beams with emittances of $\gamma\epsilon_x = 3 \times 10^{-6}$ m-rad and $\gamma\epsilon_y = 3 \times 10^{-8}$ m-rad at a repetition rate of 180 Hz. With the present electron and positron injector designs, this requires damping the incoming electron emittance by over four orders of magnitude and the incoming positron emittance by roughly six orders of magnitude.

The damping is performed in three rings: a pre-damping ring for the positrons which damps the very large incoming positron emittance to roughly the same size as the incoming electron beam, and two main damping rings that damping the electrons from the injector and the positrons from the pre-damping ring to the desired final values. All three rings use high-field combined-function bending magnets and the main damping rings also have 26 m of wiggler magnets to attain the desired damping rates.

The design of the pre-damping ring is relatively straightforward—the primary difficulties are related to the very large incoming beam emittance, *i.e.,* the large transverse and energy apertures that are required and the injection and extraction systems. We presented a design with solutions for both of these issues. Although we have not yet started detailed engineering studies for the components of the ring, the tolerances and requirements appear reasonable. The alignment tolerances are well within the capabilities of conventional alignment practices (although we will include the ability to use beam-based alignment) and most magnet requirements are not dissimilar from those of the PEP-II LER or the ALS synchrotron light storage ring.

The main damping rings are more difficult and thus most of our studies have concentrated on them. Fortunately, the rings have a number of similarities with the present generation of synchrotron light storage rings and with the new flavor factories being constructed. In addition, many of the design and physics questions will be studied in the ATF prototype damping ring that is being constructed at KEK. Thus, many of the accelerator physics questions that may arise in the NLC damping rings will be studied and verified in these other rings.

These similarities have also simplified the design process and provide confidence that most of the components could be constructed. In particular, the beam currents are less than those in the PEP-II LER and we have adopted rf cavities and a multibunch feedback system based on those being constructed for the LER. Likewise, the vacuum system is based on those of the ALS and PLS synchrotron radiation sources and the magnets designs are similar to those in these and other radiation sources. Although many of these components are the present state-of-the-art, we will benefit from operational experience of these other rings before the construction of the NLC is started. This will allow appropriate design modifications to ensure the required reliability for the NLC damping rings.

One exception are the combined-function bending magnets which have higher fields than in these other rings. We have performed some initial studies which show that the fields are attainable, but we still will need to build and measure a prototype before we can have complete confidence in the design. Fortunately, this is relatively inexpensive. If indeed the specifications cannot be met, it is straightforward to redesign the rings with looser requirements on the bending magnets although this is at the expense of some of the operating range.

Finally, the damping rings must provide a stable reliable platform for the rest of the collider. One of the lessons from the SLC is that we cannot expect optimal performance if all the components are operated at their limits. Thus, throughout the damping ring designs, we have provided substantial margin in the design performance over that actually required for the NLC. In particular, we have designed for higher currents than needed as well as apertures in excess that required. Similarly, we have provided for beam-based alignment and tuning systems that will provide much better accuracy than is actually needed. All of these overheads in the design should yield improved operations and reliability.

References

[Adolphsen 1995] C. Adolphsen, private communication (1995).

[Baltay] M. Baltay, private communication (1995).

[Bane 1988] K. Bane, "The Caculated Longitudinal Impedance of the SLC Damping Rings", *Proc. of the 1st European Part. Acc. Conf.*, Rome, Italy, 637 (1988).

[Bane 1989] K. Bane and R. Ruth, "Bunch Lengthening Calculations for the SLC Damping Rings", *Proc. of the 1989 Part. Acc. Conf.*, Chicago, IL, 789 (1989).

[Bane 1993] K. Bane and K. Oide, "Simulations of the Longitudinal Instability in the SLC Damping Rings", *Proc. of the 1993 Part. Acc. Conf.*, Washington DC, 3339 (1993).

[Bane 1995a] K. Bane and K. Oide, "Simulations of the Longitudinal Instability in the New SLC Damping Rings", *Proc. of the 1995 Part. Acc. Conf.*, Dallas, TX (1995).

[Bane 1995b] K. Bane *et al.*, "High-Intensity Single Bunch Instability Behavior in the New SLC Damping Ring Vacuum Chamber", *Proc. of the 1995 Part. Acc. Conf.*, Dallas, TX (1995).

[Bane 1995c] K. Bane and K. Kubo, "Bunch-to-Bunch Variation in the Synchronous Phase in the NLC Damping Rings", NLC–Note 19 (1996).

[Barnet 1994] I. Barnet *et al.*, "Dynamic Beam Based Alignment", CERN–SL94–84 (BI), (1994).

[Barry 1993] W. Barry *et al.*, "Design of the ALS Transverse Coupled Bunch Feedback System", *Proc. of the 1993 Part. Acc. Conf.*, Washington, DC (1993).

[Barry 1995] W. Barry *et al.*, "Design of the PEP-II Transverse Coupled Bunch Feedback System", *Proc. of the 1995 Part. Acc. Conf.*, Dallas, TX (1995).

[Bartalucci 1993] S. Bartalucci *et al.*, "Analysis of methods for controlling multibunch instabilities in DAFNE", LNF–93/067 (P), (1993).

[Berg 1995] J. Scott Berg, "Transverse Coupled Bunch Mode Coupling and Growth Rates for the NLC Main Damping Ring", NLC–NOTE–10 (1995).

[Boussard 1975] D. Boussard, CERN LABII/RF/INT/75–2 (1975).

[Boussard 1983] D. Boussard and G. Lambert, "Reduction of the Apparent Impedance of Wide-Band Accelerating Cavities by RF Feedback", *IEEE Trans. Nucl. Sci.* **30**, 2239 (1983).

[Brinkmann 1990] R. Brinkmann, "A Study of Low Emittance Damping Ring Lattices", DESY–M–90–09 (1990).

[Chao 1995] A. Chao, B. Chen, and K. Oide, "A Weak Microwave Instability with Potential Well Distortion and Radial Mode Coupling", presented at the 1995 Part. Acc. Conf., Dallas, TX (1995).

[Corlett 1993] J.N. Corlett and R.A. Rimmer, "Impedance Measurements of Components for the ALS", *Proc. of the 1993 Part. Accel. Conf.*, Washington, DC (1993).

[Fox 1993] J. Fox *et al.*, "Feedback Control of Coupled Bunch Instabilities", *Proc. of the 1993 Part. Accel. Conf.*, Washington, DC (1993).

[Furman 1995] M. Furman, "The Positron Beam Instability Code POSINST", to be documented (1995).

[Grobner] O. Gröbner, "Bunch Induced Multipactoring", *Proc. Xth Int. Conf. on High Energy Acc.*, Serpukhov, USSR, 277 (1977).

[Greene 1992] E. Greene, T. Warwick, "Environmental Vibration Measurements of the ALS Floor and Storage Ring", LSBL–144 (1992).

[Halbach 1969] K. Halbach, *Nucl. Instr. and Methods* **74**, 147 (1969).

[Halbach 1985] K. Halbach, *J. Appl. Phys.* **57**, 3605 (1985).

[Haïssinksi 1973] J. Haïssinski, "Exact Longitudinal Equilibium Distribution of Stored Electrons in the Presence of Self-Fields", *Il Nuovo Cimento* **18B**, No. 1, 72 (1973).

[Heifets 1994a] S. Heifets, "Bunch-to-Bunch Phase Variation in the NLC DR", NLC–NOTE–6 (1994).

[Heifets 1994b] S. Heifets, "Study of the NLC DR Impedance and Collective Effects: the First Attempt", NLC–NOTE–9 (1994).

[Heifets 1995] S. Heifets, "Study of an Instability of the PEP-II Positron Beam", PEP-II AP Note 95.21 (June 7, 1995).

[Heim 1995] J. Heim *et al.*, "Wiggler Insertion of the PEP-II B-Factory," *Proc. of the 1995 Part. Acc. Conf.*, Dallas, TX (1995).

[Herb 1995] S. Herb, G.B. Jaczko, and F. Willeke, "Beam-Based Calibration of Beam Position Monitor Offsets in the HERA Proton Ring using Strong Sextupole Fields", (1995).

[Hirata 1992] K. Hirata and K. Yokoya, "Nongaussian Distribution of Electron Beams due to Incoherent Stochastic Processes", *Particle Acclerators* **39** 147–158; and KEK–Preprint–91–212 (1992).

[Hofmann 1982] A. Hofmann and F. Meot, "Optical Resolution of Beam Cross-section Measurements by Means of Synchrotron Radiation", *Nucl. Instr. and Methods* **203**, 483–493 (1982).

[Izawa 1995] M. Izawa, Y. Sato and T. Toyomasu, "The Vertical Instability in a Positron Bunched Beam", *Phys. Rev. Lett.* **74**, 5044 (1995).

[JLC] KEK JLC damping ring design.

[Juravlev 1995] V.M. Juravlev *et al.*, "Seismic Conditions in Finland and Stability Requirement for the Future Linear Collider" (1995).

[Kamada 1994] S. Kamada, "Overview on Experimental Techniques and Observations", *Proc. of the Workshop on Nonlinear Dynamics in Particle Accelerators: Theory and Experiments*, Arcidosso, Italy (1994).

[ATF 1995] "ATF Accelerator Test Facility Design and Study Report", KEK Internal 95–4 (1995).

[Kikuchi 1995] M. Kikuchi *et al.*, "Beam-Based Alignment of Sextupoles with the Modulation Method", *Proc. of the 1995 Part. Acc. Conf.*, Dallas, TX (1995).

[Klatt 1986] R. Klatt and T. Weiland, "Wake Field Calculation with Three-Dimensional SCI Code", *1986 Linear Acc. Conf. Proc.*, SLAC, 282 (1986).

[Krejcik 1993] P. Krejcik *et al., Proc. of the 1993 Part. Acc. Conf.*, Washington DC (1993).

[Kubo 1993] K. Kubo, *et al*, "Compensation of Bunch Position Shift Using Sub-RF Cavity in Damping Ring", *Proc. of the 1993 Part. Acc. Conf.*, Washington, DC, 3503 (1993).

[Lambertson 1995] See, for example, G.R. Lambertson, "Update of RF Reaction During Beam Gap", PEP–II Tech Note 85 and CBP Tech Note 73, (1995).

[Mattison 1995] T. Mattison, "Injection/Extraction Kickers for the NLC Damping Rings", talk given to NLC damping ring group 1/10/95.

[Minty 1995] M.G. Minty, W.L. Spence, "Injection Envelope Matching in Storage Rings," *Proc. of 1995 Part. Acc. Conf.*, Dallas, TX (1995).

[Minty 1995b] M.G. Minty and R.H. Siemann, "Heavy Beam Loading in Storage Ring RF Systems", SLAC–PUB–95–6801, submitted to *Nucl. Instr. and Methods* , (September 1995).

[Moshammer 1993] W. Moshammer and T. O. Raubenheimer, presentation at LC93.

[Murphy 1987] J. B. Murphy, "Storage Ring Lattice Considerations for Short Wavelength Single Pass FELs", *Proc. of the ICFA Workshop on Low Emittance e^+e^- Beams*, BNL–52090, Brookhaven, NY, 197 (1987).

[Ohmi 1995] K. Ohmi, "Beam and Photo-Electron Interactions in Positron Storage Rings", KEK Preprint 94–198, (February 1995).

[Oide 1990] K. Oide and K. Yokoya, "Longitudinal Single Bunch Instability in Electron Storage Rings", KEK Preprint 90–10, (1990).

[Oide 1994] K. Oide, "A Mechanism of Longitudinal Single Bunch Instability in Storage Rings", KEK Preprint 94–138, (1994).

[Pedersen 1975] F. Pedersen, "RF Cavity Feedback", *IEEE Trans. Nucl. Sci.* NS–22, no. 3 (1975), and NS-32, no. 3 (1985).

[Pedersen 1992] F. Pedersen, SLAC-400, 192 (1992).

[PEP-II 1993] LBL–PUB 5379, SLAC–418, in PEP–II Conceptual Design Report, June 1993.

[Piwinski 1972] A. Piwinski, DESY Report 72/72 (1972).

[Piwinski 1985] A. Piwinski, "Beam losses and lifetime", CERN Accelerator School, Gif-sur-Yvette, CERN**85-19** (1985).

[Raubenheimer 1988] T. O. Raubenheimer, L. Z. Rivkin, R. D. Ruth, "Damping Ring Designs for a TeV Linear Collider", *Proc. of the 1988 DPF Summer Study, Snowmass '88*, Snowmass, CO, 620 (1988).

[Raubenheimer 1991] T.O. Raubenheimer, "Generation and Acceleration of Low Emittance Flat Beams for Future Linear Colliders", Ph.D. Thesis, Stanford University, SLAC–387 (1991).

[Raubenheimer 1992] T.O. Raubenheimer and P. Chen, SLAC–PUB **5893**, in "Ions in the Linacs of Future Linear Colliders", Proc. of LINAC92, Ottawa, vol. 2, 630–632 (1992).

[Raubenheimer 1992] T. Raubenheimer, "Emittance Growth due to Beam Gas Scattering", KEK Report **92–7** (1992).

[Raubenheimer 1993a] T.O. Raubenheimer, R. Early, T. Limberg, and H. Moshammer, "A Possible Redesign of the SLAC SLC Damping Rings", *Proc. of the 1993 Part. Acc. Conf.*, Washington DC, (1993).

[Raubenheimer 1993b] T.O. Raubenheimer, K. Egawa, M. Kikuchi, K. Kubo, S. Kuroda, K. Oide, S. Sakanaka, N. Terunuma, J. Urakawa, "The Vertical Emittance in the ATF Damping Ring", *Nucl. Instr. and Methods* **A335:**1 (1993).

[Raubenheimer 1994] T.O. Raubenheimer "The Core Emittance with Intrabeam Scattering in e^+/e^- Rings", *Particle Acclerators* **45:**111 (1994).

[Raubenheimer 1995a] T.O. Raubenheimer and F. Zimmermann, "A Fast Beam-Ion Instability: Linear Theory and Simulations", *Phys. Rev. E* **52**, 5487 (1995).

[Raubenheimer 1995b] T.O. Raubenheimer, private communication (1995).

[Rieke 1972] F.F. Rieke and W. Prepejchal, "Ionization cross sections of gaseous atoms and molecules for high energy elelctrons and positrons", *Phys. Rev. A* **6**, (1972).

[Rimmer 1992] R.A. Rimmer, "RF Cavity Development for the PEP-II B-Factory", Proc. Intl. Workshop on B-Factories, KEK, Tsukuba, Japan (1992).

[Rivkin 1985] L. Z. Rivkin, "Damping Ring for the SLAC Linear Collider", Ph.D. Thesis, Cal. Tech. (1985).

[Robin 1995] D. Robin, G. Portmann, and L. Schachinger, "Automated Beam Based Alignment of the ALS Quadrupoles", NLC Note 18, (1995).

[Robinson 1962] K.W. Robinson, CEA report, CEAL–1010 (1962).

[Rojsel 1994] P. Rojsel, "A Beam Position Measurement System Using Quadrupole Magnets Magnetic Centre as the Position Reference", *Nucl. Instr. and Methods* in *Phys. Rev.* 343, (1994).

[Rogers 1995] J. Rogers, "Photoelectron Trapping Mechanism for Horizontal Coupled Bunch Mode Growth in CESR", CBN 95–2 (1995).

[Rossbach 1988] J. Rossbach, "Closed-Orbit Distortions of Periodic FODO Lattices Due to Plane Ground Waves", *Particle Acclerators* **23**, 121 (1988).

[Sakanaka 1995] S. Sakanaka *et al.*, "Design of a high power test cavity for the ATF damping ring", *Proc. of the Part. Acc. Conf.*, Dallas, TX (1995).

[Sands 1976] M. Sands, "Beam-Cavity Interactions", Orsay report, 2–76 (1976).

[Siemann 1983] R. Siemann, "Computer Models of Instabilities in Electron Storage Rings", in *The Physics of Particle Accelerators*, AIP Conf. Proc. **127**, 431 (1983).

[Stupakov 1995] G. Stupakov, T.O. Raubenheimer and F. Zimmermann, "A Fast Beam-Ion Instability: Effect of Ion Decoherence", *Phys. Rev. E* **52**, 5499 (1996).

[Thompson 1989] K.A. Thompson, "Transverse and Longitudinal Coupled Bunch Instabilities in Trains of Closely Spaced Bunches", *Proc. of the 1989 Part. Acc. Conf.*, Chicago, IL (1989).

[Thompson 1991] K.A. Thompson, "Simulation of Longitudinal Coupled-bunch Instabilities", ABC-24, (1991).

[Teng 1985] L.C. Teng, "Minimum Emittance Lattice for Synchrotron Radiation Storage Rings", LS–17 Argonne (1985).

[Turner 1995] J.L. Turner *et al.*, "Vibration Studies of the Stanford Linear Collider", *Proc. of the 1995 Part. Acc. Conf.*, Dallas, TX, (1995).

[Wilson 1994] P. Wilson, private communication (1994).

[Zisman 1986] M. Zisman, S. Chattopadhyay, J. Bisognano, "ZAP Users Manual", LBL–21270 (1986).

Contributors

- Karl Bane
- Lou Bertolini
- John Byrd
- Yunhai Cai
- John Corlett
- Dick Early
- Miguel Furman
- Sam Heifets
- Kwok Ko
- Patrick Krejcik
- Tom Mattison
- Bobby McKee
- Michiko Minty
- Cho Ng
- Tor Raubenheimer
- Robert Rimmer
- David Robin
- Ben Scott
- Steve Smith
- Bill Spence
- Cherril Spencer
- Gennady Stupakov
- Perry Wilson
- Sasha Zholents
- Frank Zimmermann